Catalytic processes for the control of nitrogen oxides emissions in the presence of oxygen.

POLITECNICO DI TORINO

Doctor of Philosophy in Chemical Engineering

Department of Applied Science and Technology

XXVIII Cycle (2013-2016)

PhD Thesis

Catalytic processes for the control of nitrogen oxides emissions in the presence of oxygen.

Academic Tutors:

Prof. Raffaele Pirone - Politecnico di Torino.

Prof. Fabio Deorsola - Politecnico di Torino.

PhD Student:

Silvia Andreoli

(No. 199920)

I dedicate my thesis to my little, big, fabulous world:
my mom, my dad and my husband.
Thank you

Introduction

The emissions of nitrogen oxides (NO_x) from power plant and vehicles are known to cause damages to human health and environmental safety. The introduction of the EURO 6 regulations has imposed new limits on emissions of different types of pollutants present in the flue gases of diesel engines.

In particular, the emission limits of autovehicles are different between stoichiometric oxygen-to-fuel ratios and oxygen-lean engine conditions: the latter ones are responsible of large amounts of particulate matter (PM) and nitrogen oxides (NO_x), which are very dangerous air pollutants. Conversely, since under stoichiometric conditions PM emissions are quite negligible and NO_x can be fruitfully removed by catalytic abatement, the former have been regulated by more stringent legislation. However, emissions limits are becoming stricter and stricter in recent years also for lean engines, although in the presence of oxygen the abatement of NO_x results in a much harder task.

Also for stationary plant, such as coffee roasters, the NO_x emissions will be limited and the new regulations will be enforced from April 2016, and also in these applications the presence of oxygen in the pollutants-containing gas will make any abatement process very difficult.

For these reasons, to fulfil the requests of the more stringent regulations, it is important to develop more efficient technologies which result in prevention of pollutants formation, together with improved abatement process for the pollutants emitted in the flue gases.

NO_x emission levels from autovehicles have been reduced by 66% from Euro 5, requiring the use of NO_x after-treatment devices in addition to in-cylinder measures such as cooled EGR (Exhaust gas recirculation). LNTs (Low NO_x Trap, sect. 1.5) have shown good NO_x reduction performance and durability while SCR (Selective Catalytic Reduction, sect.1.8), while offering also good NO_x reduction performance, offers more flexibility for fuel economy and reduction of CO_2 emissions. Manufacturers will likely choose the NO_x after-treatment technology based on a combination of cost, reliability, fuel economy, and consumer acceptance.

In large stationary applications (power plants, chemical industry, etc.), the issue of the NO_x removal is often accomplished through the post-treatment of the exhaust gases by means of the selective catalytic reduction (SCR) method. The main advantages got from the exploitation of this technology are its high efficiency and its reliability as well as stability of the catalytic reaction, but the high cost represents a considerable drawback as well as the need to have a proper temperature range of effective performances that obliges to place SCR unit. In addition to these general limits, a further drawback of ammonia SCR process lies in the low acceptability of such a technology in some different contexts, such as the food industry, due to the unpleasant smell and danger of the reactant molecule employed.

The extension to vehicle exhausts is very interesting too, provided that a proper catalytic system is developed in ordered to answer to the different requests of mobile NO_x sources. The most important difference in the operating conditions can be represented by the range temperature of interest for the process.

Hence, SCR devices could be even employed in mobile applications after adequate and calibrated system revision and modification in order to give effectiveness at lower light-off temperature (120 °C), since no solution seems to be viable with non-specific reducers (CO, HCs) mainly in the presence of O_2, for instance in diesel engines.

In particular, the development of "Low Temperature" NH_3-SCR catalysts that work in the range of temperature from 120 to 300 °C is considered an ideal way to control NO_x emissions also from stationary sources besides being an unavoidable necessity for vehicles. As a matter of fact, the reduction of the nitrogen oxides by means of ammonia in an oxidizing atmosphere has raised the need of the development of new catalysts, characterized by low cost and capability of ensuring high conversions, even at relatively low temperatures.

On the other hand, such a solution appears to be not viable for specific applications such as coffee roasters in food engineering, due to the unacceptance of ammonia (above all, for its odour in the plant), costs and safety reasons. Much more interesting could appear the attempt to prevent pollutant formation by developing intrinsically clean upstream processes.

In the present PhD, I focused my attention on the research of lower cost, versatility, environment-friendly nature and, of course, performer catalysts.

The work was devoted to synthesize, characterize and testing of MnO_x and MnO_x-CeO_2 catalysts proposed as innovative LT SCR catalysts, and a series of other catalytic systems for the selective oxidation of the organic compound emitted by an industrial roaster of coffee, in order to prevent the NO_x formation in such devices.

Generally, Mn is used in both reduction and oxidation reactions due to its various types of labile oxygen as well as to the presence of different structures and morphologies.

To the best of our knowledge, the optimal oxidation state of the metal has not been assessed for the SCR reaction, despite numerous studies dealing with the role of MnO_x and the deactivation of the catalysts.

Manganese oxides were investigated as catalysts for low-T SCR. Different MnO_x catalysts were prepared by means of different operating conditions and characterized, as well as tested in the SCR process under lab-scale conditions. The goal was thereafter to understand the suitable Mn oxidation state necessary for SCR performances and to study the nature of active sites, which does not seem to be well clarified to date although a great research effort in this field has been made in the last two decades.

The contribute of CeO_2 with MnO_x was investigate so the solution combustion route was chosen for synthesizing MnO_x-CeO_2 catalysts. The Mn/Ce molar ratio as well as quality and quantity of organic fuel in the reaction were investigated as key parameters and their influence on the structural, microstructural and superficial properties was studied. Moreover, the redox property of MnO_x-CeO_2 samples and the synergistic effect of Ce^{4+} and Mn^{n+} ions were analysed. All these properties were correlated to the catalytic activity in order to optimize the parameters for the best catalytic performance. In particular, we have already tried to correlate some chemical properties of the surface with the performances in the NH_3-SCR of pure MnO_x samples prepared by the SCS technique and in this paper a direct comparison among those results and the evidences obtained for the Mn-Ce catalysts will be performed.

On the other hand, and also in connection with a project sponsored by a coffee-maker company, the issue of removal of NO_x from roasting effluent was faced by studying catalysts and reactor conditions/configuration to prevention of the formation of nitrogen oxides itself.

The attention was given to catalysts consisting of nanoparticles of transition metals, such as copper, nickel, iron and manganese, which replace in part or in full the platinum

group catalyst, usally used in industrial context to abate the large mass of VOC emitted in the process. A homogenous dispersion and control the size of the nanoparticles on the substrate was necessary to develop the most effective catalysts and with a higher yield.

The total or partial replacement of the platinum group with nanoparticles of transition metal catalysts leads to a considerable reduction in costs and also to the strengthening of sustainability and a secure supply of raw materials for EU producers.

The replacement of the catalyst with an oxidative catalyst active and selective at low temperature allows both to reduce VOCs (Volatile Organic Compounds) and the CO is to reduce the nitrogen compounds to molecular nitrogen. For this purpose have been identified, from literature studies, catalysts were supported on matrices of micro and mesoporous.

Powder catalysts are the precursor materials deposited on the filters, so it is meaningful to analyse the intrinsic behaviour of the oxidative powder catalyst itself before investigating the oxidizing activity over the coated filters.

In the current PhD thesis, Chapter I describes about the state of art of pollutant emissions, NO_x, diesel engines, coffee and roasters, methods for abetment and prevention of NO_x.

The Chapter II involves Experimental methods: synthesis methods, characterizations and testing.

The Chapter III relates to articles either published during the PhD and Chapter IV is connected to the new catalyst for prevention of NO_x formation.

The Chapter V presents the conclusions.

Acknowledgments

Completion of this doctoral dissertation was possible with the support of several people. I would like to express my sincere gratitude to all of them.

First of all, I would like to express my special appreciation and thanks to my advisor Professor Dr. Raffaele Pirone, who has been a mentor for me with his valuable guidance, scholarly inputs and consistent encouragement I received throughout the research work.

This feat was possible only because of the unconditional support provided by Asst. Prof. Fabio Alessandro Deorsola: a person with an amicable and positive disposition, he has always made himself available to clarify my doubts and I consider it as a great opportunity to do my doctoral programme under his guidance and to learn from his research expertise.

I would like to thank you for encouraging my research and for allowing me to grow as a research scientist.

Thank you PhD Camilla Galletti, for all your help and support and your friendship, for your funny times and you scientific support.

I thank Professor Dr. Debora Fino, for the academic support and the facilities provided to carry out the research work in a new and interesting project.

Her advice on both research as well as on my career have been priceless.

I would also like to thank my team members, Professor Samir Bensaid, Asst. Professor Marco Piumetti, Professor Dr. Nunzio Russo for their scientific contribution.

Special thanks to my family. Words cannot express my gratitude to my mother, father and my husband, for all the sacrifices they have made on my behalf, for the care they had for me, for their attention and their support.

CONTENTS

Chapter I: State of art, pollutant emissions

1.1 NITROGEN OXIDES EMISSIONS

NO_x (NO, N_2O and NO_2) pollutants are emitted in high-temperature combustion by mobile sources as automobiles, trucks and various non-road vehicles (e.g., construction equipment, boats, etc.) as well as stationary sources such as power plants, industrial boilers, roasters, cement kilns, and turbines.

All fossil fuels are considered as main sources associated to combustion processes, where there is a transformation from chemical energy in fuels into thermal and mechanical energies. When air reacts with fuels at high temperature, NO_x are unavoidable involved into the reaction between oxygen and nitrogen in air [1, 2].

The pie chart below shows that road transport and energy production are the greatest sources of NO_x emissions in the EU during 2011.

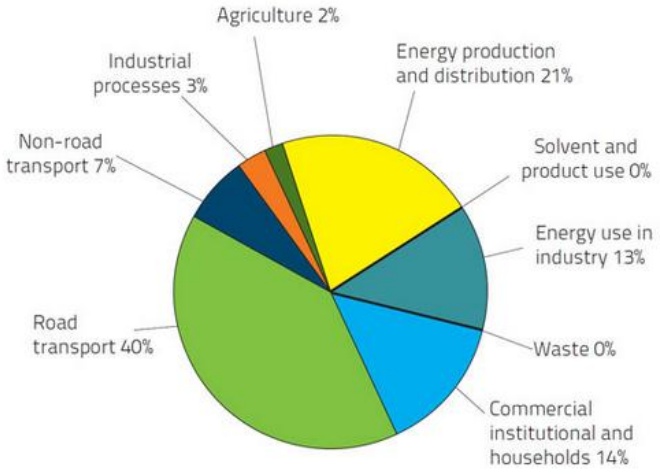

Fig.1.1:Source – European Union emission inventory report 1990–2011 under the UNECE Convention on Long-range Trans-boundary Air Pollution (LRTAP) –

When NO_x and volatile organic compounds (VOCs) react, in the presence of heat and sunlight, Ground-level Ozone is formed.

Ozone can be transported by wind currents, and can cause health impacts far from original sources. Other impacts from ozone include damaged vegetation and reduced crop yields. NO_x and sulphur dioxide could react with other substances up in the air to form acids (for example NO_x in contact with water forms nitric acid), which fall to earth as dry particles, rain, fog, or snow.

Nitrous oxide is a greenhouse gas. As well it contributes to ozone depletion in the stratosphere. Acid rain damages cause severe damaging to flora and fauna.

When nitrogen oxides and volatile organic compounds (VOCs) react to sunlight, creating a brown haze above cities formed a mixture of pollutants that is called photochemical smog. It tends to occur more often in summer, because that is when we have the most sunlight.

The main NO_x effects on human health concern breathing and the respiratory system and damage to lung tissue. In fact, nano-particles penetrate deeply into sensitive parts of the lungs and can cause or worsen respiratory disease such as emphysema and bronchitis, and aggravate existing heart disease.

Another aspect is the water quality deterioration that concerns the increase of nitrogen loading in water bodies, modifying the chemical balance of nutrients used by aquatic plants and animals.

1.1.1 Reaction mechanisms

The nitrogen oxides formation takes place according to three different mechanisms:

– Thermal NO_x: formed directly for the combination of O_2 and N_2

– Prompt: originated on the flame front due to a not perfect mixing

– Fuel NO_x: derived from N–containing molecules

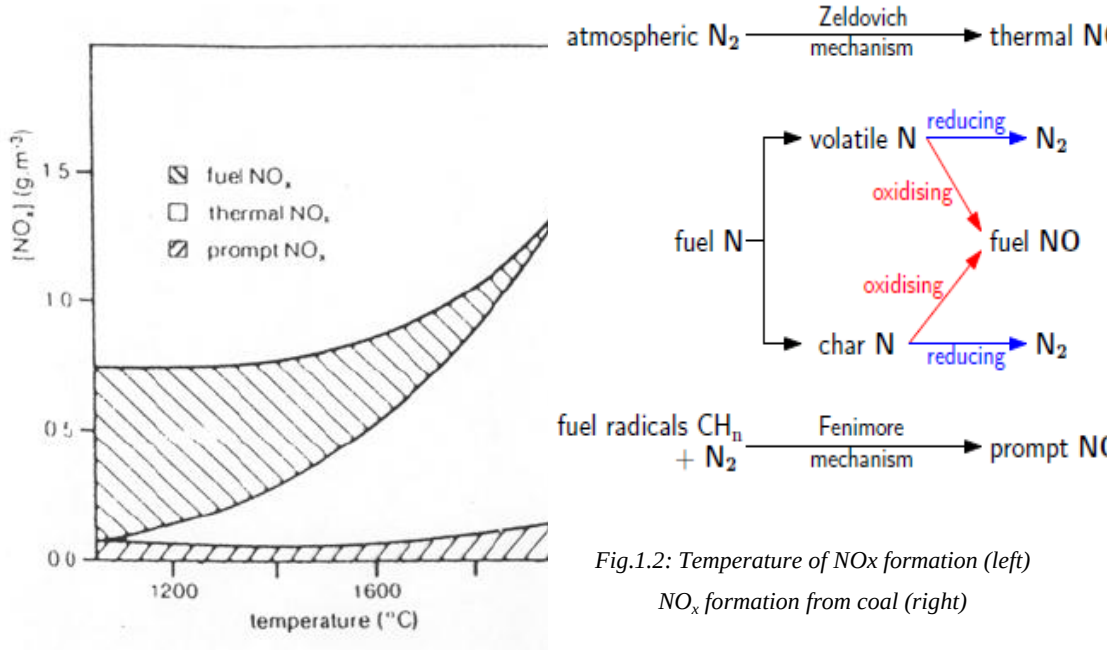

Fig.1.2: Temperature of NOx formation (left)
NO_x formation from coal (right)

1.1.1.1 Thermal NO_x

Between all the possible ways, thermal NO_x is the most relevant. N_2 and O_2 are combined, during combustion, following the radical mechanism of Zeldovich [8]:

$$N_2 + O^{\bullet} \rightarrow NO + N^{\bullet} \quad (1.1)$$

$$N^{\bullet} + O_2 \rightarrow NO + O^{\bullet} \quad (1.2)$$

$$N^{\bullet} + \mathrm{OH} \rightarrow NO + \mathrm{H} \quad (1.3)$$

This mechanism requires temperatures exceeding 1800 K in order to get the conditions of an appreciable kinetic. Considering the high temperature required, the need for equally high activation energy is supposed. The rate determining step is the break of the triple bond present in the molecule of N_2. The control of this reaction can be achieved by decreasing the temperature, the contact time and varying the concentration of the reactants. For reasons of flame stability, combustion performed in excess of air. With the increase of the quantity of air, the volume is increased, with the consequent decrease of the flame temperature. From Figure 1.3 it is possible to observe how different pollutants are produced by combustion. These exhibit very different patterns depending on the ratio combustion air/fuel, better defined as λ (Fig. 1.4). The choice of the ratio to be used is essential for determining the quantities, and the species, of products to be treated. From the viewpoint of combustion efficiency, ideally it works in lean conditions, then with $\lambda > 1$. It might, therefore, think to use a large excess of air to reduce NO_x emissions, but this would cause instability of the flame. Working, however, in rich conditions ($\lambda < 1$) less nitrogen oxides but many (HC, CO) will be produced.

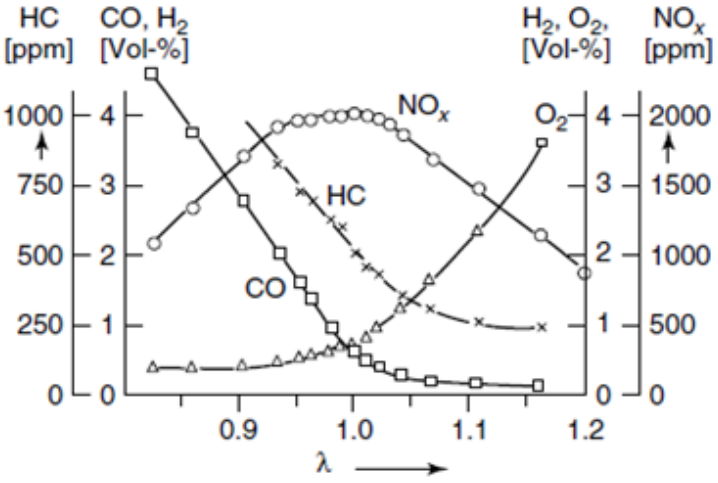

Fig. 1.3: pollutant emissions connecting to air/fuel ratio λ

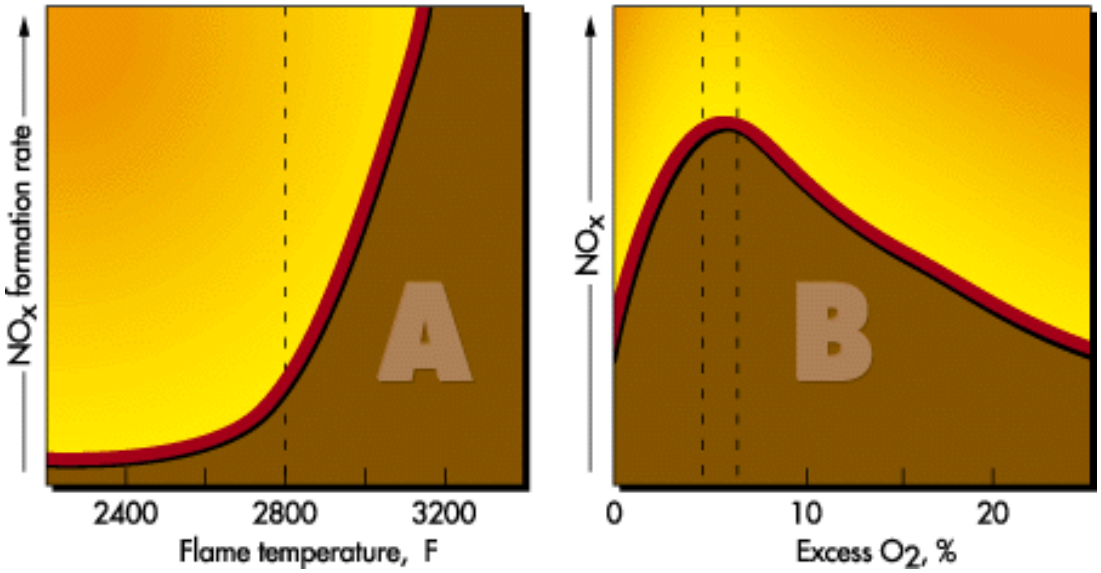

Fig. 1.4: NO_x formation temperature vs flame temperature (left) or vs Excess O_2 (right)

1.1.1.2 Prompt NO_x

On the flame front, NO_x concentrations are higher than the equilibrium value. In this area, indeed, the mixing is not perfectly homogeneous and causes the formation of many unburned hydrocarbons, present in the form of radicals.

They react readily with atmospheric nitrogen giving hydrocyanic acid as a reaction intermediate, which, in turn, is oxidized to NO_x in the presence of air.

As reported in Fig. 1.5 the radical nitrogen (N•) continue the reaction and it contributes to the formation of thermal NO_x:

$$HC^{\bullet} + N_2 \rightarrow HCN + N^{\bullet} \quad (1.4)$$

$$H_2C^{\bullet} + N_2 \rightarrow HCN + NH^{\bullet} \quad (1.5)$$

$$N^{\bullet} + \mathrm{OH} \rightarrow NO + \mathrm{H}^{\bullet} \quad (1.6)$$

Through a careful premixing, and a lean mixture ratio, it is possible to reduce the quantity of nitrogen oxides originated by this process.

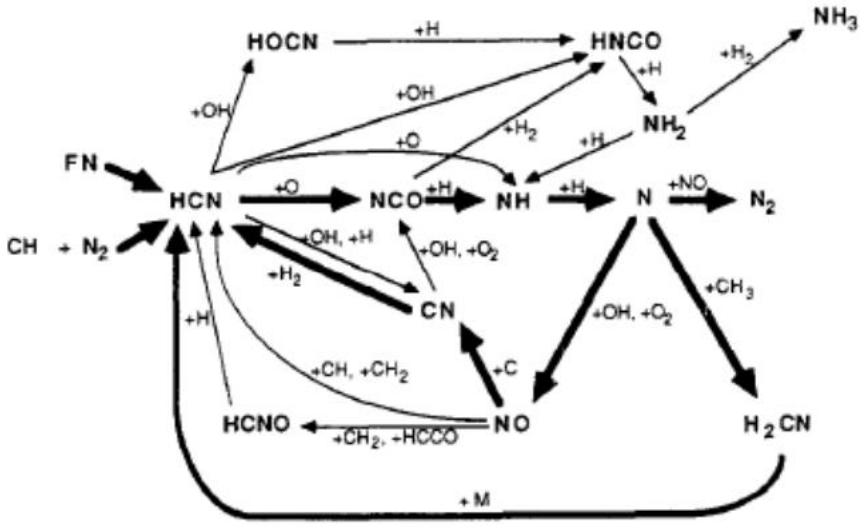

Fig. 1.5: Reaction path diagram illustrating the major steps in prompt NO_x formation and conversion of fuel nitrogen (FN) to NO.

1.1.1.3 Fuel NO_x

These NO_x molecules come directly from nitrogen in the fuel so the Fuel NO_x conversion is referred to *Fuel-Bound Nitrogen* (FBN) during the combustion.

This nitrogen can be easily oxidized, much more than the atmospheric one: even before 1200 °C, temperature at which the first thermal NO_x begin to form, the process emits already a considerable quantity of NO_x from the fuel.

This category of nitrogen oxides mainly comes from heavy oils and coal containing not negligible (between 0.2 and 5% w/w) amounts of nitrogen.

Then, the combustion of methane (for example) would reduce to zero the formation of this type of NO_x. How the exposure to air pollutant emissions and adverse human health impacts are connected is now well established. Therefore, the changes are necessary to reduce the population exposure to the major air pollutants and toxic species in urban environments, and also, reduce emissions from the vehicle fleet.

According to an analysis by the Health Effects Institute, ‘‘the composition of diesel exhaust varies considerably depending on engine type and operating conditions, fuel, lubricating oil, and whether an emissions control system is present.”

So, it is clear that NO_x is toxic and its regulation has been becoming more stringent all over the countries.

1.2 EMISSIONS AND REGULATIONS

The increase in the industrial activity requires continuous improvement of technologies for the reduction of pollutants commonly issued and to this aim, the study of catalytic systems has assumed increasing importance over the years.

The pollutants are worldwide continuously emitted, both from stationary sources, such as homes, small and large thermo-electric plants, and from mobile sources, such as vehicles in the first place. The graph illustrates the typical ranges of emissions of pollutants from stationary sources, when these do not provide any abatement system (Tab. 1.1).

Table 1.1: Industry and gas emissions

Industry	*Source*	*Fuel type*	*Gas emissions*	*Levels/ppmv*[a]
Heat and power generation	Boiler	Coal	NO_x	150–700
			SO_x	300–2500
			Particles[b]	10 mg Nm^{-3}
		Oil/Pet coke	NO_x	200–500
			SO_x	1000–5000
			Particles[b]	10 mg Nm^{-3}
		Biofuel	NO_x	100–300
			SO_x	0–50
	Gas turbine	Gas	NO_x	15–50
			CO	1–200
	Diesel engine	Oil	NO_x	1000–1500
			SO_2	100–2000
			CO	100–1000
			Hydrocarbons	50–500 ppm C_1
Incineration	Municipal waste, sewage sludge		NO_x	150–300
			SO_2	10–100
			CO	5–20
			Dioxins	1–10 ng Nm^{-3}
			Particles[b]	
Process Industry	Nitric acid plants		NO_x	100–2000
			N_2O	100–1000
			HNO_3	Trace
			NH_3	Trace
	Cement calcination	Gas + solid	NO_x	100–3000
	Ethylene burners	Gas	NO_x	10–100
	Smelters	Gas	SO_x	20 000–100 000
			NO_x	10–100
			Heavy metals	<1 (after scrubber)
	Coal gasification	Coal	NO_x	10–50
			SO_x	30 000–100 000
	Industry heaters	Gas	NO_x	10–100
	Glass furnaces	Gas	NO_x	200–500
			SO_2	500–1500
	FCC catalyst regeneration	Gas	NO_x	50–2000
	Printing industry, etc.	Solvents	VOC	1–10 g Nm^{-3}

As regards the reduction of nitrogen oxides emissions, this could occur by different methods which can be summarized in table 1.2.

Table 1.2: Mechanism for NO_x emissions reduction.

Mechanism	*Technique*	*Efficiency/%*
Reduced peak temperature	Water injection	40–70
	Flue gas recirculation	40–80
	Burner out service	30–60
	Less excess air firing (LEA)	15–20
Limiting thermal NO_x formation	Oxyfuel	70–90
Lower residence time at peak temperature	Low-NO_x burners, overfire air, staged combustion, rotating opposed fired air, etc.	30–70
Catalytic reduction of NO_x	Selective catalytic reduction (SCR)	70–98
	Selective non-catalytic reduction (SNCR)	25–50
	Adsorption and reduction NO_x	60–90

Table 1.3: EU Emission Standards for Passenger Cars [dieselnet]

Stage	Date	CO	HC	HC+NOx	NOx	PM	PN
		g/km					*#/km*
Compression Ignition (Diesel)							
Euro 1†	1992.07	2.72 (3.16)	-	0.97 (1.13)	-	0.14 (0.18)	-
Euro 2, IDI	1996.01	1.0	-	0.7	-	0.08	-
Euro 2, DI	1996.01[a]	1.0	-	0.9	-	0.10	-
Euro 3	2000.01	0.64	-	0.56	0.50	0.05	-
Euro 4	2005.01	0.50	-	0.30	0.25	0.025	-
Euro 5a	2009.09[b]	0.50	-	0.23	0.18	0.005[f]	-
Euro 5b	2011.09[c]	0.50	-	0.23	0.18	0.005[f]	6.0×10^{11}
Euro 6	2014.09	0.50	-	0.17	0.08	0.005[f]	6.0×10^{11}
Positive Ignition (Gasoline)							
Euro 1†	1992.07	2.72 (3.16)	-	0.97 (1.13)	-	-	-
Euro 2	1996.01	2.2	-	0.5	-	-	-
Euro 3	2000.01	2.30	0.20	-	0.15	-	-
Euro 4	2005.01	1.0	0.10	-	0.08	-	-
Euro 5	2009.09[b]	1.0	0.10[d]	-	0.06	0.005[e,f]	-
Euro 6	2014.09	1.0	0.10[d]	-	0.06	0.005[e,f]	6.0×10^{11} [e,g]

* At the Euro 1..4 stages, passenger vehicles > 2,500 kg were type approved as Category N_1 vehicles
† Values in brackets are conformity of production (COP) limits
a. until 1999.09.30 (after that date DI engines must meet the IDI limits)
b. 2011.01 for all models
c. 2013.01 for all models
d. and NMHC = 0.068 g/km
e. applicable only to vehicles using DI engines
f. 0.0045 g/km using the PMP measurement procedure
g. 6.0×10^{12} 1/km within first three years from Euro 6 effective dates

Table 1.4: EU Emission regulation on coal fired power plants

NO_x ELVs mg/Nm^3	LCP Directive			Industrial Emissions Recast Proposal	
	MWth	existing "old new"	"new new"	existing	new
coal/lignite	50 - 100	600	400	300 (450)	300 (400)
	100 - 300		200	200	200
	300 - 500			200	150 (200)
	> 500	500 →200(>2016)			
liquid fuels	50 - 100	450	400	450	300
	100 - 300		200	200	150
	300 - 500			150	100
	> 500	400			
natural gas (boilers)	50 - 300	300	150	100	100
	300 - 500		100		
	> 500	200			
gas turbines	natural gas	not covered	50 (75) (*)	50 (75) (*)	50 (*)
	other gases		120	90	50
gas engines	not covered			100	75

(*) efficiency to be taken into accounts in some cases.

As reported in Tab. 1.3 and Tab 1.4, it is clear that the European and global tendencies lead to lower emission standards.

In order to satisfy the upcoming regulations, it is necessary to develop more efficient technologies which reduce formation of pollutants (primary techniques) and finally improved abatement of the pollutants emitted in the flue gases (secondary techniques).

There has been much interest in reducing NO_x from engines in terms of fuel injection strategies [4, 5], exhaust gas recirculation [6] and catalytic reactions [7], among which selective catalytic reduction (SCR) has been successfully applied in stationary applications such as boilers and power plants.

In large stationary applications the issue of the NO_x removal is accomplished through the post-treatment of the exhaust gases by means of the selective catalytic reduction (SCR) method.

1.3 STATIONARY AND NON-STATIONARY POWER PLANTS

1.3.1 Plants not stationary

In addition to stationary plants, it has been shown above that even the non-stationary plants are a remarkable source of emission of different types of pollutants (see Figure 1.1).

Since the '70s, an increase in the use of cars in the most industrialized cities caused a rapid and steady deterioration in air quality, leading to an increase in the concentrations of nitrogen oxides (NO_x), unburned hydrocarbons (HC), carbon monoxide (CO), sulphur oxides (SO_x), and particulate matter (DP) contained in the exhaust gas [9].

The internal combustion engine uses as fuel a mixture of hydrocarbons C_xH_y, which react with the combustion air leading predominantly to the formation of carbon dioxide and water vapour, and to a lesser extent to pollutants, in the order of 1-3% in volume.

The combustion process is described by the reaction:

$$CxHy + (x + \frac{y}{4})O_2 \rightarrow xCO_2 + \frac{n}{2}H_2O \qquad (1.7)$$

Carbon dioxide and water vapour are the main products; however, it must be considered that the incomplete combustion of the reaction also causes the emission of some unburned hydrocarbons, such as alcohols, aldehydes, and especially carbon monoxide.

Moreover, since most of fossil fuels present some percentages of sulphur and nitrogen, the following of combustion will cause the formation also of sulphur oxides (mainly SO_2) and nitrogen oxides, these mainly consisting of NO and to a lesser part of N_2O.

In addition, since during the combustion temperatures greater than 1700 K is reached; when the reaction between the oxygen and the nitrogen is present in the air the result is the formation of nitrogen oxide.

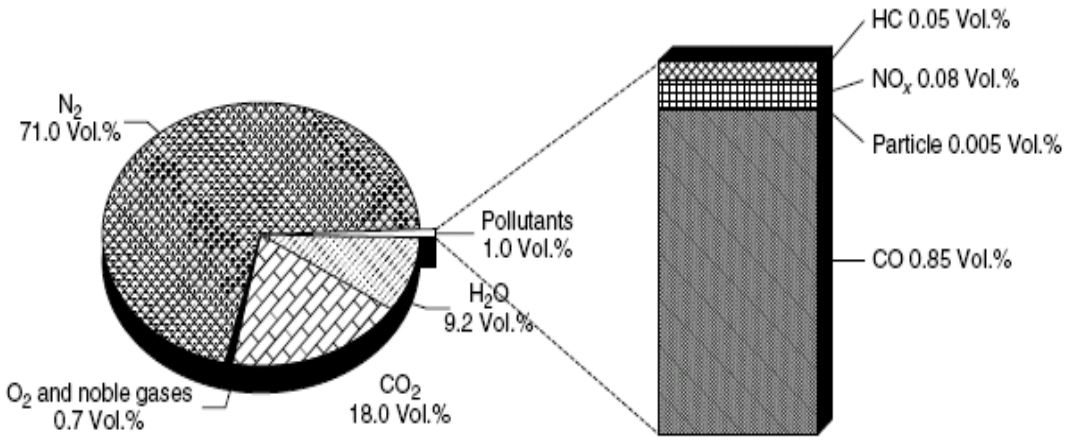

Fig. 1.6: percentage of pollutants

Of course the percentages of carbon monoxide, unburned hydrocarbons (responsible for photochemical smog) and nitrogen oxides generated depend on both the initial composition of the fuel and the characteristics with which the reaction takes place in the combustion engine; at these, however, must add an additional pollutant that is generated in the process: the particulate.

Particulate matter, generally referred to as PM, is constituted by solid carbonaceous nanoparticles, and a soluble organic fraction, often referred to as SOF (soluble organic fraction).

The order of magnitude of the different pollutants contained in the exhaust gas of an internal combustion engine is shown in Figure 1.6. It is necessary to specify here, however, that for petrol engines, that is, those spark ignited, the emission of SO_x and particulate is more negligible, due to the low content of them in gasoline; vice versa, in diesel engines ignited by compression emissions of CO are negligible, since combustion takes place here with a strong excess of air.

The formation of these pollutants varies depending on the type of engine. In fact, based on the mode with which the combustion process is started, different products are obtained:

- Spark ignition engines (petrol) engines emit carbon monoxide (CO), unburned hydrocarbons and $NO_{x,}$
- Engines and compression ignition (diesel) engines emit NO_x, SO_x, HC and particulate.

If the duration of the cycle is instead considered, the engines can be divided into:

- 2-stroke engines: is necessary only one crankshaft revolution to describe a whole cycle; characterized by high emissions of HC, CO, but reduced release of NO_x.
- 4-stroke engines: are necessary two crankshaft revolutions to describe a whole cycle; characterized more NO_x emissions compared to 2 times.

As regards gasoline engines, they employ the so-called "three way catalyst" which is flanked generally to the recycle systems of the burnt gases (EGR), which allow reducing the maximum temperature in the combustion chamber.

The first emission controls were made with the introduction of catalysts based on platinum, iridium and ruthenium, which guarantee excellent efficiency in the oxidation of different types of pollutants.

The oxides of the last two elements are, however, very volatile and difficult to be deposited on a support without causing their loss. This brought the platinum to be one of the main components of this first type of catalysts [9].

Currently, in the automotive industry, the exhaust gas treatment system is divided into several parts, given the variety of polluting compounds to treat. In general, considering a diesel engine, we can distinguish:

- DPF (Diesel Particulate Filter) for removal of the particulates
- DOC (Diesel Oxidation Catalyst) for the oxidation of the unburnt CO and CO_2
- SCR for the catalytic reduction of NO_x
- LNT for the catalytic reduction of NO_x

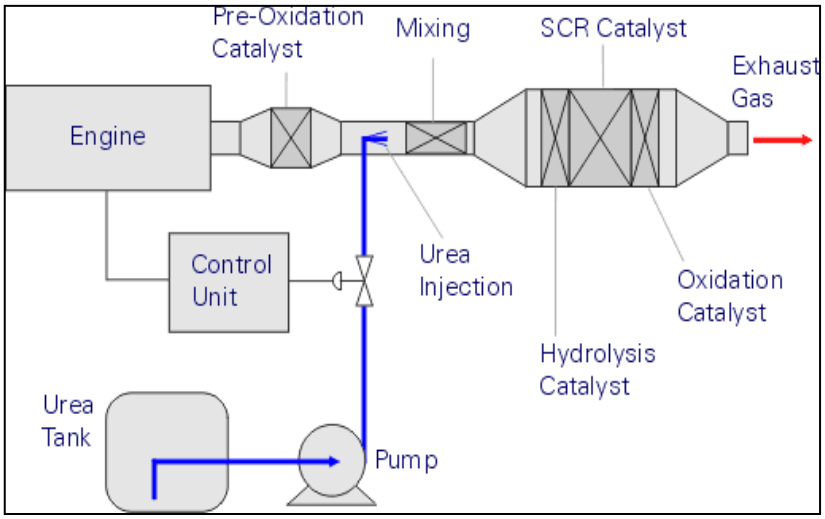

Fig. 1.7: Scheme of after-treatment system.

The gas mixture passes, first, through the DOC, where oxidation of CO, NO and HC to CO_2, NO_2 and water takes place, and then through the particulate filter that holds the diesel particulate. In the moment in which the DPF has a high pressure drop, the regeneration is carried out, through the post fuel injections, in order to cause combustion of the particulate blocked. As a last unit is placed the SCR (Fig. 1.7).

The operating principle of this technology involves the use of ammonia for the reduction of NO_x to N_2 and will be described in great detail in the next chapter. It is the most affordable and efficient for the overthrow of a type of pollutant, which, until the 2000s (with the introduction of Euro 3), did not know how to cope.

Restrictions on emissions of NO_x, before that date, were, in fact, incorporated within the limits on unburned, leaving free choice to the manufacturer on how to carry out the abatement and focus more on what species.

The arrangement of the various units has to follow the required sequence. The DOC in the oxidation of the various pollutants leads to the formation of NO_2, strongly oxidizing compound, which facilitates the removal of both the unburned and of the particulates, both the NO_x themselves through the fast SCR reaction.

To ensure the complete removal of NO_x, the unit SCR must be therefore placed as last. Hence the need of a catalyst which ensures high conversions at low temperatures. The research has oriented towards the development of new catalysts based on oxides of transition metals, very active and relatively cheap.

1.3.2 Stationary power plant

In stationary applications the problem of removing NO_x is addressed through prevention systems of formation (primary technologies) and through post-treatment systems of exhaust gases (secondary technologies) [4].

1.3.2.1 Roasters: Coffee Roasting Processes and Emissions

The roasting process consists in a phenomenon of heat and material transfer superimposed to endothermic reactions and exothermic and dependent on the time and the temperature.

So it transforms the chemical and physical properties of green coffee beans into roasted coffee products ready to be employed for the preparation of the coffee beverage.

The changes experienced macroscopically from the coffee bean are:

1. Colour of the grain: from green to light yellow which then darkens until the final colour reddish brown
2. Surface of the grain: oil spill that make it glossy
3. Structure of the grain: it becomes porous due to the strong growth of CO_2 that takes place between 7 and 12 minutes of roasting [10].
4. Volume of the grain: almost doubles from 0 to 9 minutes of roasting. This increase in volume is due to the release of water, CO_2 and volatile organic compounds from the beans to the gas phase [10].
5. Weight of the grain: decreases by about 15-20%. The weight loss corresponds to a slow release of water and volatile substances [10].
6. Humidity: decreases regularly in the course of roasting up to values less than 1%, then it depends on if cooling is effected by water.
7. Loss of organic reactions of decomposition over 160 °C of carbohydrates, the chlorogenic acids, of trigonelline and amino acids, with strong growth of CO_2 that continues for some time thanks to the development of Maillard reactions [11,12].
8. Volatiles from about 350 in the green coffee have been identified over 850 after roasting [10, 13-16].
9. Aromatic substances: there are about 25, concentrated in the oils of coffee (about 1 g/kg), and their mixture characterizes the typical aroma of roasted coffee.

The vast majority of coffee is roasted commercially on a large scale, but small-scale commercial roasting has grown significantly with the trend toward "single-origin" coffees served at specialty shops.

Some coffee drinkers even roast coffee at home as a hobby in order to both experiment with the flavour profile of the beans and ensure them of the freshest possible roast.

Four steps can be identified during the roasting process: i) drying; ii) development of the brown colour; iii) decomposition and iv) full roasting.

The green coffee beans are transferred to feed hoppers that charge beans to the roaster.

The roaster may operate on a batch or continuous basis.

At a temperature of 50-55 °C, the proteins denature and the water evaporates. Starting from 100 °C, the browning phenomenon occurs due to the pyrolysis (degradation of organic compounds) and water continues to evaporate, leading to beans swelling.

At 140 °C the decomposition of organic compounds due to the reaction between sugars and proteins starts from the bean surface (also known as Maillard reactions), causing the development of hundreds of volatile organic compounds (VOC) that characterize the typical scent of the roasted coffee.

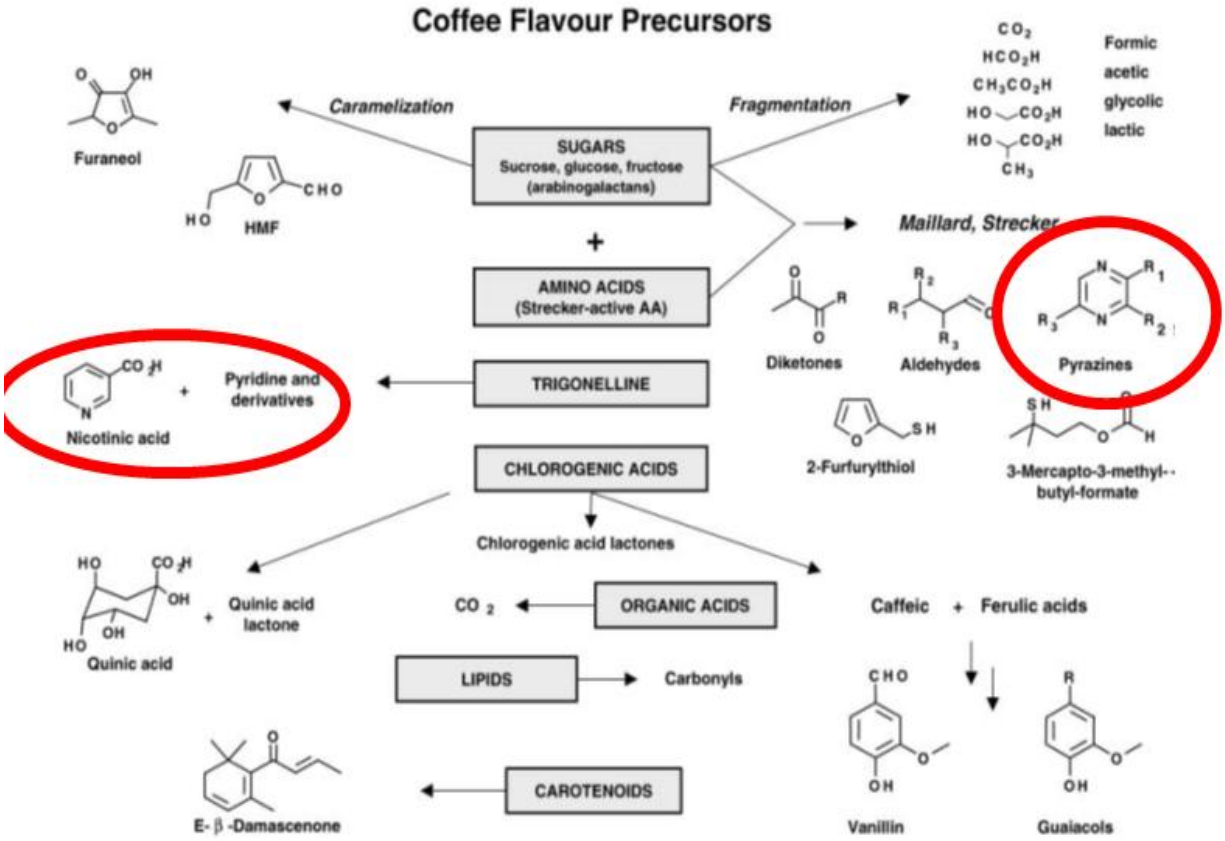

Fig. 1.8: Coffee flavour precursors

Table. 1.5: Sugar content of green Arabica and Robusta coffee

Coffee	Sucrose	Fructose	Glucose	Mannose	Arabinose	Total
Arabica						
Colombia	8.2	0.15	<0.01	ND	<0.01	8.35
Colombia	8.3	0.07	0.3	ND	0.05	8.72
Salvador	7.3	0.02	<0.01	ND	0.09	7.43
Brazil	6.65	0.15	<0.01	0.02	0.15	6.87
Brazil	6.3	0.15	<0.01	0.1	0.07	6.62
Kenya	8.45	0.02	<0.01	<0.01	0.07	8.55
Kenya	7.05	0.03	<0.01	0.06	0.07	7.21
Tanzania	7.55	0.2	0.45	0.08	0.05	8.33
Ethiopia	6.3	0.4	0.4	ND	<0.01	7.1
Ethiopia	6.25	0.25	0.45	ND	0.04	6.99
New Guinea	7.7	0.07	<0.01	ND	0.06	7.84
East India	6.5	0.04	<0.01	ND	0.1	6.64
Robusta						
Madagascar	3.9	0.25	<0.01	ND	0.12	4.29
Cameroun	3.2	0.3	<0.01	ND	0.09	3.6
Cote d'Ivoire	3.4	0.35	0.2	ND	0.09	4.06
Cote d'Ivoire	0.9	0.55	0.5	ND	0.15	2.1
Indonesia	1.25	0.25	<0.01	ND	0.05	1.56
Indonesia	3	0.2	0.35	0.06	0.07	3.68
Philippines	4	0.4	0.35	0.02	0.1	4.87
Philippines	4.85	0.35	0.5	ND	0.04	5.74

Expressed as % dry basis (Source: Bradbury 2001).

Over 200 °C the decomposition includes the inner part of the beans involving the popping and cracking phenomena. The percentage of water is about 1-3 %. From 200 °C the reaction becomes exothermic, the oils are released and the surface of the beans presents itself with the typical red-brownish colour.

At higher temperature (>240 °C) the coffee bean burns producing black soot. The design of the roasters and time-temperature profiles influence the flavour. Roasters are typically horizontal rotating drums that tumble the green coffee beans in a current of hot combustion gases; the roasters can be indirect- or direct-fired.

The most important mode of heat transfer is the convection that determines the rate and uniformity of roasting (Baggenstoss et al. 2008). The effects of time-temperature profile on coffee aroma properties have been reported in Fig. 1.9.

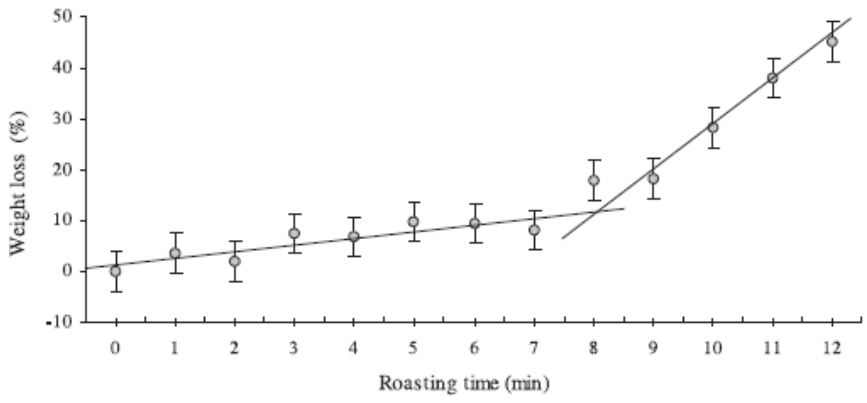

Fig.1.9: Weight loss vs roasting time

The weight loss curve presents a behaviour described by two distinct rates. The roasting period between 0 and 7 min can be described by a straight line with a relatively small slope. The weight loss in this period corresponds to a slow release of water and volatiles.

The roasting period from 7 to 12 min can be described by a straight line with a steeper slope, corresponding to an intensive evolution of CO_2 and organic compounds out of the beans.

It was reported [10] that the CO_2 release rate rapidly increases when there is a significant decrease in the water release rate. Based on this information, and on the analysis of the curves for gas temperature profile and for the beans volume variation during roasting, it can be inferred that the pyrolysis reactions become expressive in the roasting period from 5 to 6 min.

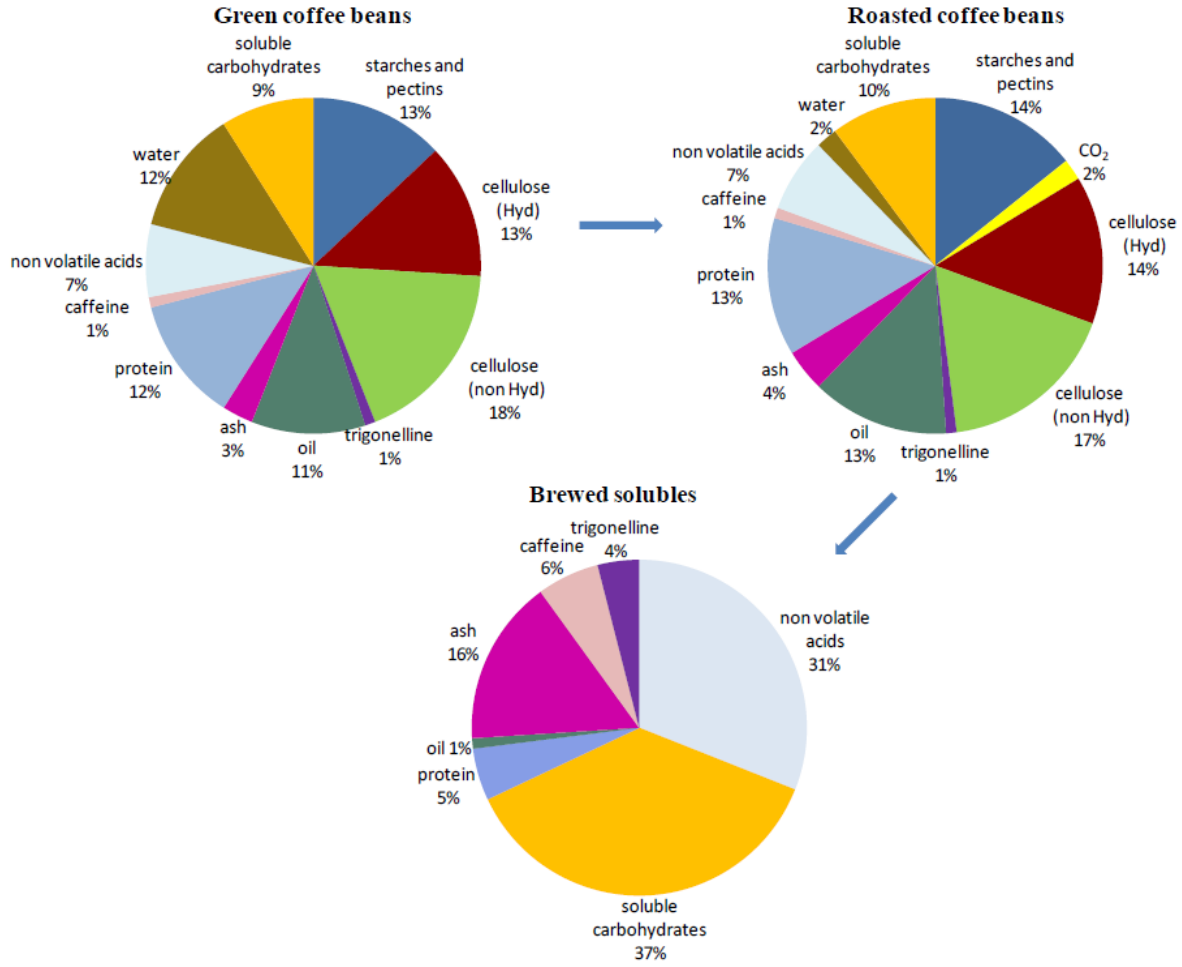

Fig.1.10: an example of how change the composition of the coffee bean during the different steps.

The roasting time, as well as the temperature of the roaster and subsequently the flow rate of the air passing through the roaster, is fundamental parameters of the

process. They represent the core of the know-how of the coffee manufacturer, deriving from an experience gained in years and years of practice, and are the keys for achieving each single feature (smell, taste, etc.) of the roasted coffee and consequently of the coffee beverage. Lyman et al. observed that the medium roasted process (6.5 min to the onset of the first crack and 1.0 min to the onset of the second crack) resulted in balance with citrus taste. Instead the "sweating process" (4.5 min to the first crack and 6.5 min to the second crack) resulted in non-uniform bean colour. Reducing the heating rate further by using the "baked process" (11 min to the first crack and 18 min to the second crack) produced coffee of "flat, woody with low brightness and acidity" (Lyman et al. 2003). It is possible to summarize that all physical characteristics such as temperature, colour, and weight-loss are indicators of roast degree. The process conditions as temperature of the roasters and time are fundamental to obtain the desired flavour.

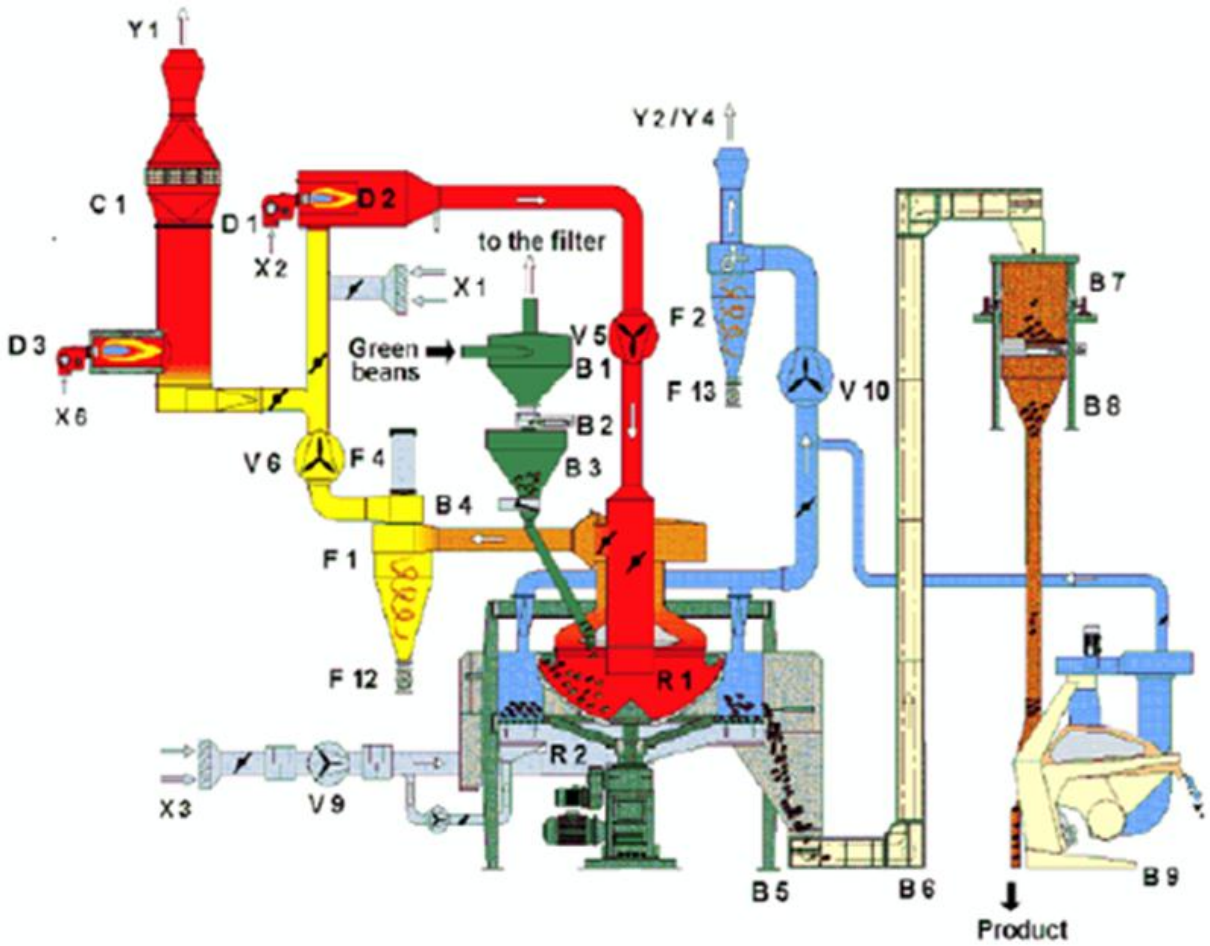

R1 = Roaster
R2 = Cooler
D3 = Burner catalyser
X6 = Supply air – burner catalyser
B3 = Roaster bin
D1 = Burner
D2 = Heating furnace
X3 = Supply air - cooler
B2 = Feeding slide
V6 = Roasting exhaust air fan
X1 = Supply air - roaster
X2 = Supply air - burner
B1 = Feeding bin
V5 = Roasting supply air fan
B4 = Feeding flap

V9 = Cooling supply air fan	B5 = Charging bin	V10 = Cooling exhaust air fan
Y1 = Exhaust air - roaster	B6 = Bucket elevator	Y2/Y4 = Exhaust air cooler/destoner
B7 = Receiving bin	B8 = Scale bin	B9 = Destoner
F1 = Roasting cyclone	F2 = Cooling – destoner cyclone	F4 = Rupture disc
C1 = Catalyser	F12 = Cellular wheel sluice	F13 = Cellular wheel sluice

Fig.1.11 Scheme of a typical batch roasting plant.

In Fig. 1.11 a typical batch roasting plant is reported. The main burner is devoted to the coffee roaster in order to heat the air up to about 450 °C, passing in the roaster and transferring its heat to the coffee beans for the endothermic roasting process.

Gaseous and particulate matter (PM) emissions occur during the step.

Particulate emissions are composed primarily of coffee chaff (the outer skin of the coffee bean) that is released when the coffee beans swell during roasting.

Most of the chaff released during roasting is light enough to be carried off with the roaster exhaust.

The gaseous emissions result from the breakdown of the sugars and oils present in the green coffee beans and include aldehydes (e.g., formaldehyde, acetaldehyde), organic acids, phenols, and other hydrocarbons. In addition, nitrogen oxides and carbon monoxide emissions occur as a result of the combustion of natural gas, which is typically used to fuel the roaster.

So part of the exhaust gases could be re-cycled in a loop to the primary burner in order to decrease the energy consumption and the emission of pollutants too instead, the remaining flow is send to the exhaust pipe where, before emitted in the atmosphere, it is subject to a catalytic oxidation in order to convert the pollutants (CO, VOC, etc.) into CO_2, at a temperature of about 450 °C.

In the next step the beans are quenched with a water spray to halt the roasting process. This operation happens in a cooler, in which the air is blown over and/or through the beans and to improve the velocity they are agitated.

Due to the elevated temperature of the roaster, the water applied is emitted as steam. It contains PM and, moreover, traces of the pollutants released during the roasting process.

Due to the necessity to separate beans from other undesired material as well as stonesand other waste materials is used a destoner, which consists in an air classifier. The primary pollutant emitted during these two processes already

described is particulate matter as coffee chaff. The last one is removed with cyclone collectors.

Catalytic or thermal oxidizers that are downstream of cyclones typically control gaseous emissions from coffee roasters.

To reduce the emissions re-circulating roasters where introduce: a redirect portion of the roaster exhaust back through the burners, resulting in the oxidation of some of the pollutants.

The division typically uses 95% control efficiency for oxidizers. Thus, if necessary, the temperature of the exhaust gases of can be raised by a secondary burner, committed to the oxidation converter.

Table 1.6: CO and NO_x emissions for a representative roasting cycle in different points of the roasting plant.

	Sampling point	CO [mg/Nm^3]	NO_x (as NO_2 eq) [mg/Nm^3]
Coffee roasting	After main burner	433	114
	After roaster	1055	59
	Before catalytic converter	1751	141
	After catalytic converter	12	421
Empty roaster	Before catalytic converter	141	40

The kind of roasting cycle performed and on the kind of coffee beans employed affect the quality and quantity of polluting molecules contained in the exhaust gas. Table 1.6 illustrates CO and NO_x during an entire cycle of roasting.

It is clear that as a first step carbon monoxide is generated by the main burner in the lower quantity and subsequently the main part is released during the roasting of the coffee beans.

It is likely to suppose that the CO emission is associated with the development of VOCs.

The catalytic converter completely performs its oxidative action, since carbon monoxide as well as VOCs is fully converted to CO_2, with a negligible amount of carbon monoxide at the pipe end.

But unfortunately the catalytic oxidation concerns also the nitrogen-containing organic molecules, mainly pyridine, pyrazine and caffeine, deriving from the Maillard reactions during coffee roasting.

The sucrose is split into reducing sugars such as glucose and fructose which, in turn, react with free amino acids and free amino groups of the proteins in the Maillard reaction, forming aminoketones and/or amminoaldose. These, by

successive reactions produce compounds which react further in a complex cascade of reactions leading to numerous volatile compounds.

The nitrogen-containing compounds, which are formed by this series of reactions (circled in Fig.1.7), are: pyridines and derivatives, pyrazines and nicotinic acid.

For example, among the pyrazines have been identified: 2-Methyl-pyrazine, 2,5-Dimethyl-pyrazine, 2,6-Dimethyl-pyrazine, Ethyl-pyrazine, 2,3-Dimethyl-pyrazine, 2-Ethyl-6-metilpyrazine, 2-Ethyl-S-metilpyrazine, Trimethyl-pyrazine, 2,6-diethyl-pyrazine, 2,3-diethyl-pyrazine [12]. It was measured a pyrazine content of about 57 mol per kg of coffee, while the amount of 2-methylpyrazine is equal to 695 µmol/kg [17].

The oxidation of these molecules causes the formation of nitrogen oxides, specifically NO and NO_2.

Thus the nitrogen oxides emitted in the atmosphere are not produced directly in the roaster but are a consequence of the converted employed for the abatement of carbon monoxide and VOCs.

It turned out that the substances emitted from roasting green coffee are dominated by the presence of alcohols, which represent 93% of the total concentration in Arabica and 53% Robusta.

The methanol is by far the most abundant VOC in both mixtures: Arabica (90%) and Robusta (44%). The groups most abundant compounds in descending order of importance are the aldehydes (1-3%), hydrocarbons and organic acids (0.2-0.6%) [11].

Additionally, the degradation of sucrose (in particular the oxidation of furfural) leads to the formation of furans, among which were identified: 5-Methyl-2-vinilfuran, 2-Methyl-tetrahydro-3-furanone, 2-methyl-3-[2H]-furanone, 2-Furfural, furfuryl-metanoate, 5-Metill-2-furfural, 2-furfuryl-alcohol [12].

The composition of the gas roasting also depends on the type of mixture.

For example, mixtures consisting of Arabica (A) and Robusta (R) in different ratios were analysed, showing that that the ratio of the mixtures influence the content of sugar and other compounds responsible for the formation and emission of VOCs [18].

In fact, when the sugar content is high, the pyrazines, pyridines and furans are formed in large amounts compared to the coffee with just one flavour.

The different ratios affect 20 chemical species such as aldehydes, ketones, thiazoles, thiophenes, phenolic compounds, pyridine, pyrazine, etc.

It has been reported that in the mixture A20:R80 was found an increased amount of compounds consisting of sulphur, while furans, aldehydes and pyrazines are more abundant in the mixture A80:R20.

As reported from fig.1.12 to fig. 1.15, the presence or not of pollutants is more evident by observing the graphs of the CO and NO_2 emission trend for some batches of a representative roasting cycle.

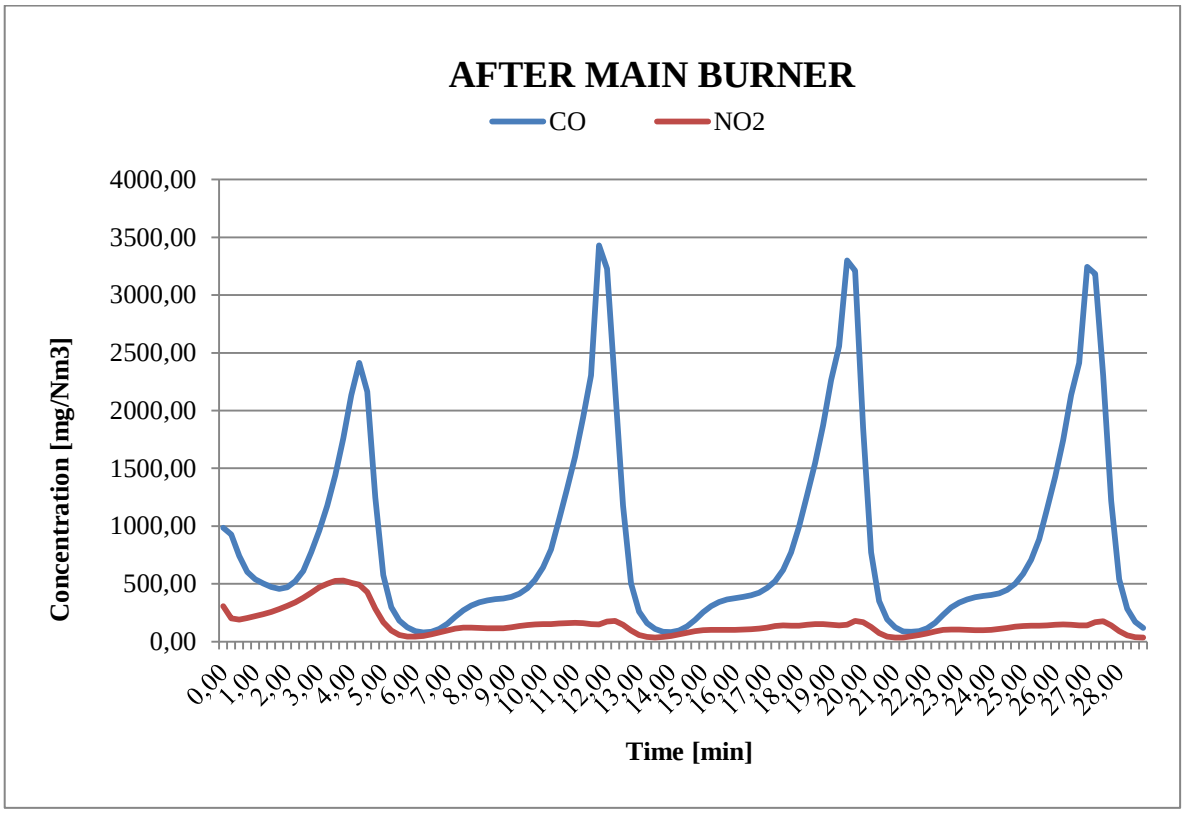

Fig.1.12: CO and NO_2 emissions after the main burner for a representative roasting cycle.

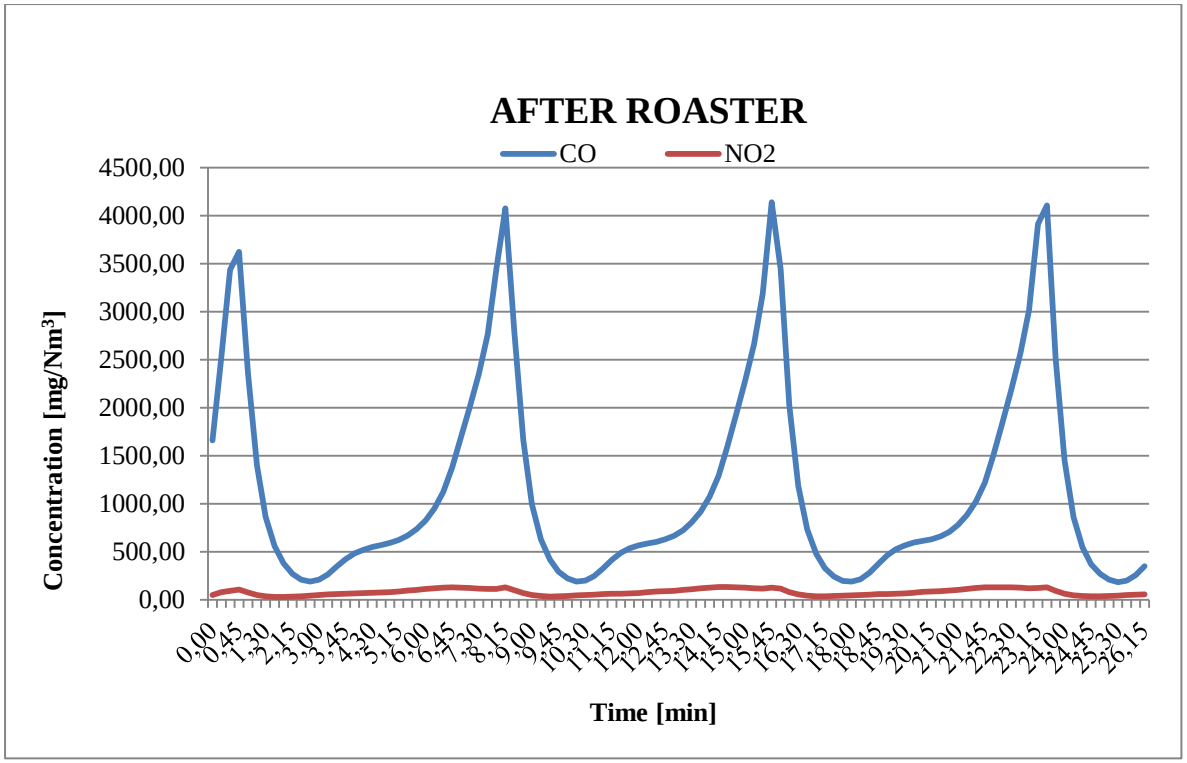

Fig.1.13: CO and NO_2 emissions after the roaster for a representative roasting cycle.

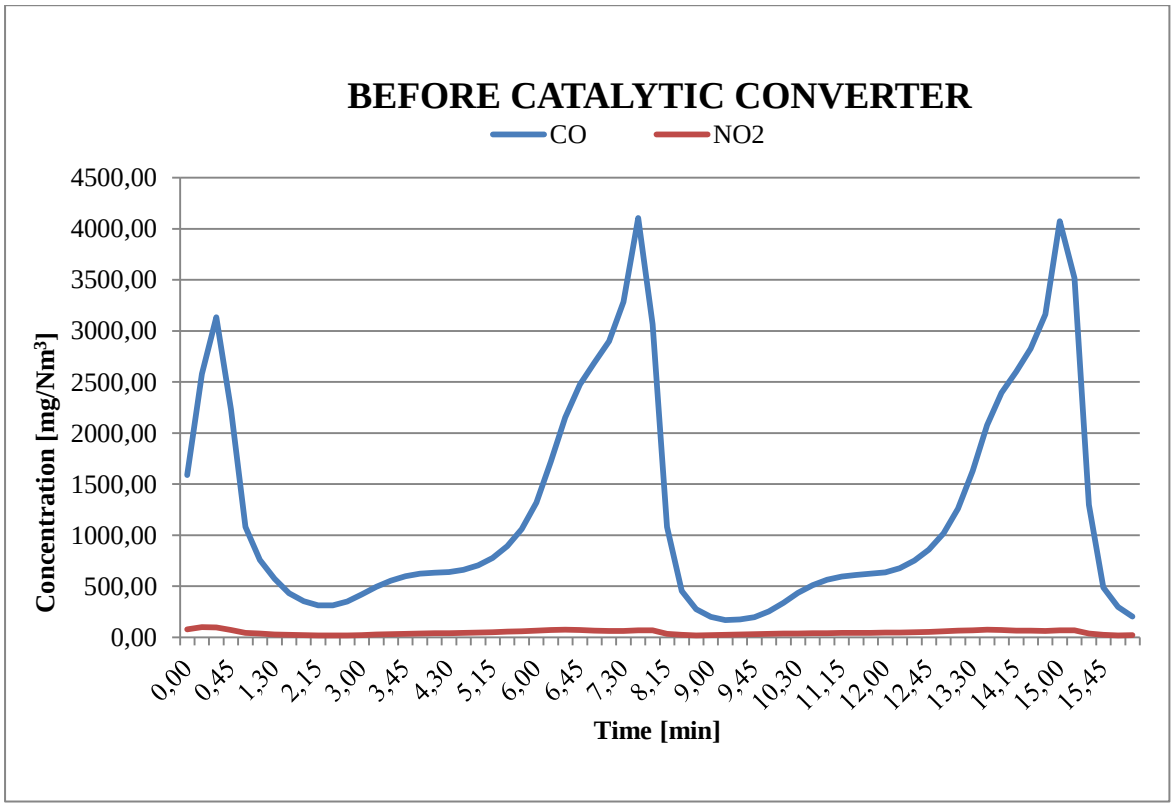

Fig.1.14: CO and NO_2 emissions before the catalytic converter for a representative roasting cycle.

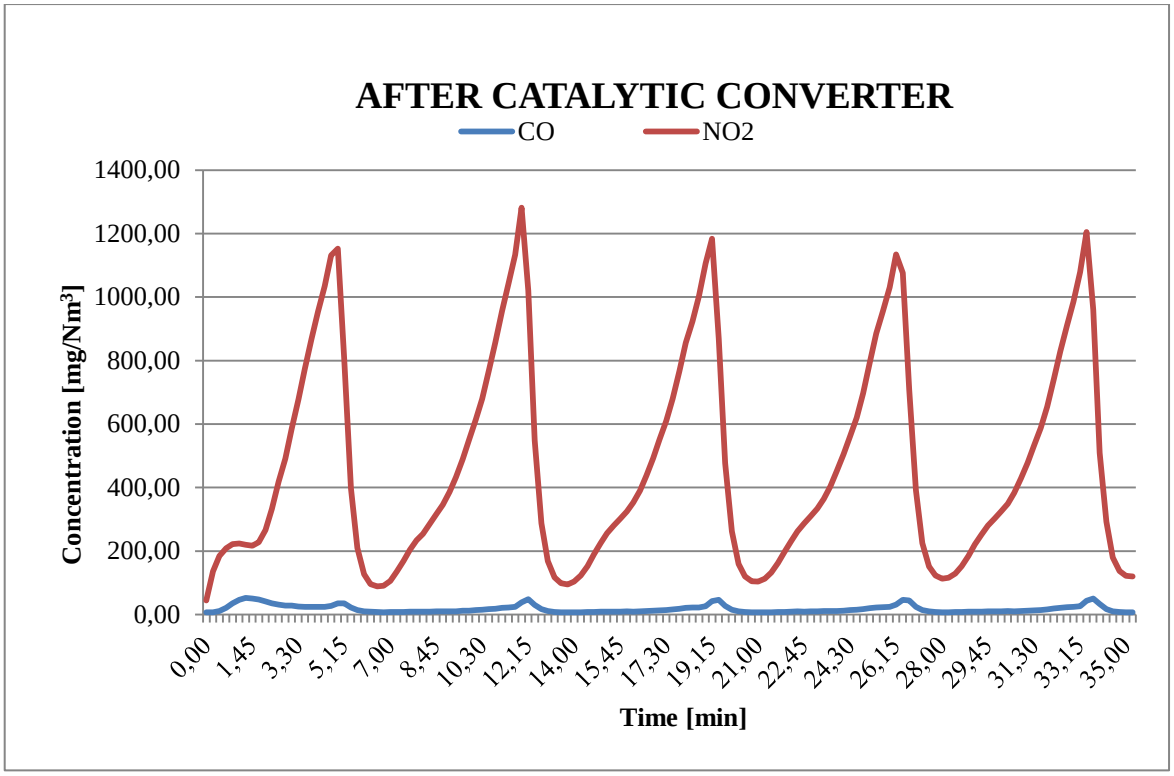

Fig.1.15: CO and NO_2 emissions after the catalytic converter for a representative roasting cycle.

So, VOC and nitrogen compounds are emitted from the roaster. The VOCs are abated through the oxidation catalyst. At this stage NO_x are formed.

1.3.2.2 Catalyst for NO_x and VOC removal

Recent studies have led to the selective catalytic oxidation of nitrogen compounds (NH_3 and pyridine) to nitrogen.

Amblard et al. have reported that among the transition metals supported on γ-Al_2O_3, Ni, Mn and Fe were the most active and selective catalysts for the SCO at high temperature.

Titanium dioxide (TiO_2) was also studied as a support, which is more active and selective towards N_2 at low temperatures (<300 °C) compared to γ-Al_2O_3.

Using zeolites exchanged with transition metals (Me-Y) as a support, it was proved that the activity for the ammonia oxidation decreased in the sequence of Cu-Y> Cr-Y> Ag-Y> Co-Y> Fe -Y> Ni-Y> Mn-Y, and the main product was nitrogen.

Recently, the SCO method was studied on a series of transition metals (Cr, Mn, Fe, Co, Ni, Cu or Pd) supported on ZSM-5. The results showed that the catalytic

performances increase in the tendency of Co-ZSM-5 ~ Ni-ZSM- 5 <Mn-ZSM-5 <H-ZSM-5 <Pd-ZSM-5 <Cr-ZSM-5 <Cu- ZSM-5 <Fe-ZSM-5 [19].

The selective catalytic oxidation of ammonia nitrogen (NH_3-SCO) has been studied on mixed oxide ceria-zirconia ($Ce_{1-x}Zr_xO_2$) [20].

In particular, the catalyst $Ce_{0.4}Zr_{0.6}O_2$ showed the best activity of oxidation of NH_3, with a temperature of complete conversion equal to 360 ºC.

The results also indicated that a zirconium content increased in the catalysts $Ce_{1-x}Zr_xO_2$ improves the selectivity to N_2 which is about 100% with x>0.4. Catalysts $Pt/CuO/Al_2O_3$ with 20% wt of CuO and 0.5-4% wt of Pt were prepared and used for the selective catalytic oxidation of ammonia in wet and dry gas and in synthetic biogas with CO, hydrogen and methane.

The measures of activity show that $Pt/CuO/Al_2O_3$ is active and selective for the oxidation of ammonia to form nitrogen [21].

The effects of catalysts of oxides modified Ce_2O_3-Cu-Mn/TiO_2 and La_2O_3-Cu-Mn/TiO_2 were considered on the basis of catalytic activity and the selectivity of the ammonia oxidation in the temperature range from 125 to 250 ºC [22].

The results revealed the beneficial role of La_2O_3 and Ce_2O_3 in catalytic activity at low temperature and lean oxygen concentration, while the change with La_2O_3 and Ce_2O_3 brought a negative influence on the selectivity to N_2. The activity of ammonia oxidation at low temperature is related to the ability of dissociative or non-dissociative adsorption of oxygen of the catalysts.

Furthermore, a good correlation is existing between the selectivity to N_2 for the selective catalytic oxidation (SCO) and selective catalytic reduction (SCR) [23].

The catalyst $Ru/Ce_{0.6}Zr_{0.4}O_2$ shows a significant catalytic activity and slippage of ammonia was almost completely removed in the presence of NO_x and SO_2.

Other catalysts active and selective in the process of selective oxidation of ammonia to nitrogen (NH_3-SCO) were found to be HY zeolites modified with palladium (0.05 to 2.5 wt.%) [24].

By varying the proportion of palladium in the zeolite, the conversion of ammonia and the selectivity to nitrogen vary and the temperature at which the maximum yield is obtained too.

In fact, for the catalyst 1.5% wt Pd/HY the peak temperature is shift from 200 ºC to 370 ºC compared with 0.05% wt Pd/HY.

1.4 NO_x PREVENTION AND ABATEMENT

There are various solutions to prevent the arising of nitrogen oxides by modifying the combustion process such as:

1. Reduction of the peak temperature of the flame, through:

– Water Injection (or Steam Injection) in such a way that this absorbs heat during combustion, vaporizing and lowering, consequently, the flame temperature.

– Flue gas recirculation: widely used both in stationary plants and especially in the automotive sector (EGR). This strategy involves the recirculation of exhaust gases into the combustion chamber, after cooling (intercooling). The mass of gas thus acts as a thermal flywheel, decreasing the flame temperature and hence NO_x products.

– Less Excess of Air (LEA): the level of EA was considered a practical limit because it gave good combustion but did not require extensive furnace monitoring. Owing to less than perfect mixing of air and fuel, there must be some EA present at all times to ensure good fuel use and to prevent smoke formation.

2. Oxyfuel: it reduces the formation of thermal NO_x by acting on the reactants, by carrying out combustion with the presence of oxygen. This solution, although very effective, is expensive because of the need to use pure oxygen.

3. Reduction of contact time: this solution can be applied using various technologies, such as the subdivision of combustion in multiple stages (staged combustion), the use of flames in lower concentration of reagents or greater dispersed in space.

The technologies involve however secondary post-treatment systems which eliminate NO_x downstream of the combustion. They are divided into:

– Adsorption and reduction in NOx (SCONOX)

– selective non-catalytic reduction (SNCR)

– Selective catalytic reduction (SCR)

1.5 LNT

One of the most promising systems for the reduction of NO_x at the exhaust of diesel engines, thus operating with a lean mixture, is the so-called "NO_x-storage catalyst", also called Lean NO_x Trap. This system can be considered for NO_x control for both heavy-duty and light-duty applications.

The system operates in a discontinuous way, contrary to the TWC (Three Way Catalyst) or DOC (Diesel Oxidation Catalyst); it is constituted by a monolithic structure coated with materials that serve both for the accumulation phase of NO_x (alkali metals and alkaline earth metals, Ba, K, Na, Mg, Ca), both for the catalysing oxidation and reduction action (noble metals, respectively Pt and Rh).

In conditions of lean mixture (normal operation of the diesel engine), the NO_x trap removes nitrogen oxides (NO and NO_2) from the exhaust gas and accumulates them in the form of nitrites and nitrates.

Before the accumulation phase, it is necessary to oxidase NO to NO_2 on the sites of platinum, which therefore acts as an oxidant catalyst , being the NO_2 easily to be accumulated in the trap compared to NO [25,26].

In the accumulation phase:

$$BaO + NO_2 + ½\, O_2 \leftrightarrow Ba(NO_3)_2 \qquad (1.8)$$

The total NO_x adsorptive capacity of NO_x trap obviously depends on the availability of free sites of BaO, which must be recovered when a certain NO_x concentration is attained at the exit of the converter.

The reduction to N_2 and the regeneration of the NO_x trap requires a reducing environment, and then a level almost nil O_2.

When the regeneration is started, the oxygen concentration decays to almost zero, and suitable conditions for the NO reduction are achieved.

The reducing agents can be several, such as CO, HC, or even hydrogen. The most common species devoted to NO reduction are hydrocarbons, which can be directly fed to the system, without further fuel reforming.

The first step of the regeneration is the decomposition of the nitrate, and the recovery of the BaO site.

In this step, NO is released, therefore the proper amount of fuel has to be dosed in order to promptly reduce the NO released.

$$Ba(NO_3)_2 \leftrightarrow BaO + 2NO + 1½\, O_2 \qquad (1.9)$$

This can be achieved by increasing the levels of EGR (Exhaust Gas Recirculation) and injecting additional fuel to the internal cylinder to bring the air/fuel ratio until the stoichiometric value (or slightly lower).

In contrast, these operations involve high levels of smoke and soot and are highly harmful for the life of the engine.

The NO_x trap operating within a temperature range quite extensive, ranging from 200 to 450 to 500 ºC.

The lower temperature limit depends on the low kinetics of oxidation of NO to NO_2 at low temperatures, while the upper one is determined from the instability of nitrates, which, even in conditions of poor mixture, may decompose at elevated temperatures.

During the periodic regeneration (which can also take place about every minute), the conversion of NO_x is improved thanks to a higher duration of rich-spike and low values of lambda, all however at the expense of emissions of HC and CO.

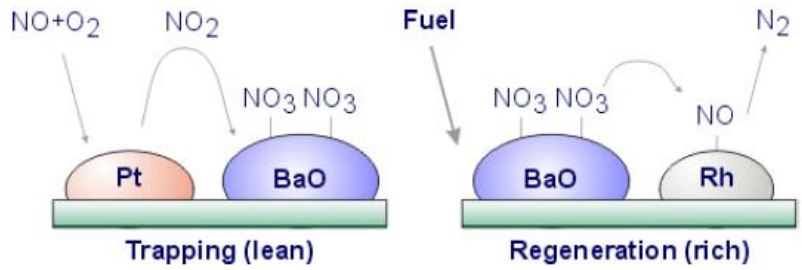

Fig. 1.16: Steps of LNT process

1.6 SCONOX

The SCONOX system is a new catalytic reduction technology that has been developed and it is currently being made available for natural gas-fired turbines.

The principle of operation of this catalytic technology is based on NO_x entrapment by means of adsorption and catalytic oxidation. The SCONOX system does not require the use of ammonia, eliminating the potential of ammonia slip conditions evident in existing SCR systems. CO and NO are catalytically oxidized to CO_2 and NO_2. The NO_2 molecules are subsequently absorbed on the treated surface of the SCONOX catalyst. One of the catalysts used for this technique is the potassium carbonate supported on alumina doped with Platinum ($Pt\text{-}K_2CO_3/Al_2O_3$). The potassium carbonate catches NO_x and HC while the Platinum promotes the reduction to N_2 during regeneration of the catalyst. The reaction scheme can then be described as follows:

Entrapment

$$NO + \frac{1}{2}O_2 \rightarrow NO_2 \quad (1.10)$$

$$2NO_2 + K_2CO_3 \rightarrow CO_2 + KNO_2 + KNO_3 \quad (1.11)$$

Regeneration

$$KNO_2 + KNO_3 + 4H_2 + CO_2 \rightarrow K_2CO_3 + 4H_2O\ (g) + N_2 \quad (1.12)$$

1.7 SNCR

SNCR technologies came into commercial use on oil- or gas-fired power plants in Japan in the middle of the 1970s. In Western Europe, SNCR systems have been used commercially on coal-fired power plants since the end of the 1980s. In the USA, SNCR systems have been used commercially on coal-fired power plants since the early 1990s.

This solution involves the injection of a reducing agent, such as ammonia, in the gases for the reduction of NO_x to N_2within an appropriate temperature window.

Emissions of NO_x can be reduced by 30% to 50%. The NO_x and reagent (ammonia or urea) react to form nitrogen and water. The process does not require the use of a catalyst, thanks to the high temperatures involved (between 900 °C and 1100 °C).

When the reaction temperature increases over 1000 °C, the NO_x removal rate decreases due to thermal decomposition of ammonia. On the other hand, the NO_x reduction rate decreases below 1000 °C and ammonia slip may increase. The effectiveness depends largely on the optimization of the injection, enabling the achievement of conversions of the order of 40-70%. Ammonia slip from SNCR systems occurs either from injection at temperatures too low for effective reaction with NO_x or from over-injection of reagent leading to uneven distribution. An injection system that has too few injection control points or injects a uniform amount of ammonia across the entire section of the boiler will almost certainly lead to a poor distribution ratio and high ammonia slip.

Distribution of the reagent can be especially difficult in larger coal-fired boilers because of the long injection distance required to cover the relatively large cross-section of the boiler.

1.8 SCR

Selective catalytic reduction (SCR) is a technology that permits to convert nitrogen oxides into diatomic nitrogen, N_2, and water, H_2O.

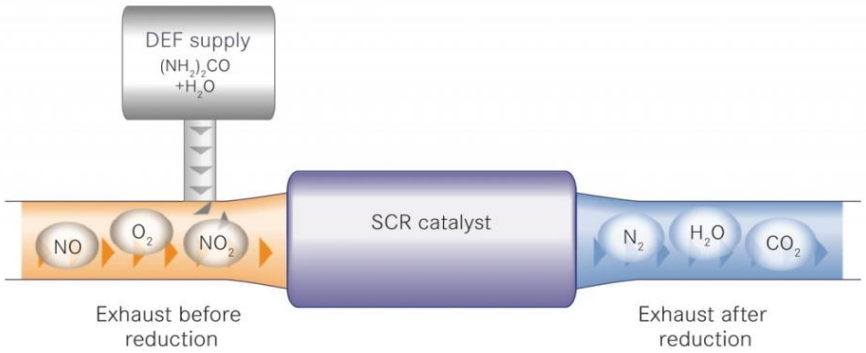

Fig.1.17: SCR scheme

This technology was initially used in the late 1970s in thermal power plants in Japan. Subsequently spread since the mid-1980s in Europe and in the 1990s in the USA where was introduced for gas turbines. The SCR applications, with a growing number of installations for NO_x control from coal-fired power plants, was extended and so include plant and refinery heaters and boilers in the chemical processing industry, furnaces, coke ovens, as well as municipal waste plants and incinerators.

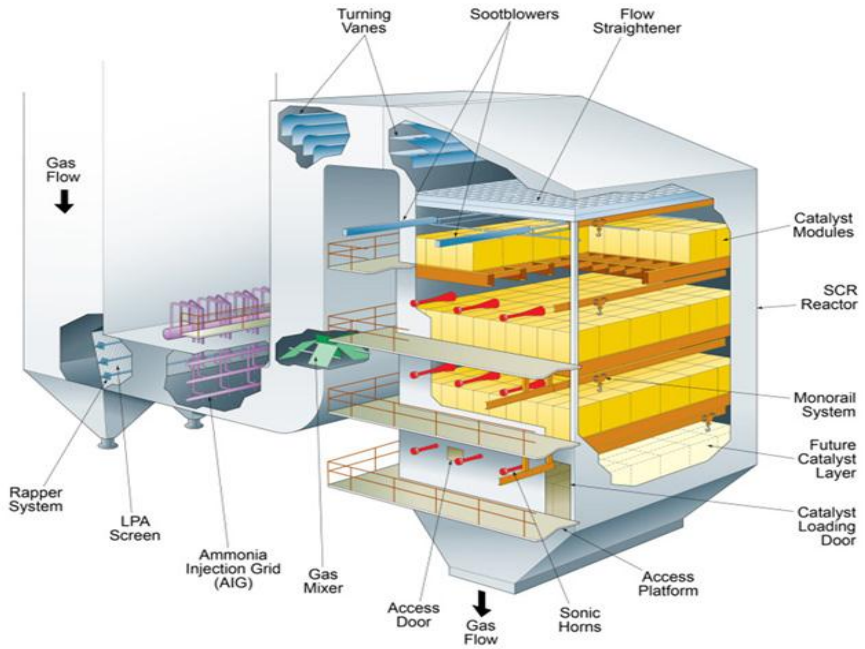

Fig.1.18: SCR scheme in power plant

Since the new legislation SCR was introduced into mobile diesel engines, at the beginning, in the USA in the context of the 2010 NO_x limit of 0.2 g/bhp-hr for heavy-duty engines, as well as the Tier 2 NO_x standards for light-duty vehicles.

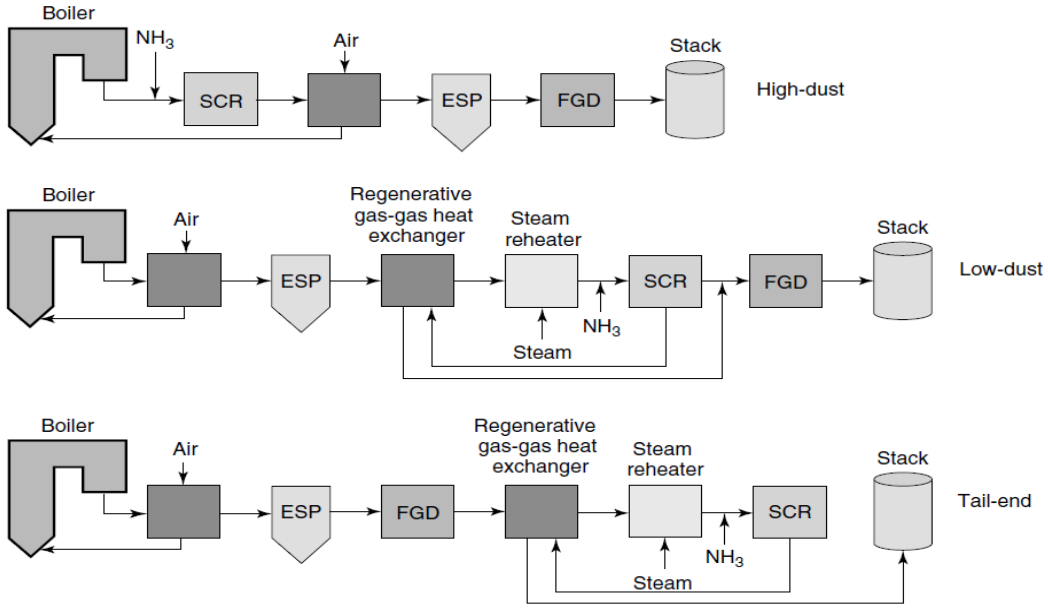

Fig. 1.19: Process layout for conventional installation of SCR reactors at boiler-based power plants.

Depending on the structure of the power plant, the location of the unit to the SCR can change. There are three possible configurations. At first, the high dust configuration. Looking at the Fig.1.19, it is possible to observe the various equipment present and their placement. The ammonia injection is inserted after the boiler and immediately before the SCR system. Subsequently it has an air preheater, an electrostatic precipitator (ESP) and a plant for flue gas desulphurisation (FGD).

In this configuration catalysts based on vanadic anhydride or titanium oxide are generally used, by operating at temperatures around 350-400 °C. The SCR is always placed before the removal of particulate matter.

Normally the reactors are composed by vertical axis and consisting of several catalytic beds, in which the decrease of the accumulation of dust is favoured in the channels of the catalyst support. In this configuration, the level of particulate can vary (from 1 to 30 g/m^3), depending on the type of fuel and the type of burner.

Due to the features of the ashes and their accumulation, there is deterioration in performance and a catalyst deactivation. This phenomenon happens from the alkali metals and sulphur compounds which they place in the pores of the catalyst. Consequently, to improve performance and to increase efficiency, it is desirable to periodically check the implant and the individual devices.

In Low Dust configuration, the catalyst is located downstream of the electrostatic precipitator. The catalyst is placed in a honeycomb structure. The working temperature is about 300-450 °C and depends on the need to control NO_x emissions and the production of sulphur trioxide from the SO_2. In this configuration, the level of particulate is significantly lower. To increase the life of the catalysts themselves, it is necessary to add promoters, such as molybdenum and tungsten, to vanadic dioxide and titanium oxide.

The tail end configuration makes sure that the SCR rig uploads the exhaust gas cleaner, since the plant for the SCR is placed after the electrostatic precipitator, ESP, and after the plant for flue gas desulphurization, FGD. In this case, the working temperatures are significantly decreased (around 300-350 °C). The average duration of the catalyst is around 5-9 years.

The table 1.7 summarizes the typical dimensional values of the monoliths used in the three different configurations described. The values of load losses related were referred to a linear speed of 5 m/s.

Table 1.7: Catalyst for SCR configuration

Catalyst type		***High-dust***	***Low-dust***	***Tail-end***
Element width	mm	150–500	150–500	150–500
Length	mm	500–1000	200–1000	200–1000
Cell density	Cells cm^{-2}	1–2	2.5–6	7–10
Pitch	mm	6–10	4–6	3–4
Wall thickness	mm	0.8–1.4	0.5–1	0.4–0.7
Geometric surface area	$m^2\ m^{-3}$	350–450	500–800	800–1000
Void fraction	–	0.65–0.75	0.63–0.75	0.66–0.78
Specific pressure drop*	hPa m^{-1}	1–2.5	3–4	5–8

The SCR industrial catalyst widely used for flue gas cleaning is based on TiO_2 supported V_2O_5–WO_3 and/or V_2O_5–MoO_3 oxides [27-30], while mobile systems use zeolite based catalysts.

The vanadium catalyst was first found to be active in the SCR reaction during the 1960s, and has since then been the predominant catalyst used.

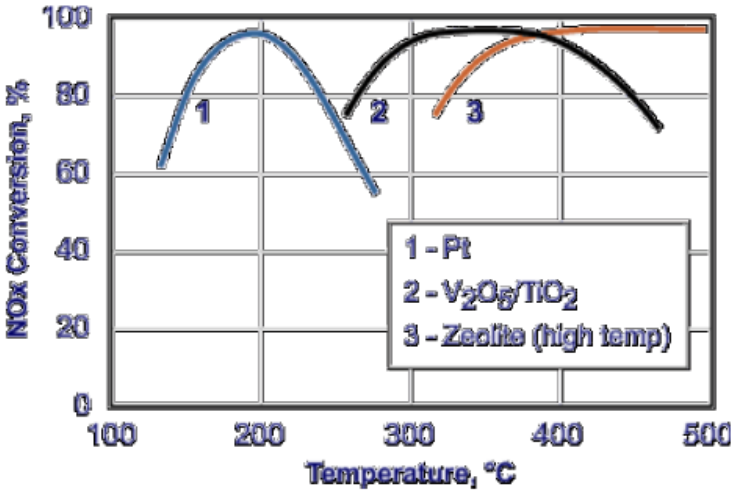

Fig. 1.20: operating temperature window of the catalyst for NH_3-SCR.

In order to prevent the oxidation of SO_2 to SO_3 due to the high level of sulphur in the gas, the vanadium content must be the minimum.

Anatase form of TiO_2 is the preferred support mainly because SO_2 poisoning does not take place on TiO_2.

The combination of V_2O_5–WO_3/TiO_2 and V_2O_5–MoO_3/TiO_2 was used in industrial SCR [31, 32]. Aggregation of vanadia in conventional SCR catalyst favours the sintering and anatase-to-rutile phase transformation of catalysts (Fig. 1.20). It should be mentioned that TiO_2-anatase is a metastable titanium dioxide polymorph and tends to convert into the thermodynamically stable rutile form at any temperature and pressure, making V_2O_5/TiO_2 (anatase) an unstable system.

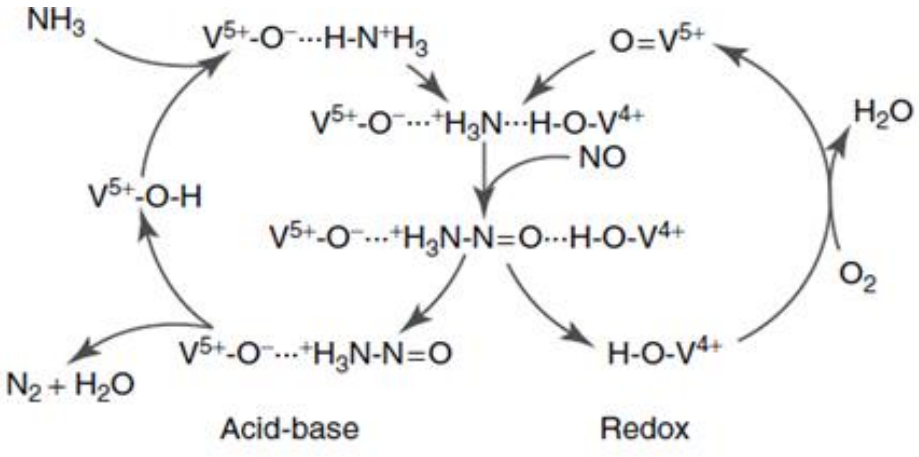

Fig.1.21: Catalytic cycle of the SCR reaction over vanadium on titanium-based catalyst

SCR reaction is a redox process that occurs with a redox or Mars–van Krevelen-type mechanism on vanadium-based catalysts.

A high-temperature application also requires a low level of vanadium to maintain the selectivity toward N_2 instead of secondary reactions that bring to N_2O or direct oxidation of NH_3 to NO, N_2O or N_2.

The main reactions in the SCR process are:

$$4NH_3 + 4NO \leftrightarrow 4N_2 + 6H_2O \quad (1.13)$$

The range of application in which the 90% of NO is converted is between 250 - 500°C.

$$2NH_3 + NO + NO_2 \leftrightarrow 2N_2 + 3H_2O \quad \text{(Fast SCR)} \quad (1.14)$$

The last reaction is called Fast SCR for the higher reactivity.

$$4NH_3 + 6NO \leftrightarrow 5N_2 + 6H_2O \text{ (Slow SCR)} \quad (1.15)$$

$$8NH_3 + 6NO_2 \leftrightarrow 7N_2 + 12H_2O \ (NO_2\ SCR) \quad (1.16)$$

The following reactions produce byproducts as (N_2O) or molecular nitrogen from the oxidation of ammonia.

$$2NH_3 + 2O_2 \leftrightarrow N_2O + 3H_2O \quad (1.17)$$

$$4NH_3 + 3O_2 \leftrightarrow 2N_2 + 6H_2O \quad (1.18)$$

$$4NH_3 + 5O_2 \leftrightarrow 4NO + 6H_2O \quad (1.19)$$

Moreover, ammonia could react with NO_2 producing ammonium nitrate (NH_4NO_3) and this occurs at low temperatures, almost at 100-200°C.

Ammonium nitrate may deposit on the catalyst and lead a temporary deactivation [33]. It is possible to reduce the formation of the NH_4NO_3 formation by supplying into the gas stream less than the precise amount of NH_3 necessary for the stoichiometric reaction with NO_x.

$$2NH_3 + 2NO_2 + H_2O \leftrightarrow NH_4NO_3 + NH_4NO_2 \quad (1.20)$$

In the case of diesel exhaust, SO_2 can be oxidized to SO_3 with the formation of H_2SO_4. Also NH_3 combines with SO_3 and form $(NH_4)_2SO_4$ and NH_4HSO_4 below 250 °C.

$$NH_3 + SO_3 + H_2O \leftrightarrow NH_4HSO_4 \quad (1.21)$$

$$2NH_3 + SO_3 + H_2O \leftrightarrow (NH_4)_2SO_4 \quad (1.22)$$

The major problem of the SCR technology is the ammonia injection: an insufficient quantity could lead low NO_x conversions and a release of ammonia to the atmosphere called *ammonia slip*.

The ammonia slip increases at higher NH_3/NO_x ratios. In practice, ratios between 0.9 and 1 are used, which minimize the ammonia slip while still providing satisfactory NO_x conversions.

Other catalysts developed for the SCR process are perovskite-type oxides with a general formula ABO_3 (where A is usually a rare-earth metal coordinated by 12 oxygen atoms and B is usually a transition metal surrounded by six oxygen atoms in octahedral coordination).

In NO_x abatement perovskites like $LaCoO_3$, $LaCo_{1-x}\ Cu_xO_{3-d}$, have a moderate use [34] as well as the partial substitution of lanthanum and manganese to form mixed oxides $La_{1-x}A_xMn_{1-y}B_yO_3$ obtaining Mn ions in various oxidation states or to create O^{2-} vacancies in the lattice, which can dissociate NO [35].

Into perovskites another catalytically active transition metal can be Cu^{2+} that lead to much higher activity for the CO + NO reaction [36].

It is also possible to incorporate noble metals as Pt [37], Rh [38], and Pd [39] into a perovskite structure stabilizing the noble metal against sintering, reaction with the support, or volatilization.

Mobile systems normally use zeolite based catalysts. Cu^{2+}-exchanged ZSM-5 zeolites are active catalysts for the reduction of nitric oxide with ammonia in the presence of oxygen.

It was shown that NO reduction by NH_3 over Cu(II) ion-exchanged Y-type zeolites [Cu(II)NaY] followed Langmuir–Hinshelwood kinetics [40]. Zeolites as catalysts or catalyst supports offer a number of potential advantages over oxide or activated carbon supports. The high internal surface area will enhance reactivity, so allowing the generation of high metal dispersions with resistance to sintering and the introduction of an acid function.

Extensive studies on SCR of NO have been carried out over other first row transition metal oxide than vanadium.

Mn oxides based catalysts are becoming popular for SCR reactions because of its low-temperature activity.

Among these various non-noble metals, MnO_x has an important role because of its lower cost, versatility, environment-friendly nature and, of course, performances.

Generally, Mn is used in both reduction and oxidation reactions due to its various types of labile oxygen as well as to the presence of different structures and morphology.

To the best of our knowledge, the optimal oxidation state of the metal has not been assessed for the SCR reaction, despite numerous studies dealing with the role of MnO_x and the deactivation of the catalysts [41, 42].

Several works investigated the activity and selectivity in low temperature NH_3-SCR of manganese oxides.

In particular, Tang et al. [43] as well as Yamashita and Vannice [44] considered four manganese oxides, proving that Mn_2O_3 and Mn_3O_4 presented stable catalytic activity and, between them, Mn_2O_3 the best one, probably due to the content of various types of labile oxygen that can complete a catalytic cycle [45].

Furthermore, Kapteljn et al. [46] investigated different oxidation states, crystallinity and specific surface area of MnO_x in the NH_3-SCR, resulting that MnO_2 exhibited, per unit surface area, the highest activity, followed by Mn_5O_8, Mn_2O_3, Mn_3O_4 and MnO. This order, and subsequently the SCR activity, was correlated to the onset of reduction in temperature programmed reduction (TPR) analyses.

From these studies, it can therefore be concluded that the SCR activity and the selectivity for nitrogen of unsupported manganese oxides is mainly affected by the Mn oxidation state, the degree of crystallinity and the specific surface area.

Over the past several years, cerium dioxide and CeO_2-containing materials become relevant as catalysts and as structural and electronic promoters of heterogeneous catalytic reactions.

Cerium dioxide is probably one of the most investigated compounds and attracted the interest in catalysis for its promoter and OSC functions.

In fact, CeO_2 is not toxic, cheap and, most important, has a unique redox property and high storage capacity making it widely investigated also in the SCR [47].

The variable Ce valence state and the Ce^{4+} vs Ce^{3+} redox couple (1.3-1.8 V) are important factor that perform, under oxidizing and reducing conditions, the shift between CeO_2 and Ce_2O_3.

On the other hand, as seen before, manganese oxides (MnO_x) have been studied as low-temperature SCR catalysts.

The additional advantage of coupling MnO_x with ceria lies in the multiple oxidation states of manganese joined with the redox couple of cerium.

A key role is played by the synthesis method of such a mixed Ce-Mn catalyst, so it is possible to find in the recent works new routes for the preparation of MnO_x-CeO_2

catalysts, such as co-precipitation [48], solution combustion synthesis SCS [49] and plasma method [50].

Solution combustion synthesis (SCS) is an effective method used for the synthesis of nanoscale materials and for the production of various ceramic powders in a wide variety of advanced applications.

The SCS method is characterized by an exothermic reaction between nitrates of the metals of the desired oxides and an organic fuel. In particular, glycine and urea are suitable fuels because they are amino acids that can act as a complexing agent of the metal ion in the solution and also serve as fuel for the synthesis of nanocrystalline metal oxides. The first step was the dissolution of both the components in water and the formed solution was put in an oven pre-heated at different temperatures. The very fast evaporation of the water and the decomposition of the reactants, give as products agglomerated nanoparticles of the desired oxide.

The operative conditions influence the properties of the resulting powders (crystalline structure, amorphous structure, crystallite size, purity, specific surface area and particle agglomeration).

With this synthesis method is possible to notice the influence of the fuel-oxidant ratios well as a model of the thermodynamic variables associated with enthalpy, adiabatic flame temperature and the total number of moles of gas generated are related to the powder characteristics, such as crystallite size and surface area.

More recently, MnO_x-CeO_2 catalysts have been reported not only to achieve high activity in the selective catalytic reduction (SCR) of NO_x with NH_3 but also proved to exhibit promising resistance to SO_2 poisoning [51, 52], that is a several obstacle to the development of any NH_3-SCR technology due to the catalyst deactivation for the presence of SO_2 [53].

In the present work, the solution combustion route was chosen for synthesizing MnO_x-CeO_2 catalysts. The Mn/Ce molar ratio as well as quality and quantity of organic fuel in the reaction were investigated as key parameters and their influence on the structural, microstructural and superficial properties was studied.

Moreover, the redox property of MnO_x-CeO_2 samples and the synergistic effect of Ce^{4+} and Mn^{n+} ions were analysed.

All these properties were correlated to the catalytic activity in order to optimize the parameters for the best catalytic performance.

1.9 BIBLIOGRAPHY

[1] H. Bosch, F. Janssen, Formation and control of nitrogen oxides, Catal. Today 2 (1988) 369–379.

[2] Nitrogen Oxides: Impacts on Public Health and the Environment, EPA 452/R-97-002

[3] K. J. Whitty, H. R.Zhang, E. G. Eddings, Emissions from syngas combustion, Combust. Sci. and Tech., Vol. 180, p. 1117 – 1136, 2008

[4] S. R. Turns, An introduction to combustion: concepts and applications, 2nd edition, McGraw Hill, p. 559 – 567, 2000

[5] A. L. Boehman, D. Morris, J. Szybist, The impact of the bulk modulus of diesel fuels on fuel injection timing, Energy & Fuels, Vol. 18, p. 1877 – 1882, 2004

[6] G. H. Abd-Alla, Using Exhaust Gas Recirculation in Internal Combustion Engines: A Review, Energy Conversion and Management, Vol. 43, p. 1027 – 1042, 2002

[7] Y. Traa, B. Burger, J. Weitkamp, Zeolite-based materials for the selective catalytic reduction of NOx with hydrocarbons, Microporous and Mesoporous Materials, Vol. 30, p. 3 –41, 1999

[8] G. Ertl, H. Knözinger and J.Weitkamp, Handbook of Heterogeneous Catalysis, Vol. 5 (1997), 2412, VCM-Wiley

[9] M. V. Twigg, "Progress and future challenges in controlling automotive exhaust gas emissions", Applied Catalysis B: Environmental 70 (2007), 2-15.

[10] E.R. Dutra, L.S. Oliveira, A.S. Franca, V.P. Ferraz, R.J.C.F. Afonso, " A preliminary study on the feasibility of using the composition of coffee roasting exhaust gas for the determination of the degree of roast", Journal of Food Engineering 47 (2001) 241±246

[11] C. Yeretzian, A. Jordan, R. Badoud, W. Lindinger " From the green bean to the cup of coffee: investigating coffee roasting by on-line monitoring of volatiles" Eur Food Res Technol (2002) 214:92–104

[12] C. A. B. De Maria, L. C. Trugo, F. R. Aquino Neto, R. F. A. Moreira" & C. S. Alviano, " Composition of green coffee water-soluble fractions and identification of volatiles formed during roasting ", Food Chemistry, Vol. 55, No. 3, pp. 203-207, 1996

[13] R. A. Buffo, and C. Cardelli-Freire "Coffee flavour: an overview", Flavour Fragr. J. 2004; 19: 99–104

[14] I. LOÄ Pez-Galilea, N. Fournier, C.Cid,. and E. Guichard, "Changes in Headspace Volatile Concentrations of Coffee Brews Caused by the Roasting Process and the Brewing Procedure"

[15] C. Sanz, D. Ansorena, J. Bello, and C. Cid, "Optimizing Headspace Temperature and Time Sampling for Identification of Volatile Compounds in Ground Roasted Arabica Coffee", J. Agric. Food Chem. 2001, 49, 1364-1369

[16] S. Schenker, C. Heinemann, M. Huber, R. Pompizzi, R. Perren, AND F. Escher "Impact of Roasting Conditions on the Formation of Aroma Compounds in Coffee Beans" JOURNAL OF FOOD SCIENCE—Vol. 67, Nr. 1, 2002

[17] P. E. Koehler, M. E. Mason and G. v. Odell, "Odor threshold levels of pyrazine compounds and assessment of their role in the flavour of roasted foods", journal of food science-Volume 36 (1971)

[18] C. Sanz, L. Maeztu, M. J. Zapelena, J.Bello,C.Cid, "Profiles of volatile compounds and sensory analysis of three blends of coffee: influence of different proportions of Arabica and Robusta and influence of roasting coffee with sugar". Journal of the Science of food and Agriculture 82:840-847, 2002

[19] G. Qi, R.T. Yang, "Selective catalytic oxidation (SCO) of ammonia to nitrogen over Fe/ZSM-5 catalysts", Applied Catalysis A: General 287 (2005) 25–33

[20] Z. Wang, Z. Qu, X. Quan, H. Wang, "Selective catalytic oxidation of ammonia to nitrogen over ceria–zirconia mixed oxides", Applied Catalysis A: General 411–412 (2012) 131– 138

[21] G. Olofsson, L. R. Wallenberg, A. Andersson ,"Selective catalytic oxidation of ammonia to nitrogen at low temperature on $Pt/CuO/Al_2O_3$", Journal of Catalysis 230 (2005) 1–13

[22] S. S. Chaugule, A. Yezerets, N. W. Currier, F. H. Ribeiro, W. N.s Delgass"'Fast NO_x storage on $Pt/BaO/\gamma\text{-}Al_2O_3$ Lean NO_x Traps with NO_2+O_2 and $NO+O_2$:Effects of Pt, Ba loading", Catalysis Today 151 (2010) 291–303

[23] D. Kaijiao, T. Xiaolong, Y. Honnghong, N. Ping,W. Lida, "Rare earth oxide modified Cu-Mn compounds supported on TiO_2 catalysts for low temperature selective catalytic oxidation of ammonia and in lean oxygen", JOURNAL OF RARE EARTHS, Vol. 28, Spec. Issue, Dec. 2010, p. 338

[24] M. Jabłon´ ska, A. Krol, E. Kukulska-Zajac, K. Tarach, L. Chmielarz, K. Gora-Marek "Zeolite Y modified with palladium as effective catalyst for selective catalytic oxidation of ammonia to nitrogen", Journal of Catalysis 316 (2014) 36–46

[25] D.H. Kima, K. Mudiyanselagea, J. Szányia, H. Zhua, J.H. Kwaka, Charles H.F. Pedena, "Characteristics of Pt–K/MgAl2O4 lean NOx trap catalysts", Catalysis Today 184 (2012) 2– 7

[26] S. S. Chaugule, A. Yezerets, N. W. Currier, F. H. Ribeiro, W. N.s Delgass"'Fast NOx storage on Pt/BaO/γ-Al2O3 Lean NOx Traps with NO2+O2 and NO+O_2:Effects of Pt, Ba loading", Catalysis Today 151 (2010) 291–303

[27] SC. Wood, Select the right NO_x control technology – consider the degree of emission reduction needed the type of fuel, combustion device design, and operational factors. Chem Eng Prog 1994;90:32–8.

[28] H. Bosch, FJ. Janssen, Preface. Catal Today 1998;2:5–8.

[29] SM. Cho, Properly apply selective catalytic reduction for NOx removal. Chem Eng Prog 1994;90:39–44.

[30] P. Forzatti, L. Lietti, Recent advances in de-NOxing catalysis for stationary applications. Heterogen Chem Rev 1996;3:33–51.

[31] M. Inomata, K. Mori, A. Miyamoto, T. Ui, Y. Murakami, Structures of supported vanadium oxide catalysts. 1. Vanadium(V) oxide/titanium dioxide (anatase), vanadium(V) oxide/titanium dioxide (rutile), and vanadium(V) oxide/ titanium dioxide (mixture of anatase with rutile). J Phys Chem 1983;87:754–61.

[32] NY. Topsoe, Characterization of the nature of surface sites on vanadia–titania catalysts by FTIR. J Catal 1991;128:499–511.

[33] S. Roy , M.S. Hegde , G. Madras Catalysis for NO_x abatement Applied Energy 86 (2009) 2283–2297

[34] H. Tanaka, I. Tan, M. Uenishi, M. Kimura, K. Dohmae, In: Kruse N, Frennet A, Bastin JM, editors. Top catal, vols. 16/17. New York: Kluwer Academic Publishers; 2001. p. 63–70.

[35] RJH. Voorhoeve, JP. Remeika, LE. Trimble ,Perovskites containing ruthenium as catalysts for nitric oxide reduction mater. Res Bull 1974;9:1393–8.

[36] N. Mizuno, Y. Fujiwara, M. Misono, Pronounced synergetic effect in the catalytic properties of LaMn1_xCuxO3. J Chem Soc, Chem Commun 1989:316–8.

[37] CN. Costa, VN. Stathopoulos, VC. Belessi, AM. Efstathiou, An Investigation of the NO/H_2/O_2 (lean-deNOx) reaction on a highly active and selective Pt/ La0. 5Ce0.5MnO3 catalyst. J Catal 2001;197:350–4.

[38] N. Guilhaume, M. Primet, Three-way catalytic activity and oxygen storage capacity of perovskite LaMn0.976Rh0.024O3+d. J Catal 1997;165:197–204.

[39] I. Twagirashema, SM. Frere, L. Gengembre, C. Dujardin, P. Granger, Structural regeneration of $LaCoO_3$ perovskite-based catalyst during the NO + H_2 + O_2 reactions. Top Catal 2002;42–43:171–6.

[40] BJ. Adelmana, WMH. Sachtler, The effect of zeolitic protons on NO_x reduction over Pd/ZSM-5 catalysts. Appl Catal B: Environ 1997;14:1–11.

[41] W.S. Kijlstra, D.S. Brands, H.I. Smit, E.K. Poels, A. Bliek, Mechanism of the Selective Catalytic Reduction of NO with NH_3 over MnO_x/Al_2O_3, J. Catal. 171 (1997) 219-230

[42] F. Kapteijn, L. Songoredjo, M. Van Driel, A. Andreini, J.A. Moulijn, G. Ramis, G. Busca, Alumina-Supported Manganese Oxide Catalysts: II. Surface Characterization and Adsorption of Ammonia and Nitric Oxide, J. Catal. 150 (1994) 105

[43] X. Tang , J. Li, L. Sun, J. Hai, Origination of N_2O from NO reduction by NH_3 over -MnO_2 and -Mn_2O_3, Appl. Catal. B: Environ. 99 (2010) 156-162

[44] T. Yamashita, A. Vannice, Temperature-programmed desorption of NO adsorbed on Mn_2O_3 and Mn_3O_4,Appl. Catal.B: Environ. 13 (1997) 141-155

[45] M. Kang, E.D. Park, J.M. Kim, J. E. Yie, Manganese oxide catalysts for NO_x reduction with NH_3 at low temperatures, Appl. Catal. A: Gen. 327 (2007) 261-269

[46] F. Kapteljn, L. Singoredjo, A. Andreini, J.A. MouhJn, Activity and selectivity of pure manganese oxides in the selective catalytic reduction of nitric oxide with ammonia, Appl. Catal. B: Environ., 3 (1994) 173-169

[47] H. Li, G. Lu, Q. Dai, Y. Wang, Y. Guo, Y. Guo, Ap. Cat. B: Environmental 102 (2011) 475-483.

[48] X.F. Tang, Y.G. Li, X.M. Huang, Y.D. Xu, H.Q. Zhu, J.G. Wang, W.J. Shen, Appl. Catal., B: Environ. 62 (2006) 265–273.

[49] B. Murugan, A.V. Ramaswamy, D. Srinivas, C.S. Gopinath, V. Ramaswamy, Chem. Mater. 17 (2005) 3983–3993.

[50] L.M. Shi, W. Chu, F.F. Qu, S.H. Luo, Catal. Lett. 113 (2007) 59–64.

[51] P. Maitarad, D. Zhang, R. Gao, L. Shi, H. Li, L. Huang, T. Rungrotmongkol, J. Zhang , J. Phys. Chem. C 117 (2013) 9999-10006.
[52] H. Chang, J. Li , X. Chen, L. Ma, S. Yang, J. W. Schwank , J. Hao, Catal. Commun. 27 (2012) 54–57.
[53] J.P. Dunn, P.R. Koppula, H.G. Stenger, I.E. Wachs, Appl. Catal. B:Environ. 19 (1998) 103.

Chapter II: Experimental methods

2.1 TECHNOLOGIES FOR THE CHARACTERIZATION AND TESTING

All the catalyst reported in my PhD thesis, were synthesized, characterized and tested.

Each of the prepared samples presented different physical-chemical and morphological characteristics, due both to the different methods of preparation.

To understand the different mechanisms for the NO_x abatement of different samples was necessary, therefore, to perform various analyses.

2.1.1 Physico-chemical characterization

Many of the characterizations carried out exploiting phenomena of chemical adsorption and/or physical.

The surface area, pore distribution (through physical adsorption), dispersion of the active ingredient and grain size (by chemical adsorption) are obtained from these particular types of evidence [1]. The two phenomena show very different features, which are illustrated in Table 2.1:

Table 2.1: characteristics of physical adsorption and chemical

Physical adsorption	Chemical adsorption
Van der Waals forces	Formation of chemical bonds
Takes place at low temperatures	is usually achieved at elevated temperatures
Low heats of adsorption	Heats of adsorption comparable to those of chemical reactions
Generally always exothermic	exothermic
Generally not active	Active
Training more layer	formation of a single layer
reversible	It may be reversible or not reversible
Not specific	Specific

The molecule interacts first for physisorption (electrostatic interaction) by approaching the surface of the solid.

The subsequent chemisorption involves passing activation energy.

The adsorption process then sees two species:

– Adsorbate: component adsorbed on the solid surface

– Adsorbent: solid in which the molecules are adsorbed

The molecules of gas, subjected to certain partial pressures, are forced to come into contact first with the surface of the adsorbent and subsequently penetrate the interior of the porosity of the solid.

This phenomenon is described by the Langmuir law, equation 2.1, which correlates the volume of gas deposited with the partial pressure applied; the greater the pressure, the greater the volume deposited. It is based on three fundamental assumptions:

– The adsorbent surface is homogeneous (the adsorption energy of all sites is identical)

– The adsorption takes place on a single layer (not allowed multilayer)

– No interaction between molecules adsorbed

$$\theta = \frac{Kp}{1+Kp} \qquad (2.1)$$

Where:

θ = degree of overlapping (0 catalyst is not coated, 1 total coating of the surface);

$K = K_{ads}/K_{des}$

p = partial pressure

The equation, in particular, describes the formation of a monolayer of adsorbate on the surface of the adsorbent, characterized by microporosity, and provides a trend right of the isotherm Langmuir type I.

Depending on the interaction which arises between adsorbent and adsorbate, and the size of the pores, it is possible to obtain, in fact, five different curves (actually 6 but the sixth is often neglected as very unusual), as shown in Figure 2.1, where V_a is the volume of gas adsorbed and P/P_0 is the relative pressure of equilibrium (P is the applied pressure and P_0 is the saturation pressure of a pure adsorbent to the measurement temperature).

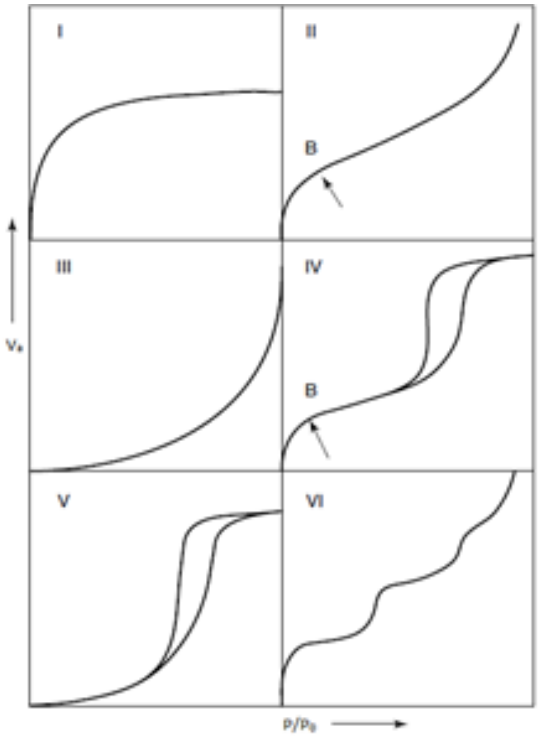

Fig. 2.1: Langmuir isotherm

2.1.1.1 BET

Another model for the description of the process of adsorption has been proposed by Brunauer-Emmett-Teller (BET).

By modifying the equation of Langmuir they have come to determine the following relation [1]:

$$V = V_m \frac{C\left(\frac{p}{p_0}\right)}{\left[1-\left(\frac{p}{p_0}\right)\right]\left[1+(C+1)\left(\frac{p}{p_0}\right)\right]} \qquad (2.2)$$

where:

V = amount adsorbed

V_m = amount adsorbed in a monolayer

p = pressure applied

p_0 = vapour pressure

C = constant related to the heat of adsorption

This model considers the possibility of adsorption in multiple layers (not more than one), and allows to determine the number of molecules adsorbed in a monolayer for compounds with isotherms of type I, II and IV. It takes three assumptions:

– the physical adsorption endless molecules in the layer

– there is no interaction between different layers

– the theory of Langmuir can be applied to each layer

Using the BET isotherm analysis, the volume of adsorbed molecules required to form a single monolayer can be found and it can be subsequently used to determine the surface area of the sample.

The size of the pores and their distribution is instead determined by the Kelvin equation (relative to cylindrical pores):

$$ln\frac{p^0}{p} = \frac{2\gamma V}{rRT} \quad (2.3)$$

To perform the test, it is necessary to first perform a thermal pretreatment of the sample (usually, the sample is placed at 200 °C for 2 hours) with the aim to remove all possible pollutants (Figure 2.2). Then the procedure continues by immersing the sample in liquid nitrogen (77K), thus fulfilling the adsorption.

Given the small size of the particles of N_2 (16, 2 $Å^2$) this type of test also allows to analyse the micro-pores, operating in a range that goes from 0.2 nm to 50 nm.

Only open pores can be analysed. The surface area and pore distribution are calculated through the analyser Micrometrics Tristar 3020 (Figure 2.3).

Fig. 2.2: Pretreatment equipment for removing pollutants

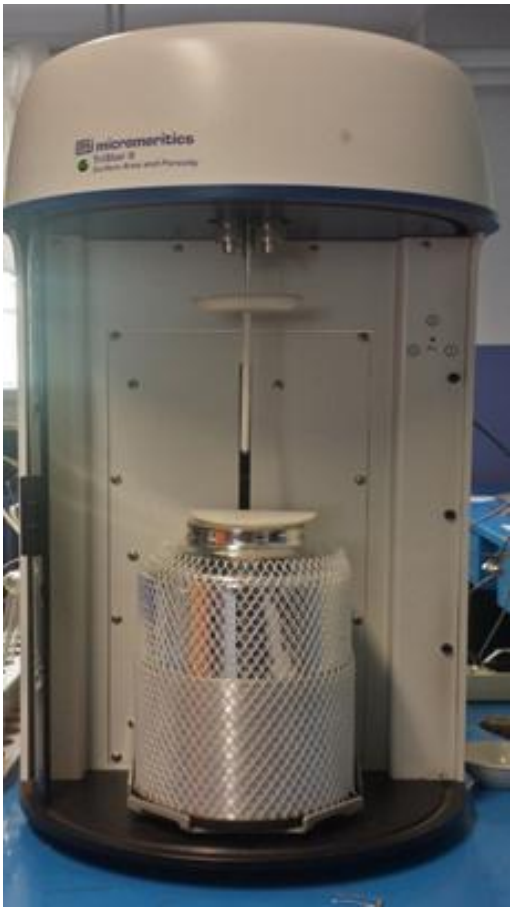

Fig. 2.3: Micrometrics Tristar 3020

2.1.1.2 TPD/R/O

The Temperature-Programmed Techniques are important methods for the study of the interactions between a solid, particularly its surface, and a certain environment for the characterization of the surface reactivity in reduction, oxidation, desorption and decomposition processes.

The temperatures at which the different species react on the surface give information on their bond strength [2]. There are different types of techniques can be used:

– TPD (T-P Desorption)
– TPR (T-P Reduction)
– TPO (T-P Oxidation)

The first phase involves the insertion of the sample to be analysed in a quartz reactor, in turn brought inside a kiln.

Before performing the test, it is necessary to carry out a pre-treatment by blowing an inert gas in order to remove all pollutants that may be present.

The temperature is therefore increased (with a ramp of 5 °C/min in the tests performed), always under flow of inert, and it is observed, at the reactor outlet, the desorption of the various species contained in the sample under analysis.

If the ability of desorption of ammonia from the various samples tested is examined, 30 mg of the sample are used, pre-treated with a stream of nitrogen (35 mL/min) for 30 min.

The adsorption phase is carried out first through a flow of helium for 30 min and subsequently with a mixture of 2% NH_3/He for 30 min. Then the analysis is performed always under a flow of He (25 mL/min) and a heating ramp of 5 °C/min, from room temperature up to 600 °C.

Through the TPR the ability of the catalyst to oxidize a reducing agent is analysed. Therefore, a mixture of H_2 and inert (typically N_2) is insufflated inside the reactor (always subject to thermal ramp) and the outlet gas is measured. The different peaks obtained will reflect the different steps of reduction made by the sample.

In this case, unlike the TPD, 50 mg of sample is used under a flow of 20 mL/min of a mixture containing H_2/Ar at 5% and a temperature ramp of 10 °C/min.

A sample of CuO is used as a reference standard to determine the consumption of hydrogen and a calibration factor equal 7,87E^{-8}. Instead of TPR, TPO highlights the reducing properties of the solid investigated.

The flow is composed of O_2 and a carrier, and the peaks that are obtained highlight the different steps of oxidation of the sample.

These tests are all carried out with the instrument TPD/R/O ThermoQuest (Figure 2.4), characterized by a TCD (Thermal Conductivity Detector), which analyses the output gas by means of a voltage variation in a Wheatstone bridge. This is generally composed of 4 resistors whose resistance varies depending on temperature.

In a branch the mixture is made to pass in input to the reactor and in another one at the output.

When the composition between input and output is different the bridge becomes unbalanced and provides a signal. It is not, however, able to provide the composition of the gases that have caused the conductivity variation.

The choice of the carrier must be carried out very carefully, so that it presents conductivity different from the gas that is interested in analysing, not to cause interference during the reading of TCD.

It should also be remembered that H_2 and He are the two gases with higher conductivity (that of all the others is much lower and approximately equal), should not, therefore, be coupled.

NH_3-TPD (Temperature Programmed Desorption) analysis was carried out in a quartz bed-fixed reactor connected to a NO/NO_2 UV Limas spectrophotometre and to a N_2O/NH_3 ND-IR (Non-Dispersive Infra Red) Uras gas analyser due to the low adsorption and temperatures and the because of the time of response is very quick.

In each experiment, 200 mg sample was pre-treated under He flow (600 mL min^{-1}) for 30 min.

A mixture of 1000 ppm NH_3 in He (600 mL min^{-1}) was then fed into the reactor at room temperature (r.t.) for the adsorption run, which lasted until the NH_3 concentration value reached the initial one.

The desorption run was performed under He flow (400 mL min^{-1}) firstly at r.t., and subsequently by increasing the temperature up to 600 °C (temperature ramp = 5 °C min^{-1}) [3].

Fig. 2.4: TPD/R/O ThermoQuest

2.1.2 Spectroscopy and Microscopy

Through these characterizations, the sample is bombarded with photons, electrons, and ions providing countless information about the surface of the solid and its composition.

2.1.2.1 X-Ray Diffraction (XRD)

The X-ray diffraction is used to identify the crystalline phase and the size of the crystallites. It is based on the interaction that a monochromatic X-ray beam has with the surface of the material analysed; this interaction is expressed by Bragg's law (equation 2.4) [4].

$$n\lambda = 2d\,sin\Theta \qquad (2.4)$$

Where:

n = 1, 2,

λ = wavelength

d = distance between the different atomic planes of the crystalline phase

Θ = angle of diffraction

The X-ray source generally has wavelengths that are intrinsic, and depend on the anticathode of the source, among which the most common is copper.

A metallic filament is heated and, when excited, emits electrons that collide with the copper anticathode, exciting in turn. The electrons then follow an energy gap. The relaxation of these causes the emission of X-rays.

These radiations have different wavelengths depending on the energy gap of the electron accomplished. Not having continuous emission is necessary to use a mono-chromator to select the radiation to be used (generally the most intense).

The diffracted X-rays are collected by an analyser (phototube), which transforms the source into an electrical signal that is repeatedly multiplied.

The result is a graph that shows the intensity of the collected radiation as a function of the diffraction angle.

The crystal structure of an unknown sample can be identified by comparing the results with the XRD patterns of known samples (the International Centre for Diffraction Data, ICDD, it has a database of approximately 100,000 samples). The width of the peaks obtained is correlated to the crystallite size using the relation:

$$D = (K\,\lambda) / (b\,cos\Theta) \qquad (2.5)$$

where:

D = Diameter of crystallite

K = constant, generally equal to 1

λ = wavelength of the radiation

b = width of the peak

The greater the width of the peaks, the smaller will be the crystallites. This type of test may then be carried out under a thermal control, by making a XRD hot chamber. The sample is exposed to a gaseous flow continuous and at a heating ramp, thus ensuring the observation of all the crystallographic changes, to which is subject the sample, at different temperatures.

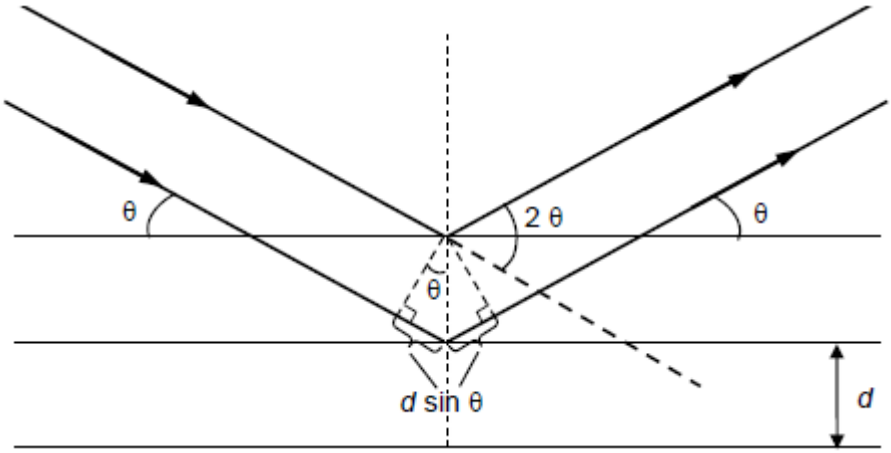

Fig. 2.5: Diagram representing the x-ray diffraction

The tests were performed using a Panalytical X'Pert Pro diffractometer (Cu Kα radiation, 2θ range 10-70, step 0.01, time per step 240 s). JCPDS files were used to identify the present phases.

2.1.2.2 X-Ray Photoelectron Spectroscopy (XPS)

This tool provides a lot of information on the surface of the material analysed (composition, oxidation state, interaction between neighboring atoms).

This information comes from a reduced number of layers (between 5 and 10), the most interesting ones from the point of view of catalysis, and from the study of the binding energy.

A beam of monochromatic X-rays is made to collide with the material, and so excite it.

The electrons that are consequently emitted are collected and analysed.

The difference between the energy of the incident beam (hv) and the kinetic energy of the electron ejected (E_k), provides the energy with which the aforementioned electron was bound (E_b).

$$E_b = h\nu - E_k \tag{2.6}$$

The weight, atomic number, oxidation state and structure of the bond, influence the binding energy.

The analysis tool is also equipped with a gun that allows bombarding argon atoms to dig the solid and reach the innermost layer.

In the present work the spectrometer X-ray photoelectron spectroscopy (XPS) analysis was carried out on a XPS PHI 5000 Versa probe apparatus, using band-pass energy of 187.85 eV, a 45° take off angle and a 100.0 μm diameter X-ray spot size.

High-resolution XPS spectra were recorded in the following conditions: pass energy of 20 eV, resolution of 1.1 eV, and step of 0.2 eV.

Sample charging effects were eliminated by referring to the spectral line shift to the C 1s binding energy (BE) value of 284.6 eV. XP-spectra were analysed by means of commercial software, applying mixed Gaussian-Lorentzian (70-30 %) profiles.

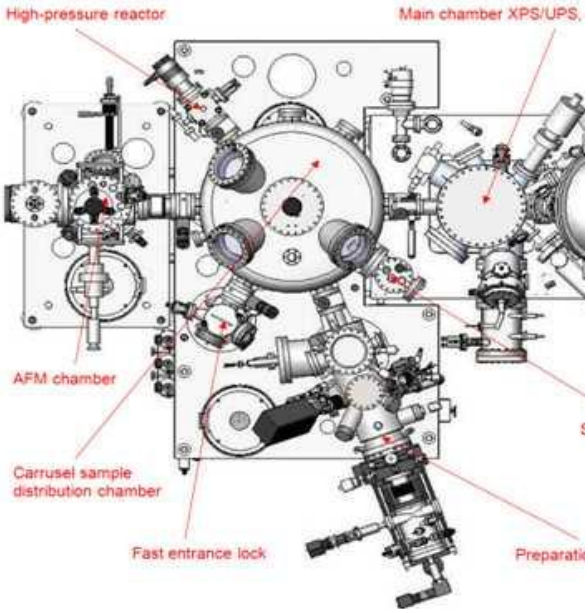

Fig. 2.6: XPS Instrument (right)

XPS parts (left)

2.1.2.3 Scanning Electron Microscope (SEM) & Filed Emission SEM (FESEM)

The scanning electron microscope is very useful if a topographic analysis of the surface is desired, especially if high resolution is not required.

Its peculiarity is to use as the source electrons (with a wavelength equal to 10-30 nm), thus differing from the normal optical microscope that, instead, uses light (400-700 nm).

This substantial difference allows the achievement of better resolutions and magnifications that depend on energy with which the electrons are accelerated, in this case about 10 KeV.

The resolution can be increased by passing to the FE-SEM (Filed Emission SEM), in which simply the source is different [5].

The images are produced using an electron beam (primary) scanned on the sample surface. The primary electrons, interacting with the surface, generate a lot of secondary electrons, at lower energy.

The intensity of these electrons is governed by the surface topography of the sample.

An image of the surface can, therefore, be reconstructed by measuring the intensity of the secondary electrons as a function of the position of the primary beam in its scanning motion. A spatial resolution with smaller than 10 nm can be obtained by decreasing the intensity of the primary beam (<1 keV).

In addition to the secondary electrons, also backscattered electrons (bounce-) and X electrons are generated. The intensity of the backscattered rays is related to the atomic number of the elements present in the sample volume that has interacted with the primary electrons.

This may provide qualitative indications of elemental composition.

The FESEM analysis is realized through the microscope Zeiss Merlin (equipped with the GEMINI II column and the detector EDS).

Fig. 2.7: FESEM apparatus

2.1.2.4 Infrared Spectroscopy (IR)

Infrared spectroscopy is one of the most used techniques for the surface chemistry analysis of a heterogeneous catalyst. It provides information on the structure and molecules adsorbed on the surface.

The technique is based on the interaction that an ultraviolet radiation has with matter: if the vibrational frequency of the molecules bound is equal to the frequency of the radiation sent, then such radiation is adsorbed.

Symmetrical molecules (for example those mononuclear) do not have any change in the dipole moment and therefore does not have absorption.

2.2 TESTING

In this chapter are described the experimental rigs illustrated in Figures 2.10, 2.11, 2.12.

The experiments were performed at Politecnico di Torino for both SCR and roasting test over powders and lab-scale filters.

In the two different experimental sets (Low Temperature NH_3-SCR and oxidative converter for roasters emissions), it is possible to determine three sections: feed section, reaction section and analysis section.

The measurements of the SCR activity were performed by placing 200 mg of the catalyst in a fixed-bed quartz reactor of 6 mm i.d., containing glass wool or a G2 porous separator, under synthetic reacting gas.

The reactor tube is located in a cylindrical electrical oven, where temperature is controlled by a PID controller. In the tests the temperatures were measured by K-type thermocouple as shown in Fig. 2.9.

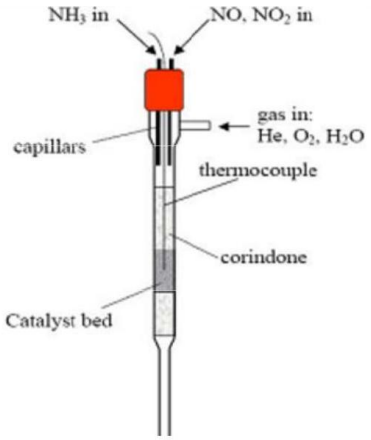

Fig. 2.8 : Configuration of the reactor

Fig.2.9 – K -type thermocouple.

For the SCR tests, the inlet gases were NO, NH_3, O_2, and balance He. Instead, for the roasters emission tests the campaign of catalytic activity tests has been developed and performed according to the following scheme:

- Oxidation of ammonia (inorganic molecule model for nitrogen in the reduced state)
- Oxidation of carbon monoxide
- Oxidation of ethylene, propylene, toluene (VOC model molecules)
- Oxidation of the complete mixture of model molecules
- Oxidation of methanol (roasting probe molecule for VOC)
- Oxidation of the pyridine (roasting probe molecule for the nitrogen in the reduced state)
- Oxidation complete mixture of roasting probe molecules

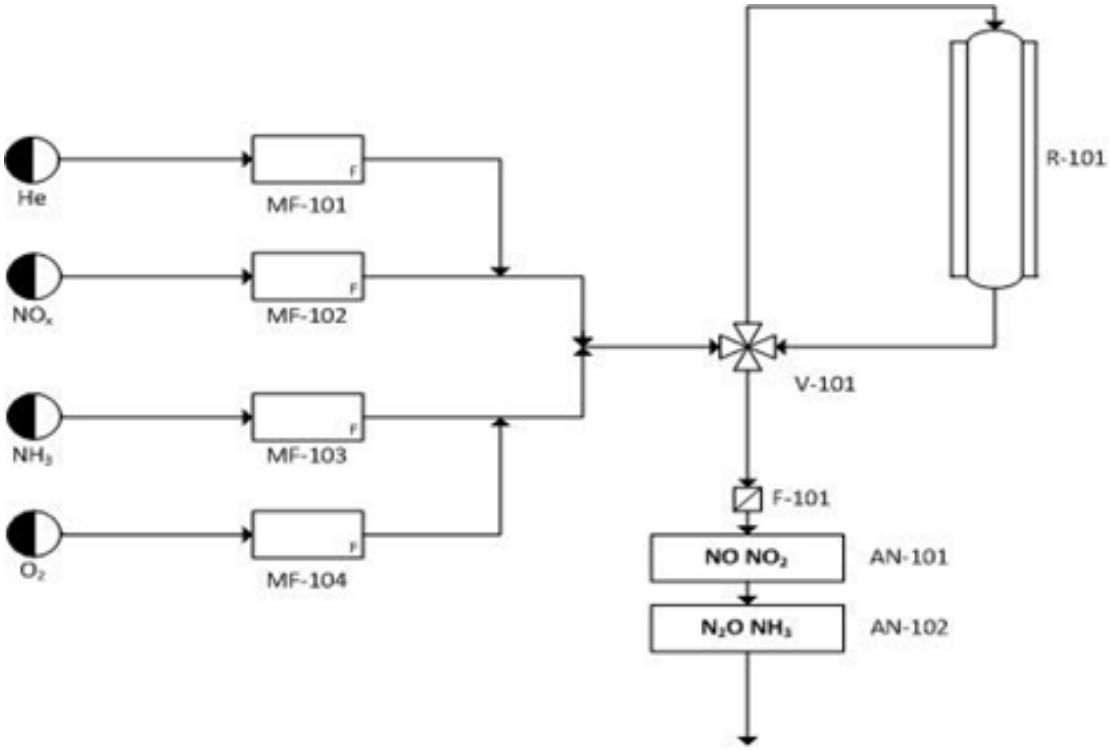

Fig.2.10: Scheme of experimental section

Fig.2.11: Picture of the lab-scale rig for powder

Fig.2.12: Picture of the lab-scale rig with vertical furnace

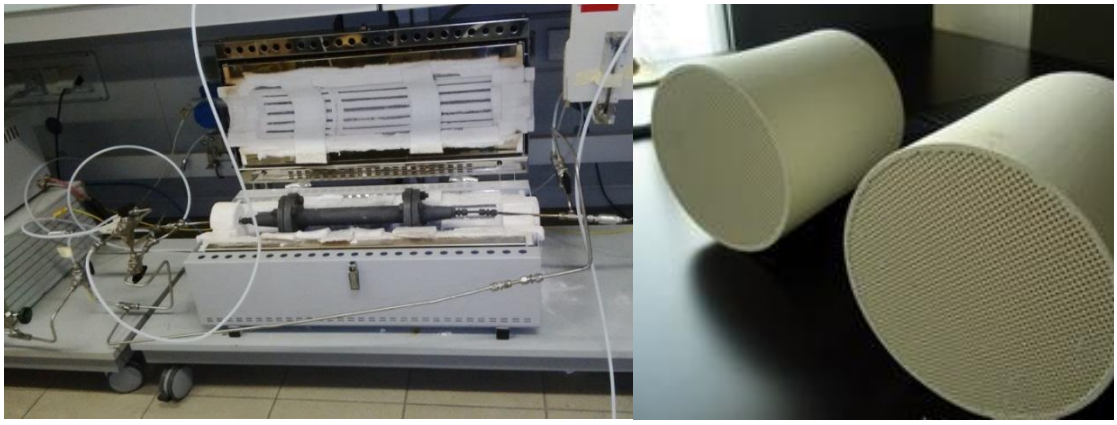

Fig.2.13: Picture of the oven with canning (left) and the honeycomb monoliths (right)

The gases were contained in cylinders at high pressure (50–200 bar) connected to the rig through a reducer, which set the line pressure at 3 bars, and stainless steel lines. The cylinders of NH_3, NO and NO_2 also contained some Helium that was used as a tracer and internal standard for the analysis. Tables 2.2 and 2.3 report some typical values of species concentrations in the gas cylinders.

Table 2.2: values of dilution for the cylinders used for SCR tests

Species	Concentration [ppm]
NH_3	10000
NO	10000
NO_2	20
O_2	pure

Table 2.3: values of dilution for the cylinders used for roasting emissions tests

Species	Concentration [ppm]
NH_3	10000
Pyridine	1001
Toluene	1000
Ethylene	995
Propylene	980
Methanol	1112
CO	1115
O_2	pure

The flows were controlled with Bronkhorst mass-flow controllers; downstream of the mass-flow meters the lab-rig operated at atmospheric pressure.

It is necessary to calibrate periodically the flow controllers to correctly correlate the required gas flow with the percentage opening of their valves.

Once correlated all the values with Flow DDE and Flow View Software it is possible to settle the desired concentration of each species in the reacting mixture.

The NO_x concentration was analysed by means of a NO/NO_2 UV Limas gas analyser, whereas the N_2O and NH_3 concentrations in an Uras nd-IR gas analyser as reported in Fig. 2.14.

Fig. 2.14: UV gas analyser Limas (above), gas analyser Uras (below) and flow meter (left)

The ABB Limas UV analyser is a photometric analyser that combines the low-detection-limit advantage of CLD (Chemiluminescence Detectors) and the well-known advantages of photometers

The Limas UV also allows the simultaneous and continuous measurement of NO, NO_2. NO analysis is based on resonance adsorption. The acquisition is provided by LabView Software. The reliability of the measures is ensured by the beam splitting through an optical chopper with interference filters and a quartz cell as illustrated in Fig.2.15. In addition, the Limas UV eliminates the drawbacks of the common CLD-methods [4].

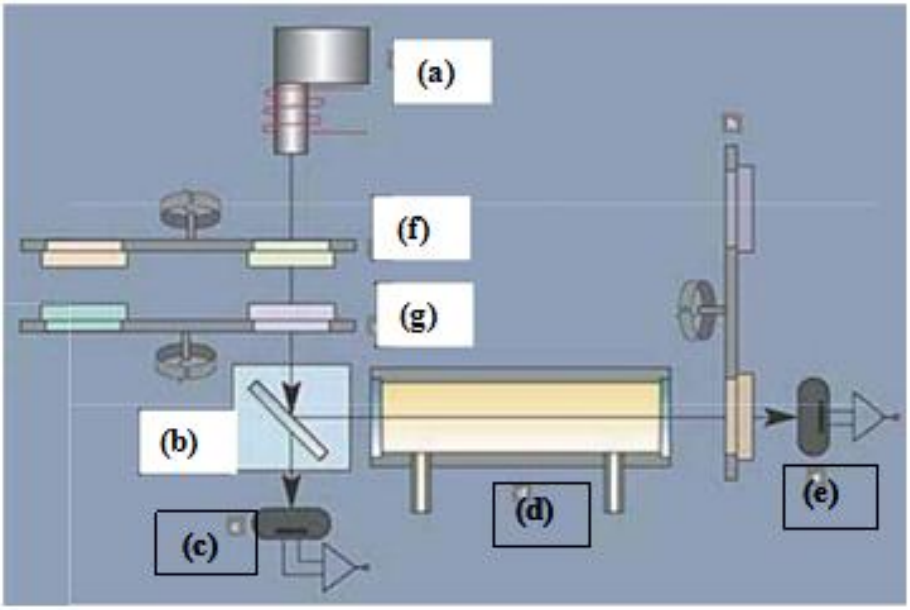

Fig. 2.15: Conceptual diagram of the UV Limas analyser: (a) emitted light, (b) semitransparent mirror, (c) first detector (d) the quartz cell.

The calibration procedure [6] is very important to have reliable values and it consists in:

– zero gas calibration for each component;
– span gas at 95% of full-scale range for each component;
– cross sensitivity of NO and NO_2;
– Periodical re-linearization at 250 ppm.

Table 2.4: values of full-scale for components

Components	Full-scale [ppm]
NO	2500
NO_2	2500

Uras gas analysers have a modular design and analyser modules can be freely combined into tailor-made solutions and upgraded or extended with new features at any time. The ABB Uras 14 allows the continuous measurement of N_2O, NH_3, CO

and CO_2. Its working principle is based on the *Non-Dispersive Infra Re* spectrophotometry (*ND IR*) in a wavelength range between 2.5 and 8 µm.

In Figure 2.17 are illustrated the main components: an IR source (lamp), a sample chamber or light tube, a wavelength filter, and the infrared detector. The gas is pumped (or diffuses) into the sample chamber, and gas concentration is measured electro-optically by its absorption of a specific wavelength in the infrared (IR) [7].

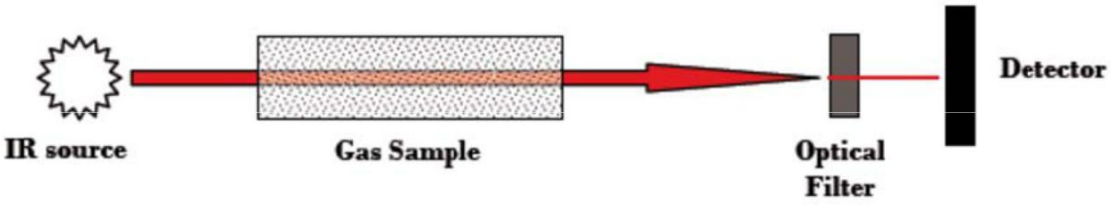

Fig. 2.16- Non-Dispersive Infra Red spectrophotometry conceptual diagram.

All analysers use high performance measurement technology and simplified calibration that doesn't require test gas cylinders.

Table 2.5: values of full-scale for components

Components	Full-scale [ppm]
N_2O	20000
CO	2000
CO_2	10000
NH_3	2000

In the case of oxidative converter, in addition, the CO/CO_2 concentration was measured with Uras nd-IR gas analyser.

2.3 OPERATING TEST CONDITIONS

2.3.1 SCR operating conditions

The measurements of the SCR activity were performed by placing 200 mg of the catalyst in a fixed-bed quartz reactor of 6 mm i.d. under a reacting gas with the following composition: 800 ppm NO, 800 ppm NH_3, 3% O_2, and balance He and GHSV equal to 100000 h^{-1}.

The total flux rate was 400 mL/min measured at RT and atmospheric pressure [8-10].

The study of the SO_2 effect was performed following the same procedure described for the evaluation of the catalytic activity, with a different gas composition.

In the poisoning by SO_2 a mixture of 800 ppm NO, 800 ppm NH_3, 3%O_2, 100 ppm SO_2 and He to balance was used.

The SCR test was also repeated after a regeneration of the catalysts at 400 °C for 2h. The NH_3 oxidation experiments were performed by following the same procedure of catalytic tests, but by employing the following gas composition: 800 ppm NH_3, 3% O_2, and He to balance.

The concentration and the selectivity were calculated from the concentration of the gases according to the following expression:

$$X = \frac{c_{NOx_{in}} + c_{NOx_{out}}}{c_{NOx_{in}}} * 100\% \quad (2.7)$$

$$S = \frac{c_{N_2}}{c_{N_2} + c_{N_2O}} * 100\% \quad (2.8)$$

2.3.2 Roasting emissions test operating conditions

Instead the measurements of the tests with the roasting emissions were performed with a W/F equal to 0.34 and under the conditions reported in Table 2.9-2.15.

The table 2.6 presents data obtained from a simulation in a previous work [10, 11], in which we highlight the features of the current of the roasting process emissions.

Table 2.6: Concentrations in the gas emissions after the oxidative converter

Concentrations in the gas emissions after the oxidative converter		
Vol. flow	0,35	cum/sec
Mass flow	0,24	kg/sec
$\mathbf{x_{CH4}}$	0,00	(vol%)
$\mathbf{x_{CO2}}$	5	(vol%)
$\mathbf{x_{O2}}$	12	(vol%)
$\mathbf{x_{N2}}$	75	(vol%)
$\mathbf{x_{H2O}}$	8	(vol%)
$\mathbf{x_{CO}}$	25	ppm
$\mathbf{x_{NO}}$	500	ppm
$\mathbf{x_{NO2}}$	25	ppm

Concentrations in the gas emissions after the oxidative converter		
T	445	°C
P	1,101	bar,a

From the previous graphs, corresponding to the outgoing and incoming currents in the various steps of the process, it is evident that this is not continuous but periodic spike.

The average values of the NO_2 concentration, obtained by considering both the highs and the values of minimum, are reported in the following table.

Table 2.7: NO_2 concentrations in the gas emissions

NO_2 before catalytic converter [mg/Nm^3]	NO_2 after catalytic converter [mg/Nm^3]
47	**472**

All the tests presented a total flux rate of 500 mL/min measured at RT and atmospheric pressure and a GHSV of 50000 h^{-1} except the tests with the honeycomb monolith (Fig. 2.13) in which the total flux rate was 1000 mL/min and the GHSV 5000 h^{-1} due to the aim to maintain the same W/F of the test with powder.

Oxidation of ammonia (inorganic molecule model for nitrogen in the reduced state)

The conditions of this test are reported in Table 2.18.

Table 2.8: composition test of ammonia oxidation.

Compound	Concentration
NH_3	500 ppm
O_2	12%
He	Remainer

Oxidation of carbon monoxide

The operative conditions for oxidation of carbon monoxide test are reported in Table 2.19.

Table 2.9: composition of the test mixture for the oxidation of carbon monoxide.

Compound	Concentration
CO	500 ppm
O_2	12%
He	Remainer

Oxidation of ethylene, propylene, toluene (VOC model molecules)

The test conditions are reported in Table 2.10.

Table 2.10: composition of the test mixture for the oxidation of VOCs.

Compound	Concentration
VOC	**500 ppm**
O_2	12%
He	Remainer

The oxidation reactions of the various compounds are the following:

$$C_2H_4 + 3O_2 \rightarrow 2CO_2 + 2H_2O$$

$$C_7H_8 + 9O_2 \rightarrow 7CO_2 + 4H_2O$$

$$2C_3H_6 + 9O_2 \rightarrow 6CO_2 + 6H_2O$$

Consequently the conversion is so calculated as:

$$Conversion\ (\%) = \frac{F_{co2}}{\nu F_{VOCin}} x100 \qquad (2.9)$$

in which $F_{VOC,in}$, in is the molar flow rate of VOC input F, F_{CO2} is the molar flow at the outlet of CO_2 in stationary conditions and ν is the number of carbon atoms in the VOC (ethylene, propylene, toluene and the mixture = 2, 3, 7, respectively, then 12 total).

Oxidation of the ethylene

The conditions are reported in Table 2.11.

Table 2.11: composition of the test mixture for the oxidation of ethylene.

Compound	Concentration
Ethylene	**500 ppm**
O_2	12%
He	Remainder

Oxidation of the complete mixture of model molecules

The operating conditions used for these tests are illustrated in Table 2.12.

Table 2.12: Composition of the oxidation test of the complete mixture of model molecules.

Compound	Concentration
CO	**800 ppm**
NH_3	500 ppm
VOC	**500 ppm**
O_2	12%
He	Remainder

Oxidation of methanol (roasting probe molecule for VOC)

The operating conditions used for these tests are listed in Table 2.13.

Table 2.13: composition of the test mixture of methanol oxidation.

Compound	Concentration
Methanol	**500 ppm**
O_2	12%
He	Remainder

Oxidation of the pyridine (roasting probe molecule for the nitrogen in the reduced state)

The operating conditions used for these tests are listed in Table 2.14.

Table 2.14: composition of the test mixture for the oxidation of the pyridine.

Compound	Concentration
Pyridine	**500 ppm**
O_2	12%
He	Remainder

Oxidation complete mixture of roasting probe molecules

The operating conditions used for these tests are listed in Table 2.15.

Table 2.15: composition test of oxidation of the mixture of probe molecules roasting.

Compound	Concentration
CO	**450 ppm**
Pyridine	280 ppm
Methanol	**250 ppm**
O_2	10%
He	Remainder

The same operating condition in the roasting emissions test were developed in powder and honeycomb coated.

2.4 BIBLIOGRAPHY

[1] G. Ertl, H. Knözinger and J.Weitkamp, Handbook of Heterogeneous Catalysis, Vol. 1 (1997), 26, VCM-Wiley.

[2] ThermoQUEST SUITE SOFTWARE TPD/R/O 1100 Operator's Manual.

[3] T. Yamashita, A. Vannice, Temperature-programmed desorption of NO adsorbed on Mn_2O_3 and Mn_3O_4,Appl. Catal.B: Environ. 13 (1997) 141-155

[4] William D. Callister, 2002,2008,"Scienza e Ingegneria dei Materiali: Una introduzione", EdiSES s.r.l.-Napoli.[ISBN:978 88 7959 421 9]

[5] Radboud University Nijmegen, Information on the FESEM (Field-emission Scanning Electron Microscope) - http://www.vcbio.science.ru.nl/public/pdf/fesem_info_eng.pdf

[6] ABB - AO2000 Series Continuous gas Analyser: Limas AO2020 Operator's Manual.

[7] ABB - AO2000 Series Continuous gas Analyser: Uras AO2020 Operator's Manual .

[8] X. Tang, J. Li, L. Sun, J. Hai, Origination of N_2O from NO reduction by NH_3 over -MnO_2 and -Mn_2O_3, Appl. Catal. B: Environ. 99 (2010) 156-162

[9] M. Kang, E.D. Park, J.M. Kim, J. E. Yie, Manganese oxide catalysts for NO_x reduction with NH_3 at low temperatures, Appl. Catal. A: Gen. 327 (2007) 261-269

[10] P.Miotto, Master Degree thesis, "Modellazione del processo di torrefazione del caffè per il dimensionamento del sistema di abbattimento degli NO_x dagli effluenti gassosi", Politecnico di Torino.

[11] M.Onnis, Master Degree thesis, " Ottimizzazione di un sistema SCR per l'abbattimento di NOx da processi di tostatura del caffè"

3.1 MnO_X CATALYSTS

3.1.1 Catalyst preparation

Catalysts synthesized by the SCS method are labelled according to the glycine/nitrate ratio: G1N2 for a glycine/nitrate ratio equal to 1:2 and G2N1 for a glycine/nitrate ratio of 2:1. Manganese (II) nitrate Mn $(NO_3)_2$ tetrahydrate and glycine $C_2H_5NO_2$ were used as reactants without further purification. Both reagents were dissolved in 100 mL of distilled water and left under stirring for 30 min to obtain a homogenous solution. Thereafter the solution was transferred to an alumina bowl and placed in a preheated oven at different temperatures for different times. The effect of the oven temperature on the crystallinity, the morphology and the SSA of the MnO_x obtained were analysed. Samples synthesized at 600 °C reached the completion of the reaction after 20 min while the G1N2 and G2N1 samples treated at 400 °C completely reacted after 1 h and after 1.5 h respectively. Subsequently the samples were collected and hand-crushed in an agate mortar. The final products were characterized by different colours: black for the G1N2 sample and dark brown for the G2N1 one. MnO_x catalysts were also synthesized by means of a co-precipitation method. The aim was to investigate the effect of the synthesis method as well as the influence of other MnO_x phases, not achieved through the SCS technique. The co-precipitation synthesis was carried out following the procedure described by Wang et al. [2] and Hong et al. [3].

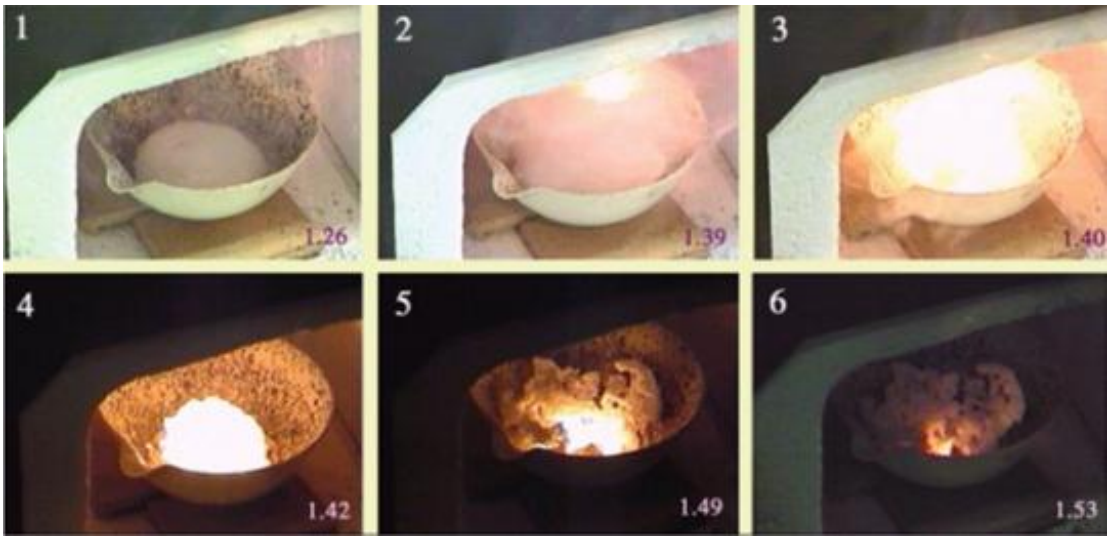

Fig. 3.1: SCS method.

The SCS method is based on an exothermic reaction in which the actors are nitrates of the metals of the desired oxides and an organic fuel, both dissolved in water forming a solution that is put in an oven pre-heated at different temperatures.

The heat supplied causes the very fast evaporation of the water and the decomposition of the reactants, giving rise to an exothermic redox reaction thus producing softly agglomerated nanoparticles of the desired oxide [1].

The AA_400 sample was obtained from the reaction between potassium permanganate $KMnO_4$ and ascorbic acid $C_6H_8O_6$, with a permanganate/acid molar ratio equal to 2/3.

More specifically, it was inserted suitable amounts of the two reactants into two different beakers containing 60 ml of water for the acid and 90 ml for the potassium permanganate.

The two solutions thus obtained were put in agitation for 30 minutes and then mixed together.

The precipitation reaction was easily recognized, producing in a very short time a yellowish precipitate at the bottom of the beaker.

This precipitate was immediately filtered and washed with distilled water and ethanol. Subsequently the sample was left to rest for some hours, dried in an oven at 100 °C, and subsequently calcined at 400 °C for 1 hour.

For the AM_600 sample, the reaction between potassium permanganate and maleic acid $C_4H_4O_4$ was induced with a molar $C_4H_4O_4/KMnO_4$ ratio equal to 1/3, according to literature [3].

The reactants were simultaneously added in a beaker with 20ml of distilled water.

The solution was stirred for two hours and during the first phase of the agitation the occurrence of the reaction was noticed, leading to a slight increase of the temperature of the beaker and to the formation of a black-coloured gel.

By continuing the agitation, a separation of the phased occurred, with the formation of a solid precipitate at the bottom.

The precipitate was collected, washed with distilled water and ethanol, dried at 100 °C for 5 h and finally calcined at 600 °C for 30 min.

3.1.2 Catalysts synthesis and chemical–physical characterization

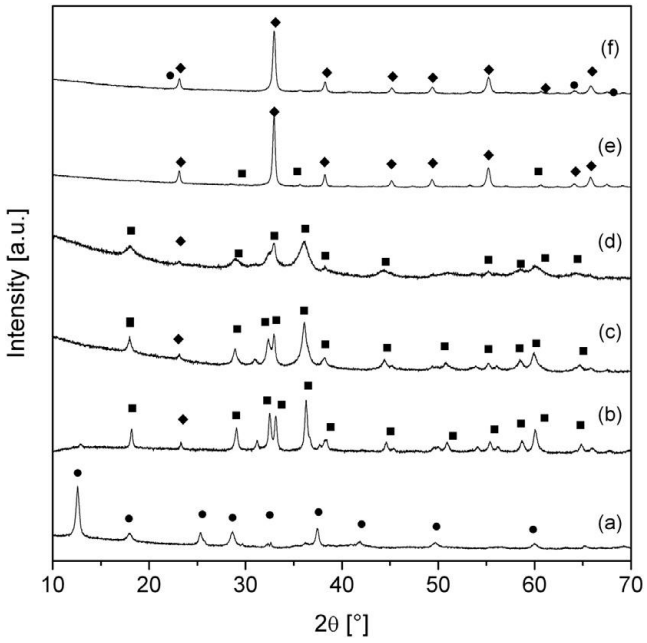

Fig. 3.2. XRD patterns of the MnOx samples synthesized: (a) AM_600, (b) AA_400, (c) G2N1_600, (d) G2N1_400, (e) G1N2_600, (f) G1N2_400 (■: Mn_3O_4, ♦: Mn_2O_3, ●:MnO_2).

The XRD patterns of all samples synthesized are illustrated in Fig. 3.2. All the peaks identified in the patterns corresponded to MnO_x phases. In particular, the peaks of the G1N2 samples matched well with the standard pattern of Mn_2O_3 (reference code JCPDS 41-1442), whereas the G2N1 and the AA_400 samples presented the characteristic peaks of the Mn_3O_4 phase (reference code JCPDS 24-0734).

The AM_600 sample was the only one showing the characteristic peaks of the MnO_2 phase (reference code JCPDS 72-1982).

Moreover, the sample G1N2_400 presented three minor peaks belonging to the standard pattern of the MnO_2 phase (reference code JCPDS 14-0644), while in the pattern of the sample G1N2_600 three small peaks of the Mn_3O_4 phase were identified. In general, the XRD patterns of the samples obtained by SCS at the lowest temperature (G1N2_400 and G2N1_400, AA1K1_400) revealed more weakly crystallized structures than the catalysts synthesized at higher temperatures.

The samples constituted by the Mn_2O_3 phase resulted more crystalline than the ones containing the Mn_3O_4 phase, as evident in Fig. 3.2, where the less broadened peaks for the G1N2 samples suggested that the relatively higher crystallinity was obtained at a higher $Mn(NO_3)_2/C_2H_5O_2$, as also reported by Yu et al. in the synthesis of MnO_2 by means of SCS [4]. In this case, however, different phases (Mn_2O_3 and

Mn_3O_4) were obtained, subsequently meaning different enthalpies of formation. Bixbyite Mn_2O_3 is characterized by an enthalpy of formation of 957-974 kJ/mol, while the one of hausmannite Mn_3O_4 lies in the range 1373-1409 kJ/mol [5].

It follows that for the G1N2 samples the minor quantity of organic fuel brought to lower temperatures suitable for the formation of Mn_2O_3 and the consequent crystallization. For the G2N1 samples, higher temperatures where obtained, though almost all the heat supplied was employed for the formation of the Mn_3O_4 phase and an inadequate fraction was left for crystallization, resulting in more amorphous materials.

Table 3.1: Values of the BET surfaces area and phases detected from XRD of the synthesized samples.

Samples	BET SSA [m^2/g]	XRD		
		Mn_2O_3	**Mn_3O_4**	**MnO_2**
G1N2_400	40	Main phase	--	Secondary phase
G1N2_600	50	Main phase	Traces	--
G2N1_400	80	Traces	Main phase	--
G2N1_600	31	Traces	Main phase	--
AM_600	3	--	--	Main phase
AA1K3_400	74	Traces	Main phase	--

The difference of crystallinity among the samples was consistent with the values of the BET surface area, as reported in Table 3.1.

The G1N2 samples, showing the higher degree of crystallinity and moderate variability with the different temperature of synthesis, were characterized by very similar BET values, in the range between 40 and 50 m^2/g.

On the other hand, the G2N1 samples showed a significant change in the surface area depending on the synthesis temperature.

The catalyst obtained at the lowest temperature showed a considerably high value of 80 m^2/g, whereas, as expected, the increase of the synthesis temperature gave rise to a remarkable decrease of the surface area up to 30 m^2/g.

The samples obtained by the co-precipitation method showed very different behaviours: the AA_400 sample, constituted by the Mn_3O_4 phase, presented a surface area very similar to the G1N2_400 one (74 m^2/g), while the sample

containing the MnO_2 phase was characterized by a very low value (3 m^2/g), considerably lower than the ones measured for the SCS catalysts.

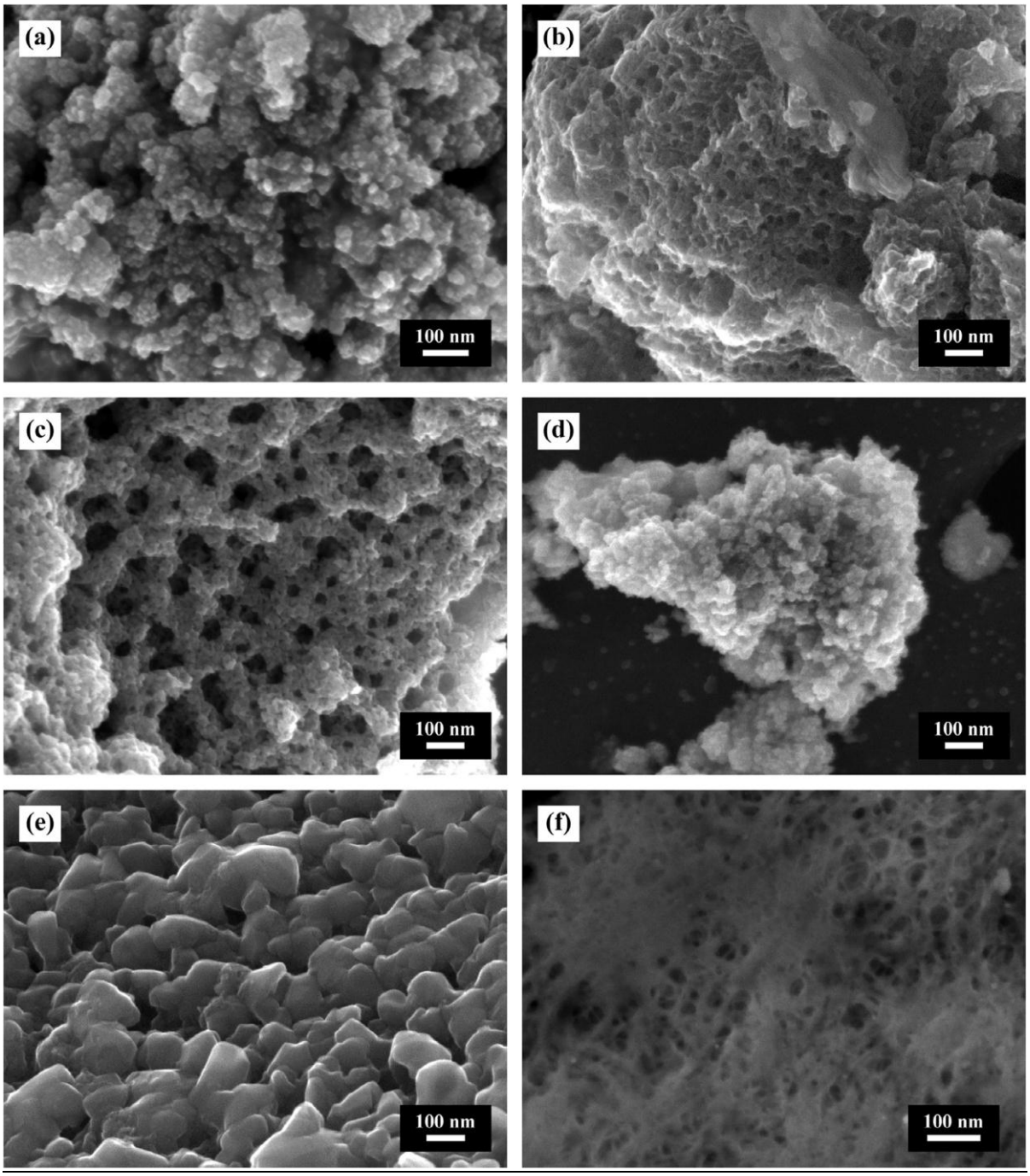

Fig. 3.3. FESEM micrographs of the synthesized samples: (a) G1N2_400; (b) G2N1_400; (c) G1N2_600; (d) G2N1_600; (e) AM_600; (f) AA_400.

The FESEM micrographs are reported in Fig. 3.3.

The analysis conducted for the samples obtained by SCS showed large agglomerates of nanoparticles with spherical shape and an average diameter of less than 60 nm. All samples presented a sponge structure with large alveoli, with the dimension of the porosity in the range between 10 and 50 nm. This kind of

morphology was expected since it is a peculiar feature of the SCS method. The micrographs indicated that the Mn $(NO_3)_2/C_2H_5NO_2$ molar ratio was not significantly affecting the morphology of the catalysts. The samples obtained by means of co-precipitation showed different behaviours: the AM_600 sample was characterized by squared and strongly agglomerated primary particles, with average dimension of less than 100 nm as well as a very small amount of porosities. The level of cohesion of the primary particles was very high, explaining the very low value of BET SSA. On the other hand, the AA_400 sample exhibited a needle-like structure where needles of nanometric diameter were disposed forming a web with a marked presence of porosities.

3.1.3 H_2-TPR and NH_3-TPD analyses

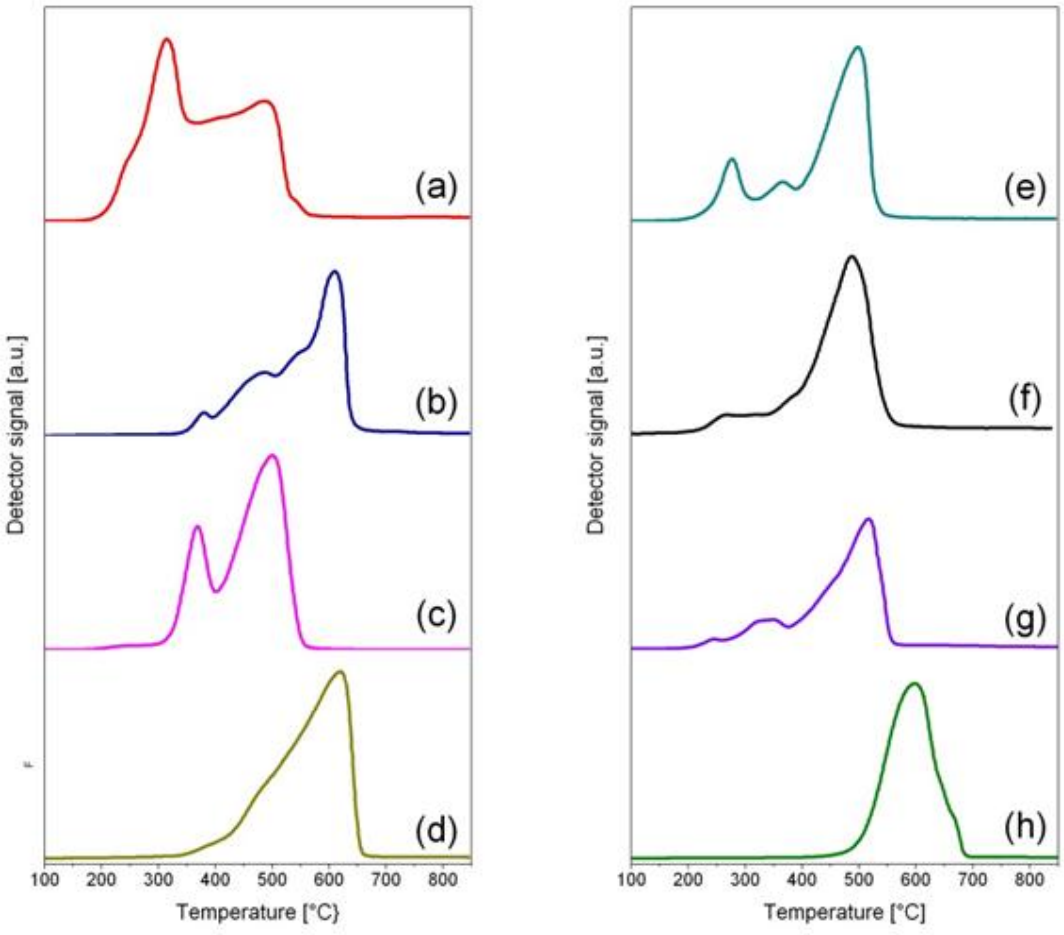

Fig. 3.4 H_2-TPR profiles of the samples: (a) G1N2_400; (b) G1N2_600; (c) AM_600; (d) commercial Mn_2O_3; (e) G2N1_400; (f) G2N1_600; (g) AA_400; (h) commercial Mn_3O_4.

Table 3.2 Summary of the data collected and calculated from the H_2-TPR profiles.

Sample	Main phase detected by XRD	H_2 (µmol/g)	Theoretical amount of Mn	Average oxidation state	H_2/Mn	BET specific area [m^2/g]
G1N2_600	Mn_2O_3	6113	69,6%	2,97	0,48	50
G2N1_600	Mn_3O_4	4285	72,0%	2,65	0,33	31
G1N2_400	Mn_2O_3	7970	69,7%	3,26	0,65	40
G2N1_400	Mn_3O_4	4424	72,0%	2,67	0,34	80
AA_400	Mn_3O_4	5874	72,0%	2,92	0,46	74
AM_600	MnO_2	13303	63,2%	4,38	1,19	3

The curves of H_2-consumption in the range 100–850 °C during TPR analysis are illustrated in Fig.3.4. In fact, in this temperature range, the MnO phase is no more reducible under such levels of H_2 partial pressure as revealed in literature [6] and verified through XRD analysis.

The tests were carried out with the purpose of calculating the H_2-adsorption amount, consolidating the reduction steps and calculating the average oxidation state of manganese.

The samples synthesized at 600 °C are characterized by a higher degree of crystallinity, and consequently their behaviour was consistent with the data present in the literature regarding the reduction of Mn species, more often referring to well-crystallized samples.

According to these, the reduction of MnO_x (at least the first peak of reduction) is proved to occur between 370 and 470 °C. More specifically, the reduction of MnO_2 presents two peaks at 365 and 475 °C, the reduction of Mn_2O_3 exhibits only one peak at 490 °C with a shoulder at a lower temperature as well as the Mn_3O_4 phase, with one peak at 520 °C [7].

In the case of the samples constituted by Mn_2O_3, only the G1N2_600 one showed values of production of water (meaning reduction of the MnO_x phase) corresponding to the theoretical ones of Mn_2O_3, with just one peak and two shoulders.

The quantity of H_2 adsorbed was equal to 6113 µmol/g, as reported in Table 3.2; by employing iterative calculations, it was possible to evaluate the average oxidation state of manganese and the calculated value in this sample corresponded to 2.97,

being the H_2/Mn ratio equal to 0.48, and namely slightly lower than the theoretical value; such a result can be explained with the presence of about 4% fraction of manganese in the oxidation state Mn^{2+}, but more specifically to the presence of 11.5% of the whole manganese species as Mn_3O_4.

This can explain the presence of the two small peaks in the range 350–450 °C, which seemed to accentuate the shoulder present in the standard curve.

The sample G1N2_400 showed two reduction peaks, at 315 °C and 487 °C respectively.

The curve presented the typical M shape of the MnO_2 phase calculated as the 29% of this compound with a H_2-consumption amounting to 7971 µmol/g largely exceeding the theoretical value of Mn_2O_3 (6330 µmol/g).

So the oxidation state for the samples G1N2 decreased by increasing the temperature of synthesis: it was greater than 3 for the sample G1N2_400 and approximately equal to 3 for the G1N2_600 sample, meaning that the former features a significant amount of MnO_2 inside and the latter is an almost pure sample of Mn_2O_3.

Considering the samples G2N1, the average oxidation state was practically equal to 8/3, leading to state that the main phase was Mn_3O_4, in good agreement with the XRD patterns.

The sample G2N1_600 followed the same trend of the standard sample, characterized by only one peak representing the reducing step $Mn_3O_4 \rightarrow MnO$.

The shift to a lower temperature (about 200 °C) is due to the lower crystallinity exhibited by the sample with respect to a strongly crystallized standard [8].

The amount of H_2-consumption was equal to 4285 µmol/g, slightly lower than the theoretical 4370 µmol/g, and consequently the H_2/Mn ratio was 0.33.

The sample G2N1_400 seemed to show the peaks related to the reduction of the γ-MnO_2 phase, which is characterized by a LT peak at 254 °C, a HT peak at 386 °C and finally the main peak.

Again, the shift of the temperature of the peak is due to the lower crystallinity of the sample, as in the case of the sample G2N1_400. As illustrated in Table 3.2, the H_2-consumption amount decreased by increasing the synthesis temperature, from 4424 to 4285 µmol/g.

The AA_400 sample showed a value higher than that of the G2N1 samples; even if the phase should be the same according to the results of the XRD analysis in fact the H_2 consumption amount was 5874 instead of 4424 μmol/g with a consequent higher H_2/Mn ratio of 0.46. All the peaks were shifted at higher temperature probably due to the higher crystallinity despite of the similar BET SSA value.

Finally, the sample AM_600 reported a value higher than 4, corresponding to the presence of Mn in the +4 oxidation state, and hence of the MnO_2 phase, and a shape corresponding to the theoretical one.

In both cases, the amounts of H_2 consumption higher than the theoretical ones were supposed to be caused by the presence of Mn^{7+} ions, deriving from the decomposition of potassium permanganate employed as reactant in the synthesis.

As a final remark of the TPR analysis, one can conclude that among the samples prepared by the SCS method, the G1N2 ones reported a higher Mn oxidation state than the G2N1 samples, while in both cases, the H_2/Mn ratio (and hence, the average oxidation state of manganese) decreased by increasing the temperature of the synthesis.

Therefore, by tailoring the synthesis temperature in the SCS technique it was possible to obtain catalysts with different crystallinity, specific surface area, Mn oxidation state and, finally, reducibility.

On the other hand, the samples synthesized through the co-precipitation technique presented a value almost equal to G1N2_600, in the case of AA_400, and a value higher than 1 for the AM_600 sample.

It is possible to summarize the reduction step as follows: $MnO_2 \rightarrow Mn_2O_3 \rightarrow Mn_3O_4 \rightarrow MnO$ [9].

It is worth to notice that the average Mn oxidation states obtained roughly corresponds to the main phases resulting from the XRD analysis, and the small deviations from the theoretical values, as well as the trend of the curves, are related to traces or secondary phases present in the samples and in some cases also identified in the XRD patterns.

The NH_3- TPD and XPS analysis were performed just for G1N2 and G2N1 samples due to the most significance of the previous results.

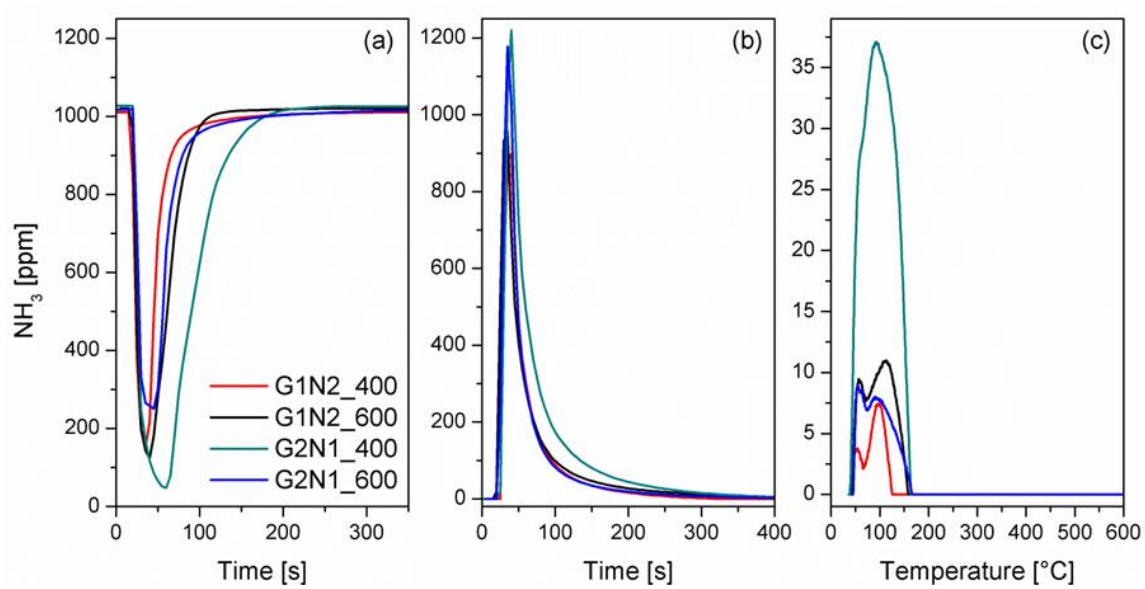

Fig. 3.4. NH_3-TPD profiles: NH_3 adsorption curves at r.t. (a); NH_3 desorption curves at r.t. (b); NH_3 desorption curves at high temperature (c).

The results of NH_3-TPD experiments are reported in Fig. 3.4; the amount of adsorbed and desorbed ammonia, as calculated by integration of the reported curves, is listed in Table 3.3.

Adsorption curves (Fig. 3.4a) showed that the samples exhibited similar NH_3 uptake at r.t., with the exception of G2N1_400 sample, adsorbing a large amount of ammonia. The desorption step at r.t. (Fig. 3.4b) showed a steep increase within 50 s, indicating that most of ammonia was weakly adsorbed (physisorbed) at catalysts surface, with the exception of sample G2N1_400 as confirmed by values of desorbed ammonia in Table 3.3.

The desorption of strongly adsorbed ammonia (Fig. 3.4c) ended at about 170 °C. As reported in Fig. 3.4 (c) G1N2_400 sample mostly physisorbed ammonia that was almost completely desorbed at r.t.

The amount of physisorbed ammonia of the other samples follows the order G2N1_600 > G1N2_600 > G2N1_400.

Accordingly, the amount of strongly adsorbed ammonia with G1N2_600, G1N2_400 and G2N1_600 was much smaller.

The G2N1_400 sample showed the highest amount of strongly adsorbed ammonia (11.7 µmol), indicating the presence of stronger adsorbing sites at the surface, most probably Mn^{4+} species detected by XPS.

Table 3.3: Adsorption/desorption quantities

Sample	Ads Qnt. [μmol]	Desorbed Qnt. [μmol]		
		RT	Ramp	TOT
G1N2_400	11.9	9.6	1.3	10.9
G1N2_600	17.1	11.2	3.2	14.4
G2N1_400	31.3	15.3	11.7	27.0
G2N1_600	15.0	10.8	2.5	13.4

Figure 4 reports the XPS peaks for O 1s and Mn $2p_{3/2}$ lines, from which, by a curve –fit procedure, the following parameters were determined:

i) surface atomic composition,

ii) the content of Mn in different oxidation states,

iii) the percentage of both lattice (O_β) and surface (O_α) oxygen species.

Such parameters are reported in Table 2, along with values of binding energy (BE, eV) and relative atomic percentages of both Mn and O.

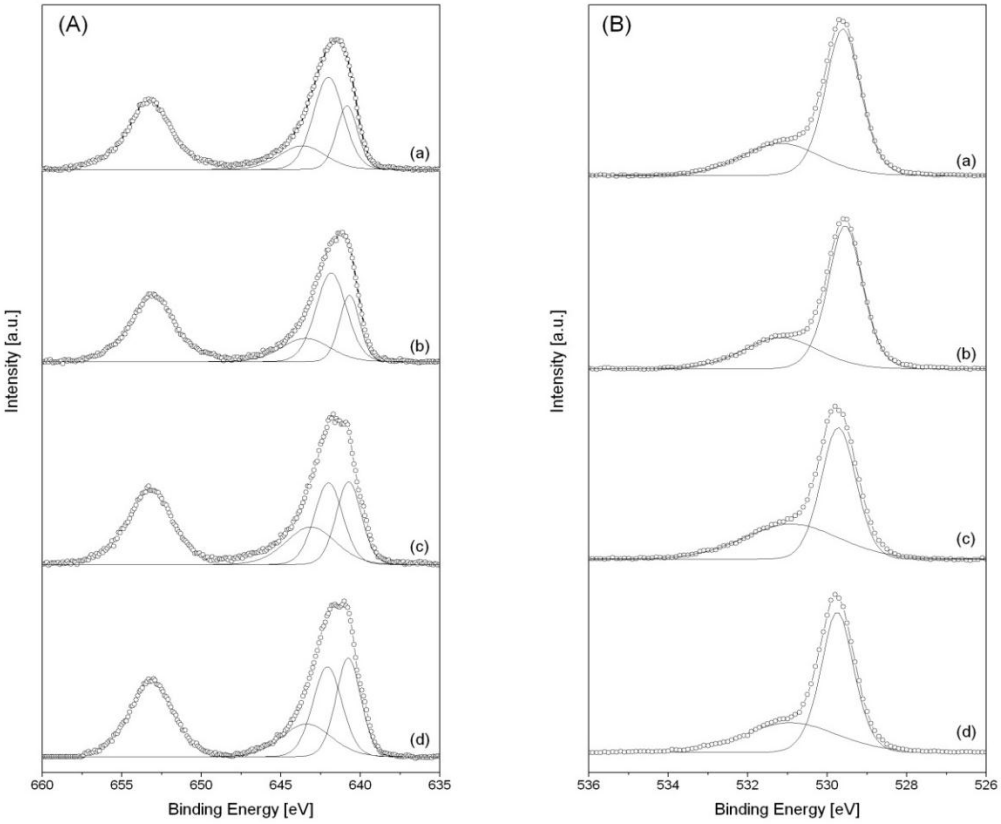

Fig. 3.5. XPS spectra in the O 1s (A) and Mn 2p (B) core level regions of G1N2_400 (a), G1N2_600 (b), G2N1_400 (c) and G2N1_600 (d) samples.

As shown in Fig. 3.5A, all samples exhibited asymmetric peaks in the O 1s region, which was curve-fitted by applying two components.

In literature, the peak in the 592.5-530.0 eV range corresponds to lattice oxygen (*i.e.* O^{2-} ions, referred to as O_β), whereas that in the 531.0-531.7 eV range to surface oxygen species (*.i e.* O_2^{2-}, O^-, OH^- species, referred to as O_α) that are supposed to play a significant role in catalytic processes, due to their high mobility [10,11,12].

All the samples showed both components at almost the same BE values (Fig. 4A), though the relative concentration of O_β and O_α species was different (see O_α/O_β ratio in Table 2).

Both G1N2 samples (mainly containing Mn_2O_3) showed a very similar amount of O_α, whereas G2N1 samples (where Mn_3O_4 was the main phase) featured a higher content of O_α likely due to the presence of a larger amorphous fraction (likely MnO_2).

In particular, the G2N1_400 sample was characterized by the highest O_α/O_β ratio. Kapteijn *et al.* [13] reported that the concentration of O_α is very significant in SCR of NO_x, proposing a model where ammonia is dehydrogenated by O_α, and the formed intermediates react with either nitric oxide or oxygen.

A high concentration of O_α species indeed favours the formation of $-NH_2$ species that react with NO to form N_2.

XP spectra of the Mn 2p region (Fig. 3.5(B)) showed with all samples two peaks attributed to the Mn $2p_{3/2}$ and Mn $2p_{1/2}$ core levels, respectively.

The relative abundance of Mn oxidation states was calculated by a curve-fitting procedure of the Mn $2p_{3/2}$ line. Several values of BE for the different oxidation states of manganese are reported in the literature: in summary, the Mn^{2+}, Mn^{3+} and Mn^{4+} peaks lie in the 640.4-640.8 eV, 641.5-642.0 eV and 642.5-643.8 eV range, respectively [10, 14, and 15].

As expected, the curve-fitting revealed the presence of peaks corresponding to Mn^{2+}, Mn^{3+} and Mn^{4+} species almost in the same positions with all the samples.

For G1N2 samples, Mn^{3+} was the most abundant surface species, leading to a Mn^{3+}/Mn^{2+} ratio slightly exceeding 2, indicating that Mn_2O_3 was the main phase also at the surface.

A considerable amount of Mn^{4+} species was also present at the surface of G1N2 samples, with a Mn^{4+}/Mn^{3+} ratio of about 0.4, likely due to the superficial defects of the manganese oxide lattice. G2N1 samples were characterized by a Mn^{3+}/Mn^{2+} ratio of about 1, in agreement with the fact that Mn_3O_4 was the main phase.

The concentration of surface Mn^{4+} species in G2N1 samples was higher, mainly due to the lower crystallinity degree, which likely leads to a higher content of structural defects with respect to G1N2 samples.

In particular, the G2N1_400 sample showed the highest Mn^{4+}/Mn^{3+} ratio, allowing us to suppose an increased oxidizing behaviour of this sample since its surface contained the largest amount of Mn^{4+} species.

Accordingly, the G2N1_400 sample also exhibits the highest content of surface oxygen (O_α) as well as a very high value of the O_α/O_β ratio (0.72).

Table 3.4: Binding Energy values (BE, eV) and chemical composition (% At) of the studied samples, as obtained by the curve-fitting procedure of O 1s and Mn 2p 3/2 lines.

			G1N2_400	G1N2_600	G2N1_400	G2N1_600
O 1s	O_β	BE (eV)	529.61	529.55	529.72	529.75
		% At	67.69	68.37	58.07	63.10
	O_α	BE (eV)	531.17	531.17	530.91	530.93
		% At	32.31	31.63	41.93	36.90
	O_α/O_β		0.48	0.46	0.72	0.58
Mn $2p_{3/2}$	Mn^{2+}	BE (eV)	640.84	640.68	640.73	640.76
		%At	25.85	25.92	33.20	36.64
	Mn^{3+}	BE (eV)	642.01	641.83	642.00	642.07
		%At	53.55	52.49	37.20	39.17
	Mn^{4+}	BE (eV)	643.64	643.35	643.12	643.39
		%At	20.60	21.59	29.60	24.19
	Mn^{4+}/Mn^{3+}		0.38	0.41	0.79	0.62
	$Mn^{4+}/(Mn^{2+}+Mn^{3+})$		0.26	0.27	0.42	0.32
	Mn^{3+}/Mn^{2+}		2.07	2.02	1.12	1.07

3.1.4 Catalytic activity measurement

The curves of the catalytic activity are illustrated in Fig. 3.6.

In general, the results showed that all samples synthesized by SCS showed a good performance in a sufficient range at low temperatures as well as the AA_400

sample does. Conversely, AM_600 showed a very poor NO_x conversion, approximately limited to no more than 5% in the whole range of temperature investigated.

The selectivity to N_2 obtained in the range from 120 to 300 °C seemed to be the highest among all samples, but this cannot bring one to any positive evaluation about its SCR properties.

More correctly, it seems useful, likely even necessary, that a comparison among selectivity values obtained over the different samples be carried out at equal NO_x conversion level.

However, such a poor conversion is supposed to be caused by the very low value of surface area.

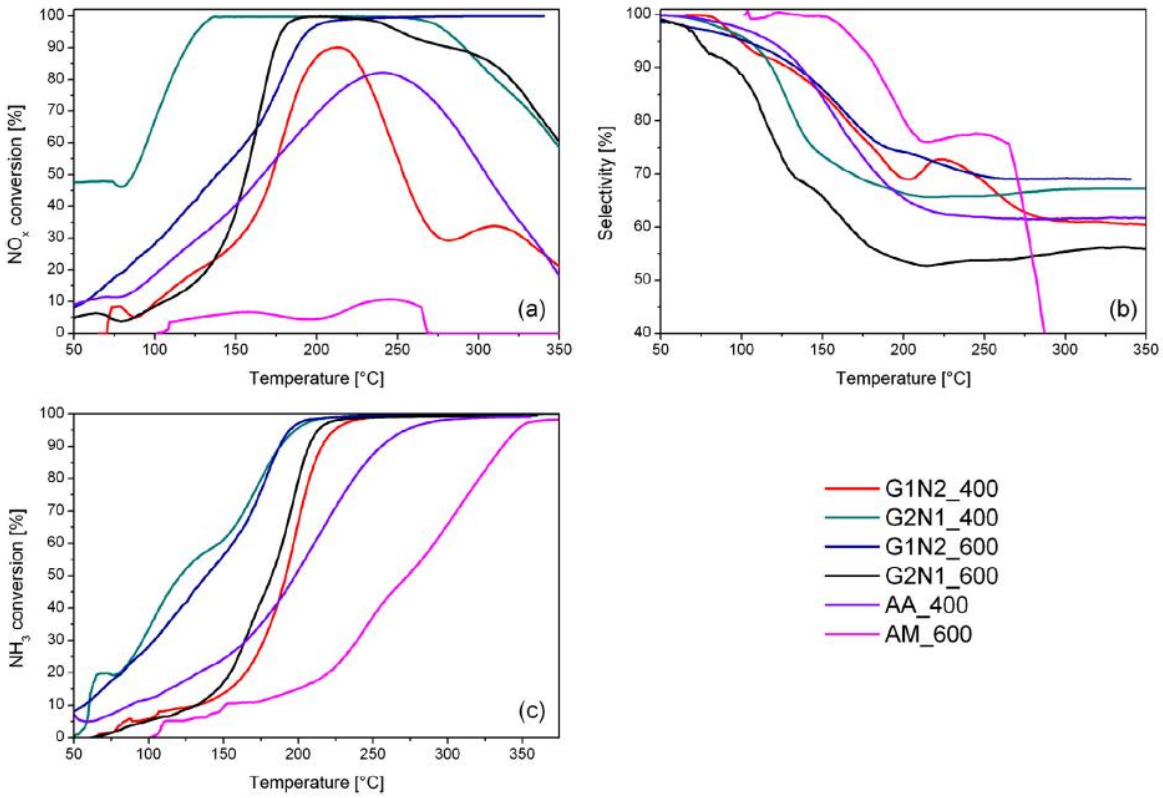

Fig. 3.6. Catalytic activity of the synthesized samples: (a) NO_x conversion; (b) selectivity; (c) NH_3 conversion.

However, all other investigated catalysts are active in the temperature range 120–350 °C and therefore can be considered suitable for working at the low temperature region of SCR process.

More specifically, the NO_x conversion data, considering here as the consumption of NO together with NO_2, showed that the G2N1_400 sample presented the highest

values, the best N_2-selectivity and also the best behaviour of the selectivity at different NO_x conversions.

All the curves followed the same trend, where the conversion presented a maximum and subsequently decreased obtaining a bell curve on the graph.

The decrease from the maximum, not following the typical sigmoidal trend, is clearly attributed to the competition with at least two side reactions: the catalytic oxidation of ammonia to give N_2 or N_2O [16, 17].

Actually, by increasing the temperature, the selectivity decreased for all the samples, due to same phenomenon.

Furthermore, the decrease of selectivity by increasing the nitric oxide conversion at constant temperature suggests that nitrogen and nitrous oxide have a different dependency on the partial pressures of the reactants. After 200 °C, the trend of the selectivity becomes linear.

It can also indicate that a series of reaction mechanisms is involved at the catalyst surface, whereby nitrogen is a first and nitrous oxide is a second nitrogen containing product.

Two nitrogen atoms of N_2O can also come from two different molecules: one from NO and another from NH_3. The decrease of both NO and NO_2 concentrations is coincident with the increase of N_2O concentrations. Moreover, the oxidation of NH_3 over MnO_x is due to the lower bond energy of the surface oxygen, resulting in greater amounts of deep oxidation product (N_2O).

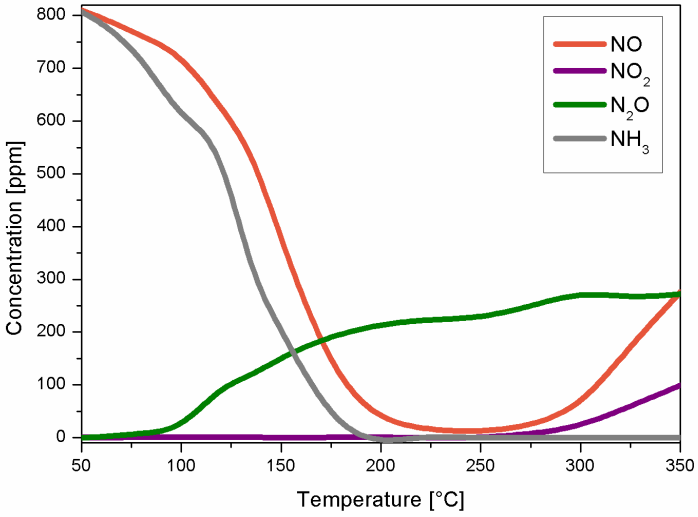

Fig. 3.7. NO, NO_2, N_2O and NH_3 concentrations of G2N1_400 sample.

As demonstration of the conversion and selectivity data, the evolution of the concentrations of the various gaseous species for the most performing sample

(G2N1400) is reported in Fig. 3.7. As can be appreciated, nitric oxide and ammonia showed a monotone decrease to 0 up to 200 °C. After this temperature, the ammonia concentration remained null and the NO one started to increase from 250 °C, when the NH_3 oxidation became prevalent and the formation of NO_2 also occurred. In the meanwhile, the N_2O concentration slowly increased starting from 100 °C, reaching an almost constant value of 250 ppm at about 250 °C. This trend is in good agreement with the values of NO_x conversion and N_2 selectivity illustrated in Fig. 3.6.

The oxidation state of manganese was the main element that governed the N_2O selectivity during the oxidation reaction of NH_3 on the manganese oxides catalysts.

The higher selectivity to N_2O was obtained over samples characterized by higher values of Mn average oxidation state.

From the conversion curves, it can be deduced for the samples synthesized by SCS that the increased surface area led to higher catalytic activity at low temperatures. In fact, the G2N1_400 sample showed the highest value of SSA and the conversion is 100% in a wide range at low temperatures. For the other samples, the surface area gradually decreased and thus the NO_x conversion was progressively reduced, the range of temperature shortened and the peak of maximum conversion shifted at higher temperatures. On the other hand, concerning the MnO_x phase, and consequently the Mn oxidation state, it seemed that the Mn_3O_4 phase could give benefits to the activity with respect to the other MnO_x phases synthesized.

Actually, the comparison between G2N1_400 and AA_400 samples was particularly interesting, because they should be characterized by the same MnO_x phase and almost the same specific surface area, but the co-precipitated sample showed a lower NO_x conversion, with a NO_x conversion plot starting at higher temperatures, and a lower selectivity at temperatures higher than 200 °C, demonstrating that the synthesis method is strongly affecting the catalytic performance.

In the case of SCS, the development of a big amount of gases in a very short time, joint to the high temperatures reached during the synthesis, can create on the surface of the catalyst several defects, in particular oxygen vacancies, which favour the adsorption and consequent oxidation of the ammonia, making this technique very suitable for the NH_3-SCR at low temperature.

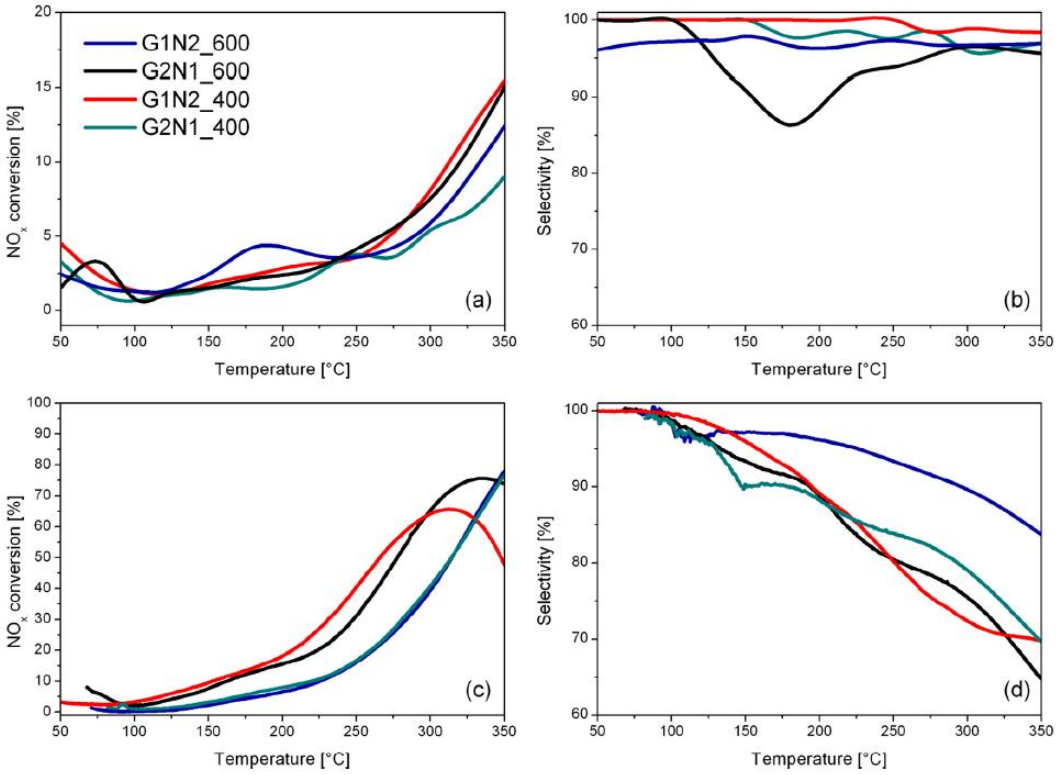

Fig. 3.8. SCR catalytic activity of the SCS samples: (a) NO_x conversion and (b) selectivity in presence of SO_2; (c) NO_x conversion and (d) selectivity after regeneration of the catalysts at 400 °C.

The effect of SO_2 on the catalytic activity was investigated and the results are reported in Fig. 3.8.

It is evident that the conversion was significantly decreased if compared to the test in the absence of sulphur (see Fig. 3.8a and b), as expected also for the very large value of SO_2 concentration involved (100 ppm), which was chosen to accelerate deactivating phenomena.

The presence of SO_2 has a great influence on the acid sites of the catalyst, and thus influences the catalytic activity.

In fact, as reported in the literature, after SO_2 treatment the Lewis acid sites disappeared whereas the Brønsted acid sites were strengthened [18].

In fact, the conversion during the SCR reaction in presence of SO_2 for all the samples was remarkably decreased and the NO_x conversion vs temperature plot shifted towards higher temperatures.

The samples G2N1_600 and G1N2_400 reached a maximum of 16% of conversion of NO at 350 °C in the same condition of the tests carried out with fresh catalysts in the absence of sulphur (namely, with the same contact time).

The G2N1_400 sample, which was the sample showing the best activity and selectivity, was more sensitive to sulphur poisoning than the other samples, but maintained a good performance in the selectivity towards N_2.

The sample G1N2_400 showed the best trend in terms of conversion of NO_x and selectivity towards N_2 and it was possible to notice an adsorption of ammonia on the surface.

After regeneration of the samples at 400 °C, the trend of the curves (Fig. 3.8c and d) showed a considerable improvement of the NO_x conversion, even if not reaching the complete conversion, but always shifted towards higher temperatures.

Moreover, the selectivity was in general higher with respect to the same samples tested in the SCR reaction without SO_2, and research space is opened to develop a better regeneration procedure.

More specifically, the G1N2_400 sample showed a NO_x conversion higher than the other samples until 275 °C, when the conversion started to decrease and the selectivity collapsed deeply.

The samples G1N2_600 and G2N1_400 had the same behaviour, with the conversion increasing by increasing the temperature though the maximum was not reached at 350 °C. However, they differed in the selectivity, which was greater in the case of the sample G1N2_600.

The G2N1_600 sample seemed to show the best catalytic performance, with a maximum of 80% of NO_x conversion at 325 °C.

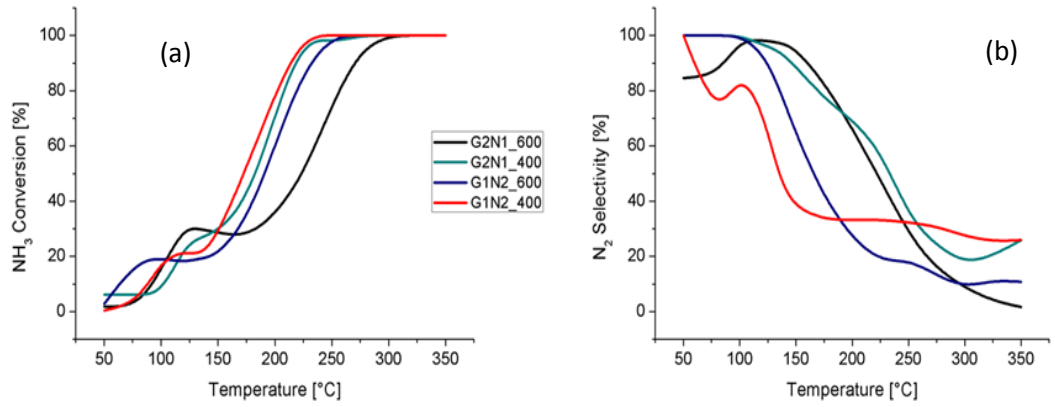

Fig. 3.9: Ammonia oxidation catalytic activity of the SCS samples.

Since the tested catalysts showed a more or less pronounced formation of N_2O in the products, experiments of ammonia oxidation were run in order to understand the

source of N_2O, which can be produced both by molecules of NO reduced by NH_3 (eq. 8) and by NH_3 oxidation (eq. 9) [4].

Fig.3.9 reports curves of NH_3 conversion (a) and selectivity towards N_2 (b): both samples synthesized at 400 °C reached an almost complete NH_3 conversion at lower temperatures than samples obtained at 600 °C, but G2N1_400 showed a higher selectivity to N_2, indicating that with the latter catalyst less N_2O was produced than with G1N2_400.

With G1N2_400, production of a large amount of N_2O started at 180 °C, reached a maximum at 220 °C and subsequently decreased.

The samples with lower selectivity to N_2 were also the same able to oxidize ammonia during NH_3 TPD tests, whereas the most selective was the sample adsorbing the largest amount of ammonia during the same tests.

The samples synthesized at 600 °C presented longer adsorption time of ammonia and this explained the fact that these curves reached the total conversion slowlier than the samples obtained at 400 °C.

The samples G2N1 showed higher aptitude to the N_2 formation, thus increasing the ammonia selective capacity.

3.2 MnO_x-CeO_2 CATALYSTS

3.2.1 Catalyst preparation

For the Ce-Mn mixed oxide catalyst, a key role is played by the synthesis method mixed. So it is possible to find in the recent works new routes for the preparation of MnO_x-CeO_2 catalysts, such as co-precipitation [19], solution combustion synthesis (SCS) [20] and plasma method [21].

The SCS method employed for the synthesis of the catalysts involved the use of two different oxidants, such as glycine ($C_2H_5NO_2$) and citric acid ($C_6H_8O_7$), and different Mn/Ce ratios, in order to investigate the influence of different compositions of the CeO_2-MnO_x system as well as of different synthesis procedures on the catalytic activity.

From the investigation carried out for the MnO_x catalysts, it was concluded that the Mn_3O_4 phase seemed to be a key factor for the achievement of remarkable catalytic performance [22].

Consequently, the following stoichiometric redox reactions were considered in order to get Mn_3O_4 as main MnO_x phase:

$$18Ce(NO_3)_3 + 27Mn(NO_3)_2 + 56C_2H_5NO_2 \rightarrow 18CeO_2 + 9Mn_3O_4 + 82N_2 + 112CO_2 + 140\ H_2O$$

$$18Ce(NO_3)_3 + 27Mn(NO_3)_2 + 28C_6H_8O_7 \rightarrow 18CeO_2 + 9Mn_3O_4 + 54N_2 + 168CO_2 + 112\ H_2O$$

The catalysts can be identified into three groups, depending on the ratio Mn/Ce present and the type of oxidizer.

The samples were labelled as MnXCeY OF±, where X and Y indicated respectively the Mn and Ce quantities in the Mn/Ce molar ratio, OF the abbreviation of the fuel employed and the symbol + or − if the fuel was introduced in a quantity below or above the stoichiometric one, with respect to the nitrate groups present in the reaction. If the symbol was not present, the sample was synthesized under stoichiometric conditions.

The first series of samples was obtained with a Mn/Ce molar ratio equal to one and the use of glycine in both below and above-stoichiometric conditions.

The second involved the use of citric acid, again below and above the stoichiometry, and an equal amount of Mn and Ce atoms (Mn/Ce = 1).

The third group of catalysts showed a molar ratio Mn/Ce equal to 9 and the use of glycine under stoichiometric or below-stoichiometric conditions.

In all cases, the reactants were weighted in suitable amounts in order to obtain 2 g of catalysts and they were subsequently mixed in 100 ml of distilled water for 30 min, obtaining a homogeneous mixture. This was poured inside an alumina capsule and placed in a preheated oven at 600 °C, where it remained for 20 min.

The synthesis temperature of 600 °C was the only considered, since the effect that the temperature has on the activity of the catalysts has previously been examined by Yang et al. [23], demonstrating that the conditions used in this work are optimal for the type of synthesis applied.

A high temperature also ensures greater stability and resistance to thermal degradation, for a possible prolonged use in time.

3.2.2 Catalyst characterization

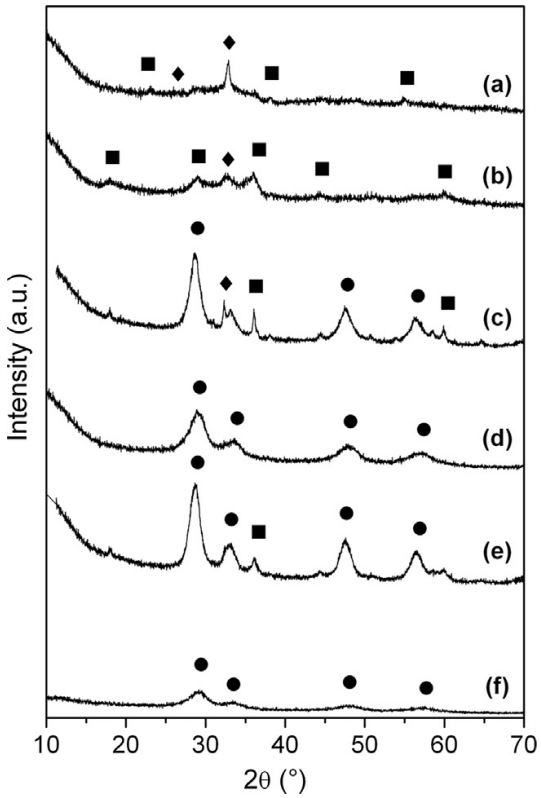

Fig. 3.10. XRD patterns of the MnOx-CeO2catalysts developed: (a) Mn9Ce1 Gly,(b) Mn9Ce1 Gly−, (c) Mn1Ce1 Gly+, (d) Mn1Ce1 Gly−, (e) Mn1Ce1 CA+, (f)Mn1Ce1 CA− (■ Mn_3O_4, ◆Mn_2O_3, ●CeO_2).

The XRD patterns of the MnO_x-CeO_2 samples are presented in Fig. 3.9.

The samples prepared with a low fuel/oxidizer ratio (see Fig. 3.10 (b), (d) and (f)) revealed a generally weaklier crystallized structure, which is a typical behaviour of pure and mixed oxides prepared by means of the SCS method and that was also observed in the pure MnO_x samples developed in paragraph 3.1 [22].

Furthermore, the samples with a Mn/Ce molar ratio of 1 (see Fig. 3.10 (c), (d), (e) and (f)) were rich in CeO_2 so, as can be noticed, the peaks of ceria were predominant and only in the case of the over-stoichiometric reaction with citric acid a small peak of Mn_3O_4 could be identified.

The dominant diffraction peaks corresponded to cerianite CeO_2 (cubic fluorite structure JCPDS 43-1002), where manganese atoms were displaced in interstitial positions to forma Mn-Ce solid solution [24, 25, 26].

The Mn9Ce1_Gly samples (Fig. 3.10 (a)) presented the characteristic peaks of the Mn_3O_4 phase (reference code JCPDS 24-0734) with secondary peaks belonging to Mn_2O_3 (reference code JCPDS 41-1442), with a more significant evidence of Mn_2O_3 for the sample obtained under stoichiometric conditions.

Table 3.5: Values of the BET surfaces area, ICP-MS metal compositions and summary of the data collected and calculated from the H2-TPR profiles of the MnOx-CeO_2 catalysts developed.

Sample	BET SSA (m^2/g)	Adsorbed gas (µmol/g)	Mn mol% (ICP)	Ce mol% (ICP)	H_2/Mn molar ratio	Mn oxidation state
Mn9Ce1_Gly	45	4990	89	11	0.47	2.9
Mn9Ce1_Gly-	32	7120	88	12	0.71	3.4
Mn1Ce1_Gly+	37	3200	76	24	0.35	2.7
Mn1Ce1_Gly-	67	2660	50	50	0.44	2.9
Mn1Ce1_CA+	39	2770	57	43	0.40	2.8
Mn1Ce1_CA-	90	3400	53	47	0.59	3.2
CeO_2	50	1300				

The values of BET specific surface area of the synthesized catalysts are summarized in Table 3.5.

As can be noticed, the SSA of the Mn1Ce1 samples was significantly increased by decreasing the quantity of fuel employed, both glycine and citric acid, due to the lower heat developed during the reaction and consequently the lower degree of crystallinity obtained. The Mn9Ce1 samples followed a similar trend, even if the difference is less marked. Table 1also illustrates the results of the ICP analysis.

For all the catalysts some discrepancies with the theoretical amounts of manganese and cerium can be appreciated, probably due to the partial evaporation of the cerium precursor caused by the high temperatures reached during the synthesis.

The FESEM images of the oxides are reported in Fig. 3.11.

For all the samples, a spongy structure typical of the SCS method can be appreciated, with large agglomerates of nanoparticles and a remarkable amount of porosity.

For the Mn1Ce1 samples, the content of oxidizer played a significant role on the morphology: in fact the pore dimensions and the quantity of alveoli were increased by increasing the amount of either glycine or citric acid, due to the higher temperature reached and thus the higher amount of gases developed during the reaction.

In the case of the Mn9Ce1 samples, the microstructure was very similar to the one of pure MnO_x synthesized through SCS, as illustrated in our previous paper [22].

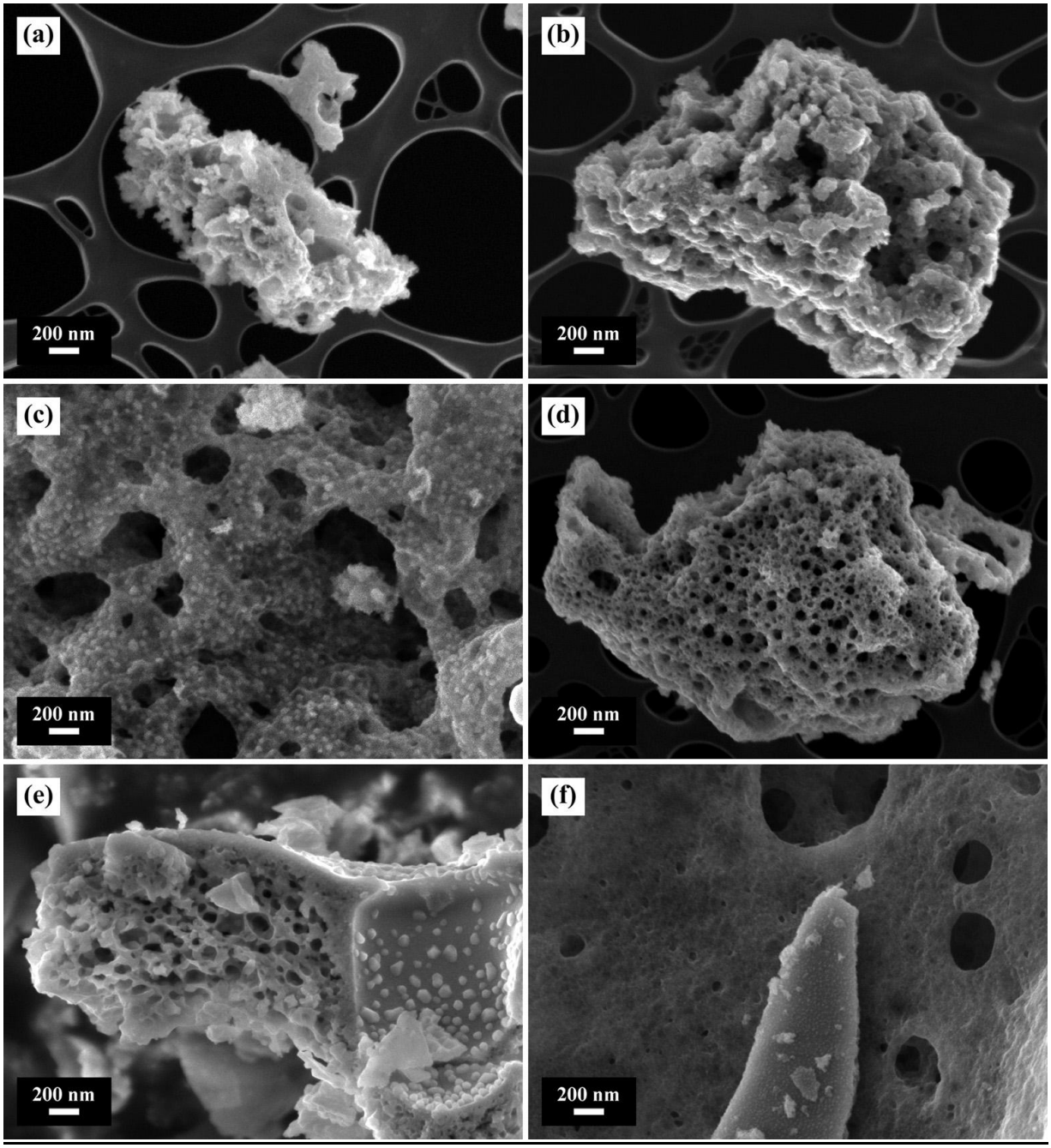

Fig. 3.11. FESEM micrographs of the MnOx-CeO2catalysts developed: (a) Mn9Ce1 Gly, (b) Mn9Ce1 Gly−, (c) Mn1Ce1 Gly+, (d) Mn1Ce1 Gly−, (e) Mn1Ce1 CA+, (f) Mn1Ce1 CA−.

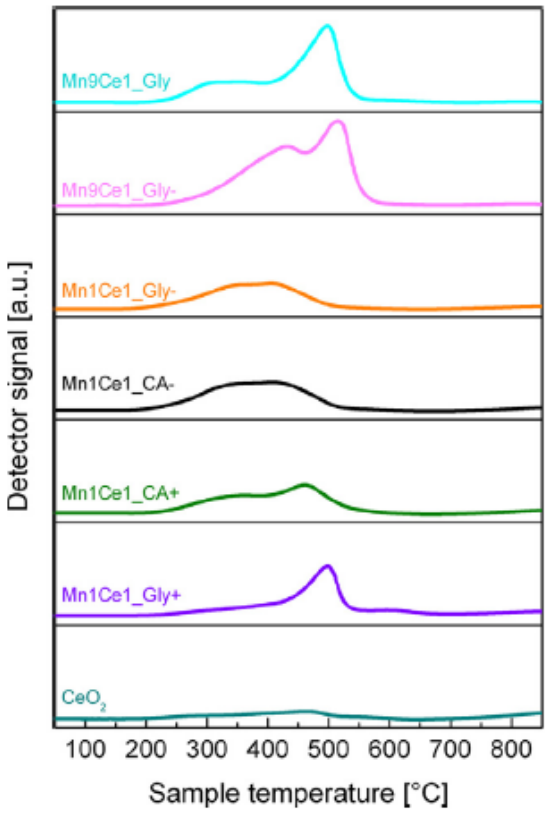

Fig. 3.12: H_2-TPR profiles of the MnO_x-CeO_2 catalysts developed by means of SCS.

The H_2-TPR results of the analysis are shown in Fig. 3.12.

The reduction profiles were displaced in the temperature range of between 250 and 600 °C and almost all the samples showed the presence of either two peaks or one broad peak due to the overlapping of several peaks.

In the previous section, the reduction ability of the pure MnO_x phases was widely investigated, demonstrating that their behaviour was significantly affected by the crystallinity and the specific surface area, in terms of temperature of reduction and amount of reacted hydrogen and, above all, of the Mn average oxidation state [22].

The amounts of H_2 uptake measured in the TPR over the MnO_x catalysts are reported in Table 3.5, together with the results for the MnO_x-CeO_2 samples.

For the MnO_x-CeO_2 samples, the reduction peak at low temperature corresponded to the reduction step from MnO_2 or Mn_2O_3 to Mn_3O_4.

Obviously, the further step of reduction led to MnO. At higher temperature the peak was referred to the reduction of the oxygen on the surface of CeO_2 [24, 27].

According to the literature, the addition of Mn in the CeO_2 decreases the temperatures at which the reduction occurs. The reduction of CeO_2 occurs at around

500–520 °C, associated with the reduction of surface ions Ce^{4+} [28] and at around 700–720 °C the reduction of the bulk takes place [27].

In Fig. 3.11, the TPR profile for ceria synthesized by means of SCS is reported, showing that the first peak occurred at about 470◦C and the second one started at the end of the test, over 800°C.

The Mn9Ce1 samples, which contained MnO_x as principal phase, were characterized by H_2 consumption values in the TPR very similar to pure MnO_x, slightly decreased due to the presence of a small content of ceria (the reduction of ceria in this range of temperature accounted for much lower H_2 uptake than the reduction of manganese).

The sample obtained in below-stoichiometric conditions showed a very large amount of consumed hydrogen (7120 µmol/g), whilst the above-stoichiometric conditions led to a lower quantity of H_2 uptake (4990 µmol/g).

The amount of reduction related to Ce under the present conditions of the TPR tests was very low com-pared to the H_2 uptake attributed to MnO_x species (see Table 3.5: for pure ceria 1300 µmol/g).

By subtracting the estimated contribution of ceria (namely, the contribution of pure ceria experimentally obtained and evaluated for the fraction of CeO_2 present in the sample), it was possible to evaluate the average oxidation state of manganese, which was 2.9 for the Mn9Ce1_Gly sample and 3.4 for the Mn9Ce1 Gly− one, likely due to the presence of superficial Mn^{4+} atoms.

The Mn1Ce1 samples showed a decreased reducibility with respect to the pure MnO_x catalysts, since CeO_2 was the preponderant phase strongly affecting the physico–chemical properties of the samples.

The values showed certain variability, in the range 2660–3400 µmol/g, mainly depending on crystallinity and SSA. Also in this case, the subtraction of the CeO_2 contribution led to calculate an average Mn oxidation state in the range between 2.7 (predominant Mn_3O_4 phase) and 3.2.

By analysing the profile of the curves, it can be noticed that the temperatures of the peaks varied with the crystallinity of the synthesized sample and with the CeO_2/MnO_x ratio.

Comparing the MnO_x-CeO_2 catalysts with the MnO_x ones, the first featured a shift of the peak towards lower temperatures.

The samples synthesized by using glycine showed a different behaviour depending on the Mn/Gly ratio and consequently on the crystallinity of the samples.

If the ratio was greater or equal to one the curve had a single peak with a shoulder. On the other hand, if the ratio was below 1 the shoulder was much more pronounced as well as the second peak was significantly decreased and a broad signal was detected in the temperature range.

This was likely due to the higher amount of crystallized Mn_3O_4 in the samples obtained under above-stoichiometric conditions rather than the counterparts synthesized under below-stoichiometric conditions, because the heat generated during the synthesis for the higher amount of organic fuel allowed to better crystallize the Mn_3O_4 phase.

A similar trend was found in the samples prepared by using citric acid.

The Mn9Ce1 samples showed an increased reducibility with respect to the Mn1Ce1 catalysts, due to the augmented amount of MnO_x.

In both cases the profiles presented two peaks.

For the sample obtained under below-stoichiometric conditions, a little shift of the peaks towards higher temperatures occurred, from 353 to 430 °C for the first peak and from 498 to 515 °C for the second one.

The XPS characteristic peaks for Mn $2p_{3/2}$, Ce 3d and O 1s are illustrated in Fig. 3.12. From the core–fit analysis of the characteristic peaks it was possible to understand the atomic composition of the surface of the catalysts and subsequently the content of manganese atoms and cerium atoms in different oxidation states as well as the percentage of lattice and surface oxygen atoms.

The binding energies and the relative percentage of each component of Mn, Ce and O atoms are given in Table 3.6.Concerning oxygen, it is reported in the literature that O_β could be assigned to the lattice oxygen and O_α to the surface chemisorbed oxygen [11].

As illustrated by the curves, all samples exhibited an asymmetric peak in the O 1s region, which was formed by two different components.

The peak in the range 592.5-530.0 eV corresponded to lattice oxygen (O^{2-}), whereas the one in the range 530.7-531.7 eV was associated with the surface-adsorbed oxygen (O_α), also known as O_2^{2-} or O^- [12].

It has been reported that O_α plays a key role in the SCR reaction and a high content of labile oxygen (expressed in Table 3.6 by the O_α/O_β ratio) can enhance the catalytic performance [29].

It is worth to notice that the ratio is nearly the same for all the catalysts analysed except for the Mn9Ce1_Gly sample, featuring a significantly higher content of chemisorbed oxygen.

The XPS spectra of the Mn 2p region showed for all the samples two peaks, which were attributed to the Mn $2p_{3/2}$ and Mn $2p_{1/2}$ core levels respectively.

The relative abundance of the Mn oxidation states was calculated by core-fitting of the Mn $2p_{3/2}$ core level.

In the literature, several binding energies are reported for the different valence of manganese.

It can be assumed that the Mn^{2+} peak lies in the range 640.4-640.8 eV, the Mn^{3+} one in the range 641.5-642.0 eV and the Mn^{4+} one between 642.5 and 643.8 eV [11, 30, and 31].

The analysis revealed the presence of the peaks of the Mn^{2+}, Mn^{3+} and Mn^{4+} species almost in the same positions for all the samples.

As in the analysis of the O 1s region, the Mn9Ce1_Gly sample was the only catalyst showing different properties, with a content of Mn^{4+} atoms significantly higher than the other catalysts and a considerably higher content of Mn^{2+} atoms meaning that by tailoring the Mn/Ce ratio and the synthesis parameters it was possible to get different superficial composition of the catalyst, in particular to increase the Mn^{4+}content that is likely supposed to improve the performance.

Concerning the cerium atoms, the region Ce 3d was analysed.

It is well known that the oxidation states of cerium present several peaks often overlapped and the core-fitting analysis can be very complicated.

The u''', u″, u, v''', v″, v peaks were considered for the Ce^{4+} state while the u' and v' peaks were attributed to the Ce^{3+} state [32, 33].

As reported in Table 3.6, all the samples showed peaks almost in the same positions.

It has been demonstrated that high oxygen storage release ability of ceria is related to the excellent reducibility through the redox shift between Ce^{4+} and Ce^{3+}.

For this reason, it is interesting to evaluate the concentration of Ce^{3+} atoms, expressed as $Ce^{3+}/ (Ce^{3+}+Ce^{4+})$ ratio.

The amount of Ce^{3+} is considerably lower for the Mn9Ce1 samples than for the Mn1Ce1 samples, since the amount of cerium oxide in the first case was significantly lower.

Nevertheless, by referring the values to the different composition of the catalysts it is possible to highlight that the Mn9Ce1_Gly sample presented the higher content of Ce^{3+} atoms on the surface.

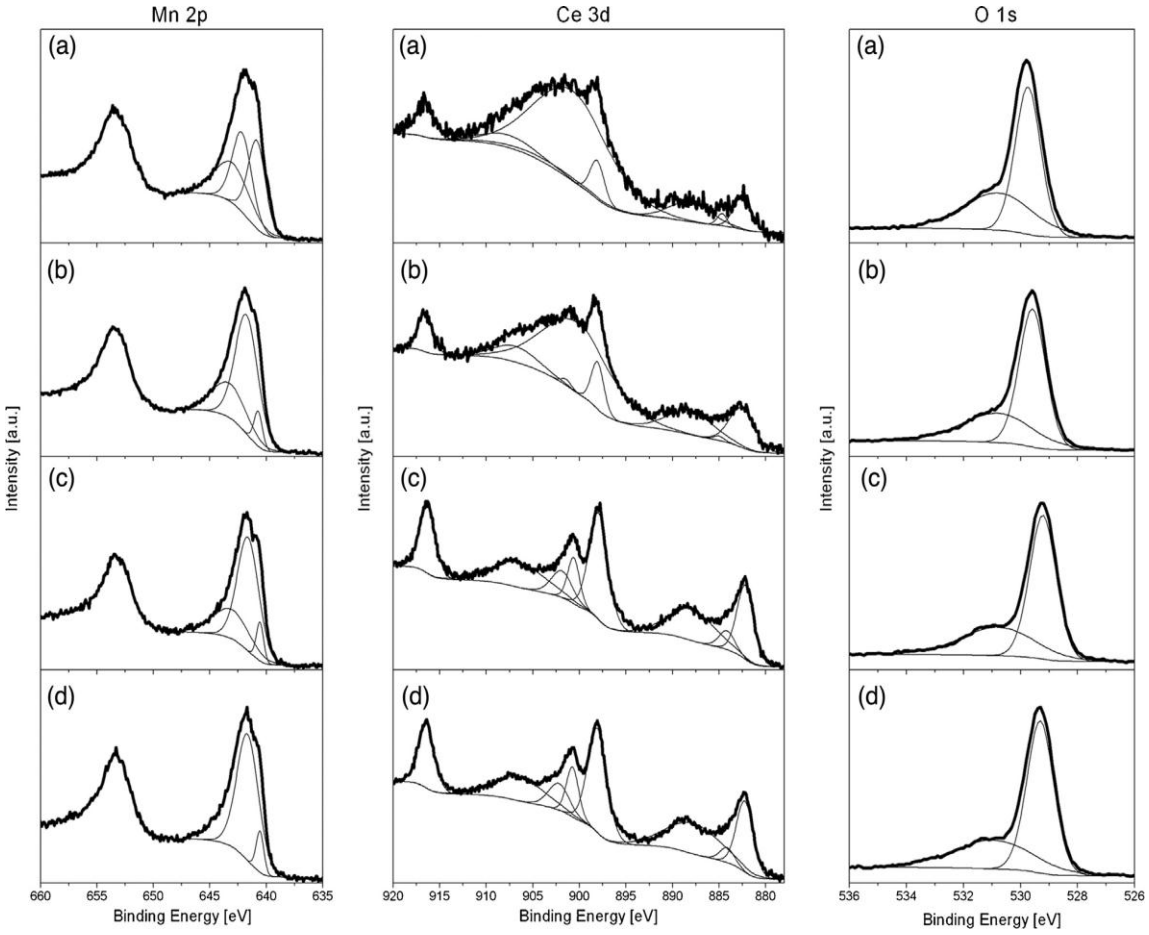

Fig. 3.13. Mn 2p (left), Ce 3d (centre) and O 1s (right) core level spectra of XPS of the catalysts developed: (a) Mn9Ce1 Gly, (b) Mn9Ce1 Gly−, (c) Mn1Ce1 Gly−, (d) Mn1Ce1 CA−. Table 2 Binding energies and atomic surface composition from XPS spectra of the MnO_x-CeO_2 catalysts developed.

Table 3.6: Binding energies and atomic surface composition from XPS spectra of the MnO_x-CeO_2 catalysts developed.

Sample			Mn9Ce1_Gly	Mn9Ce1_Gly-	Mn1Ce1_Gly-	Mn1Ce1_CA-
O 1s	O_β	BE [eV]	529.74	529.59	529.22	529.31
		%At	58.6	63.4	64.5	63.9
	O_α	BE [eV]	530.78	530.81	530.79	530.96
		%At	41.4	36.6	35.5	36.1
	O_α/O_β		0.71	0.58	0.55	0.56
Mn 2p	Mn^{2+}	BE [eV]	640.84	640.73	640.57	640.57
		%At	34.1	6.9	7.3	7.4
	Mn^{3+}	BE [eV]	642.16	641.75	641.61	641.65
		%At	34.5	64.3	64.1	66.1
	Mn^{4+}	BE [eV]	643.04	643.30	643.11	643.23
		%At	31.4	28.7	28.6	26.4
	$Mn^{4+}/(Mn^{3+}+Mn^{2+})$		0.46	0.40	0.40	0.36
Ce 3d	u'''	BE [eV]	916.64	916.57	916.35	916.45
		%At	6.2	6.5	26.6	12.4
	u''	BE [eV]	907.73	906.64	906.57	906.52
		%At	6.4	7.7	13.0	14.1
	u'	BE [eV]	903.80	901.40	901.89	902.22
		%At	3.3	0.6	5.5	6.6
	u	BE [eV]	900.80	900.22	900.62	900.74
		%At	64.6	54.6	5.4	7.2
	v'''	BE [eV]	898.10	898.05	897.94	898.07
		%At	5.1	6.6	19.9	23.5
	v''	BE [eV]	888.10	888.12	888.01	887.82
		%At	7.8	12.1	14.2	19.7
	v'	BE [eV]	884.70	885.00	884.16	884.15
		%At	1.1	0.5	2.9	2.5
	v	BE [eV]	882.51	882.55	882.17	882.24
		%At	5.4	11.3	12.4	14.0
	$Ce^{3+}/(Ce^{3+}+Ce^{4+})$		0.044	0.011	0.084	0.091

3.2.3 Catalytic activity

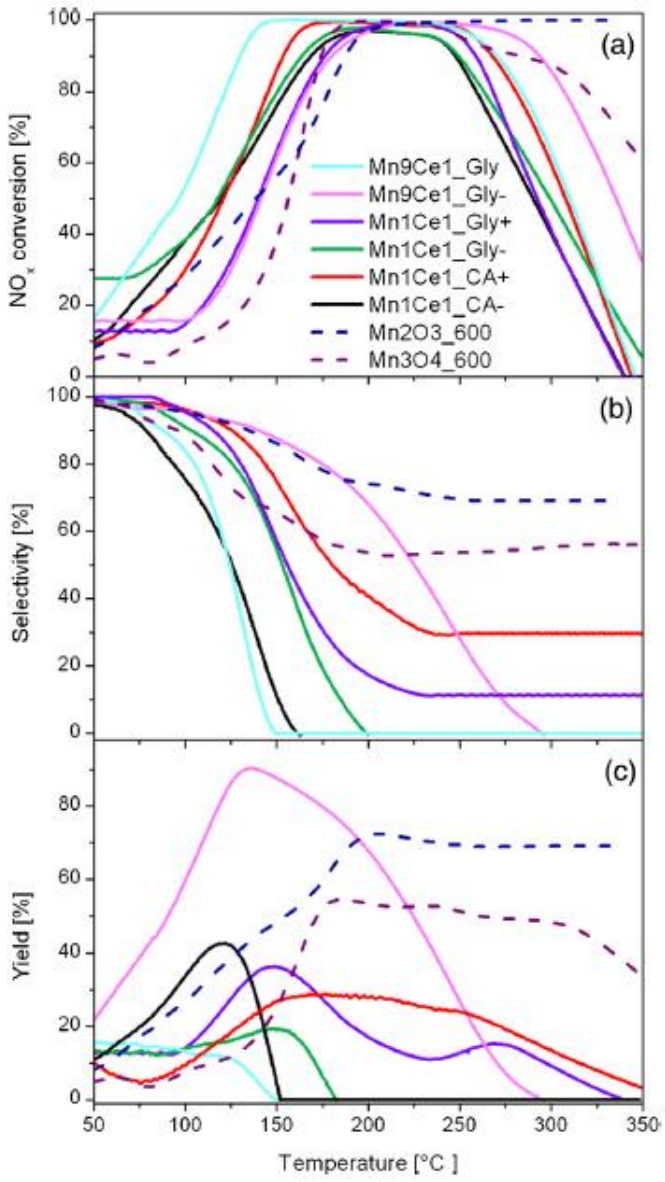

Fig. 3.14 illustrates the curves of the catalytic activity of the MnO_x-CeO_2 catalysts developed.

The performance of two MnO_x catalysts, as reported in paragraph 3.1.4, is illustrated (dashed lines) for a better comparison.

The MnO_x samples also characterized and tested detailed in paragraphs 3.1 and following, synthesized at 400 °C were not reported, although one of them showed higher NO_x conversion and N_2 selectivity, because the comparison was incorrect from our point of view due to the different temperatures of synthesis.

Fig. 3.14. Catalytic activity of the MnO_x-CeO_2 catalysts developed and of two MnO_x catalysts obtained by SCS [4]: (a) NO_x conversion; (b) selectivity; (c) yield.

At lower T, not only SSA were obviously higher, but also the phases obtained were less stable, and consequently we focused the attention as well as the comparison only on the catalysts prepared via SCS ignited at 600 °C.

The results of Fig. 3.14a showed that all the MnO_x-CeO_2 samples exhibited a good performance in a range of temperature of 130–250 °C. It is worth to highlight that the test conditions, particularly the space velocity, were considerably strict and thus the results of the catalytic activity were even more interesting.

The trend was similar for all samples with a bell shape characterized by a range of maximum activity and a subsequent decrease.

This behaviour was clearly caused by the competition of the NO_x reduction with at least two side reactions: the catalytic oxidation of ammonia to give N_2 and the similar one to produce N_2O [16, 17]. The Mn9Ce1_Gly sample showed the best trend in NO_x conversion, reaching 100% for a wide range at low temperature. Its catalytic performance was likely due to the higher BET SSA value, the higher superficial amounts of labile oxygen, Mn^{4+}atoms as well as of Ce^{3+} in comparison to the sample with the same amount of cerium oxide, though its amount of H_2 uptake not corresponded to this behaviour.

For the other samples, the NO_x conversion reached values higher than 90%, though the window of maximum activity was shifted at higher temperatures.

If compared with two different phases (Mn_2O_3 and Mn_3O_4) of pure MnO_x, the MnO_x-CeO_2 catalysts showed in general a better behaviour at low temperatures (up to 150 °C), reaching the complete NO_x conversion at temperatures lower than the pure MnO_x.

In particular, the sample Mn9Ce1_Gly showed a decrease of this temperature of about 25 °C.

The performance of MnO_x-CeO_2 catalysts was compared also with the data found in the literature of similar samples synthesized by different methods, mainly co-precipitation and incipient wet impregnation (IWI) [34, 35].

It resulted that the NO_x conversion as well as the reaction velocity of the catalysts obtained by co-precipitation was lower than the SCS catalysts developed. Similarly, the Mn-Ce catalysts supported on carbon nanotubes through IWI showed a slower kinetic and a lower NO_x conversion that the samples investigated in this work.

Concerning the selectivity to N_2 (Fig. 3.14b), for all the samples it decreased by increasing the temperature, due to the progressive promotion of the reduction reaction leading to N_2O as product in agreement with the results present in literature [16,17].

The Mn9Ce1_Gly sample showed a drastic decrease, with a selectivity of 0 at 150°C. The Mn1Ce1 CA− showed a similar trend, whereas the other samples presented selectivity gradually improved and the samples Mn9Ce_Gly− and Mn1Ce1_Gly+ exhibited the best behaviour.

The comparison of these results with the ones of the MnO_x samples highlighted the better performance of the pure manganese oxides in terms of N_2 selectivity, even if the Mn9Ce1_Gly− sample exhibited a sufficient selectivity for a considerable range of temperature.

So the results of conversion and selectivity were rather contrasting, with a doubtful evaluation of the performance for practical application.

Nevertheless, the overall behaviour has to be evaluated, considering both NO_x conversion and selectivity.

In fact, the yield graph (Fig. 3.14c) shows that the Mn9Ce1_Gly− sample was not the one characterized by the best performance, but the corresponding one obtained under below-stoichiometric conditions was the only exhibiting a sufficient level of yield in a wide range of temperature, up to 200 °C.

This catalyst showed a yield higher than the pure MnO_x, especially in the range of low temperature, proving that the addition of ceria to manganese oxide is able to improve the catalytic performance at low T.

On the other hand, the Mn_2O_3 and Mn_3O_4 catalysts showed a nearly constant yield also for temperatures higher than 200 °C.

It follows that the Mn9Ce1_Gly− sample showed a superior performance, mainly in terms of N_2 selectivity and consequently N_2 yield, with respect to the similar Mn9Ce1_Gly one, that exhibited very similar chemical-physical properties.

This is likely due to the presence in the first one of Mn_3O_4 as main constituent and Mn_2O_3 as second phase, as illustrated by the XRD pattern, whereas the latter showed an opposite composition.

It has been reported in the literature that the Mn_2O_3 phase favours the NO_x conversion while the Mn_3O_4 one the selectivity towards N_2 [36–39].

The present findings perfectly agree with the general conclusion reached in our previous work, because it resulted evident that the maximization of the Mn_3O_4 phase is the key point to obtain active and selective catalysts for ammonia SCR, as we are concluding for Ce-Mn samples.

So, the SCS synthesis performed with glycine under below-stoichiometric conditions for the preparation of MnO_x catalysts with a small amount of ceria allows obtaining successful results for the low-T SCR.

The other MnO_x-CeO_2 samples exhibited either a large window of activity but a yield lower than 35% (i.d. the samples Mn1Ce1_Gly+ and Mn1Ce1_CA+), or a

shorter working range shifted towards low temperatures but still a moderate yield, lower than 50% (samples Mn1Ce1_CA− and Mn9Ce1_Gly−).

The insufficient selectivity of the Mn9Ce1_Gly sample considerably hindered its overall performance, with the yield nullified over 150 °C.

A similar behaviour was observed for the sample Mn1Ce1_Gly−.Although the Mn9Ce1_Gly sample showed very interesting superficial properties, explaining its high conversion in a wide range of temperature, the main MnO_x phase and higher reducibility of Mn9Ce1_Gly− significantly improved its selectivity and consequently the overall performance.

However, it is worth to evidence that all the investigated catalysts are active in the temperature range 120–350 °C and therefore can be considered adapt for working at the low temperature region of the SCR process.

3.3 BIBLIOGRAPHY

[1] A. Civera, M. Pavese, G. Saracco, V. Specchia, Combustion synthesis of perovskite-type catalysts for natural gas combustion, Catal. Today 83 (2003) 199-211.

[2] Y.T. Wang, A.H. Lu, H.-L. Zhang, W.C. Li, Synthesis of nanostructured Mesopours Manganese Oxides with three-dimensional frameworks and their application in supercapacitors, J. Phys. Chem. C 115 (2011) 5413-5421.

[3] X. Hong, G. Zhang, Y. Zhu, H. Yang, Sol-gel synthesis and characterization of mesopourous manganese oxide, Mater. Res. Bull. 38 (2003) 1695–1703

[4] P. Yu, X. Zhang, Y. Chen, Y. Ma, Solution-combustion synthesis of ε-MnO_2 for supercapacitors, Mater. Letters 64 (2010) 61-64

[5] A.N. Grundy, B. Hallstedt, L.J. Gauckler, Assessment of the Mn-O System, J. Phase Equilib. 24 (2003) 21-39.

[6] Y.F. Han, F. Chen, Z. Zhong, K. Ramesh, L. Chen, E. Widjaja, Controlled Synthesis, Characterization, and Catalytic Properties of Mn_2O_3 and Mn_3O_4 Nanoparticles Supported on Mesoporous Silica SBA-15, J. Phys. Chem. B 110 (2006) 24450-24456.

[7] D. Delimaris, T. Ioannides , VOC oxidation over MnO_x–CeO_2 catalysts prepared by a combustion method , Mater Letters 84 (2008) 303-312

[8] E.R. Stobbe, B.A. de Boer, J.W. Geus, The reduction and oxidation behaviour of manganese oxides , Catal. Today 47 (1999) 161-167

[9] M. Sun, B. Lan, L. Yun, F. Ye, W. Song, J. He, G. Diao, Y. Zheng, Manganese oxides with different crystalline structures: Facile hydrothermal synthesis and catalytic activities, Materials Letters 86 (2012) 18-20

[10] M. Kang, E.D. Park, J.M. Kim, J. E. Yie, Manganese oxide catalysts for NO_x reduction with NH_3 at low temperatures, Appl. Catal. A: Gen. 327 (2007) 261-269

[11] L. Wang, B. Huang , Y. Su , G. Zhou , K. Wang, H. Luo , D. Ye , Manganese oxides supported on multi-walled carbon nanotubes for selective catalytic reduction of NO with NH_3: Catalytic activity and characterization, Chem.l Eng. J. 192 (2012) 232-241

[12] F. Larachia, J. Pierre, A. Adnot, A. Bernis, Ce 3d XPS study of composite $Ce_xMn_{1-x}O_{2-y}$ wet oxidation catalysts, Appl. Surf. Sci 195 (2002) 236-250.

[13] F. Kapteljn, L. Singoredjo, A. Andreini, J.A. MouhJn, Activity and selectivity of pure manganese oxides in the selective catalytic reduction of nitric oxide with ammonia, Appl. Catal. B: Environ., 3 (1994) 173-169

[14] H.W. Nesbitt, D. Banerjee, Interpretation of XPS Mn(2p) spectra of Mn oxyhydroxides and constraints on the mechanism of MnO_2 precipitation, American Mineralogist 83 (1998) 305-315.

[15] A. A. Audi, P. M.A. Sherwood, Valence-band x-ray photoelectron spectroscopic studies of manganese and its oxides interpreted by cluster and band structure calculations, Surface and Interface Analysis 33 (2002) 274-282.

[16] F. Kapteijn, L. Songoredjo, M. Van Driel, A. Andreini, J.A. Moulijn, G. Ramis, G. Busca, Alumina-Supported Manganese Oxide Catalysts: II. Surface Characterization and Adsorption of Ammonia and Nitric Oxide, J. Catal. 150 (1994) 105

[17] X. Tang , J. Li, L. Sun, J. Hai, Origination of N_2O from NO reduction by NH_3 over -MnO_2 and -Mn_2O_3, Appl. Catal. B: Environ. 99 (2010) 156-162

[18] R. Jin, Y. Liu, Z. Wu, H. Wang, T. Gu, Relationship between SO2 poisoning effects and reaction temperature for selective catalytic reduction of NO over Mn–Ce/TiO_2 catalyst, Catal. Today 153 (2010) 84–89

[19] X.F. Tang, Y.G. Li, X.M. Huang, Y.D. Xu, H.Q. Zhu, J.G. Wang, W.J. Shen, MnO_x–CeO_2 mixed oxide catalysts for complete oxidation of formaldehyde: Effect of preparation method and calcination temperature, Appl. Catal., B: Environ. 62 (2006) 265–273.

[20] B. Murugan, A.V. Ramaswamy, D. Srinivas, C.S. Gopinath, V. Ramaswamy, Nature of Manganese Species in Ce_{1-x} $MnxO_{2-\delta}$ Solid Solutions Synthesized by the Solution Combustion Route, Chem. Mater. 17 (2005) 3983–3993.

[21] L.M. Shi, W. Chu, F.F. Qu, S.H. Luo, Preparation and evaluation of MnO_x-CeO_2 nanospheres via a supercritical anti-solvent process, Catal. Lett. 113 (2007) 59–64.

[22] S. Andreoli, F.A. Deorsola, C. Galletti, R. Pirone, Nanostructured MnO_x catalysts for low-temperature NO_x SCR, Chem. Eng. J. 278 (2015) 174–182

[23] H. Chen, A. Sayari, A. Adnot, F. Larachi, Composition–activity effects of Mn–Ce–O composites on phenol catalytic wet oxidation Appl. Catal. B:Environ. 32 (2001) 195.

[24] H. Li, G. Lu, Q. Dai, Y. Wang, Y. Guo, Y. Guo, "Efficient low-temperature catalytic combustion of trichloroethylene over flower-like mesoporous Mn-doped CeO_2 microspheres" , Ap. Cat. B: Environmental 102 (2011) 475-483

[25] S.T. Hussain, A. Sayari, F.Larachi "Enhancing the stability of Mn–Ce–O WETOX catalysts using potassium" Applied Catalysis B: Environmental 34 (2001) 1–9

[26] D. Jiang, M. Zhang, G. Li, H. Jiang , Preparation and evaluation of MnO_x–CeO_2 nanospheres via a green route Catalysis Communications 17 (2012) 59–63

[27] W. Xingyi , K. Qian, L.Dao "Catalytic combustion of chlorobenzene over MnO_x–CeO_2 mixed oxide catalysts" Applied Catalysis B: Environmental 86 (2009) 166–175

[28] M. Kang, E.D. Park, J.M. Kim, J.E. Yie, Manganese oxide catalysts for NO_x reduction with NH_3 at low temperatures, Appl. Catal. A: Gen. 327 (2007) 261-269.

[29] L.Q. Jing, Z.L. Xu, X.J. Sun, J. Shang, W.M. Cai, Relationships of surface oxygen vacancies with photoluminescence and photocatalytic performance of ZnO nanoparticles, Appl. Surf. Sci. 180 (2001) 308-314.

[30] H.W. Nesbitt, D. Banerjee, H.W. Nesbitt, D. Banerjee, Ame. Mineral. Interpretation of XPS Mn(2p) .Ame. Mineral. 83 (1998) 305-315.

[31] A.A. Audi, P.M.A. Sherwood, Valence-band x-ray photoelectron spectroscopic studies of manganese and its oxides interpreted by cluster and structure calculations.,Surf. Interface Anal. 33 (2002) 274-282.

[32] T. Yamashita, A. Vannice, Temperature-programmed desorption of NO adsorbed on Mn_2O_3 and Mn_3O_4, Appl. Catal.B: Environ. 13 (1997) 141-155

[33] X. Gao, Y. Jiang, Y. Zhong, Z.Y. Luo, K.F. Cen, J. Hazard. Preparation of Mn-Based Selective Catalytic Reduction Catalysts by Three Methods and Optimization of Process Conditions, Mater. 174 (2010) 734-739.

[34] Z. Liu, Y. Yi, S. Zhang, T. Zhu, J. Zhu, J. Wang, Ceria-based catalysts for low-temperature selective catalytic reduction of NO with NH_3, Catal. Today 216 (2013) 76–81.

[35] X. Wang, Y. Zheng, J. Lin, Low- temperature NO reduction with NH_3 over Mn-CeO_x/CNT catalysts prepared by liquid- phase method, Catal. Commun. 37 (2013) 96–99.

[36] T. Yamashita, A. Vannice, Temperature-programmed desorption of NO adsorbed on Mn_2O_3 and Mn_3O_4,Appl. Catal.B: Environ. 13 (1997) 141-155

[37] Y. Su, B. Fan, L. Wang, Y. Liu, B. Huang, M. Fu, L. Chen, D. Ye, MnO_x supported on carbon nanotubes by different methods for SCR of NO with NH_3, Catal. Today 201(2013) 115–121.

[38] X. Tang, J. Hao, W. Xu, J. Li, Low temperature selective catalytic reduction of NOx with NH_3 over amorphous MnO_x catalyst prepared with three methods, Catal. Commun. 8 (2007) 329–334.

[39] A. Sultana, M. Sasaki, H. Hamada, Influence of support on the activity of Mn supported catalysts for SCR of NO with ammonia Catal. Today 185 (2012) 284–289.

Chapter IV: Catalyst for prevention of NO_x formation

4.1 CATALYSTS

4.1.1 Catalyst preparation

On the basis of the literature survey illustrated in section 1.3.2.2, a certain number of catalysts based on non-noble metals supported on alumino-silicates was selected and developed. Further details, such as quality and quantity of the active phase and support, can not be provided since this research activity is part of a project with a company.

The synthesis method chosen for oxidant catalyst is Incipient Wetness Impregnation in aqueous solution. The procedure consisted in the previous preparation of an aqueous solution by mixing a suitable amount of metal nitrate and 50 ml of DI water. Subsequently 1g of the support powder was added to the solution and the suspension was stirred at 90 °C until complete evaporation of the water. The remaining solid was dried at 100 °C overnight and calcined at 550 °C for 5 h [1,2]. Samples were called by the letters of the alphabet.

4.1.2 Catalysts synthesis and chemical–physical characterization

Table 4.1: Values of the BET surfaces area and from XRD of the synthesized samples.

Samples	BET SSA [m^2/g]
A	256
B	542
C	120
D	495
E	486
F	509
G	463
H	401

As reported in Table 4.1, it is evident that sample C presented the lowest BET surface value (120 m^2/g), the sample A a specific surface area double than C (256 m^2/g) and the other catalysts showed similar values, in the range 400-540 m^2/g.

4.1.3 Catalytic activity measurement on powder samples

4.1.3.1 Oxidation of ammonia (inorganic molecule model for nitrogen in the reduced state)

The catalysts were tested with a mixture of ammonia, oxygen and helium according to the compositions in Table 2.8.

The ammonia was used as template molecule (Lewis base) to test the acidic properties of the catalysts, which can play a beneficial action (cooperative effect) on the catalytic activity of the redox catalysts.

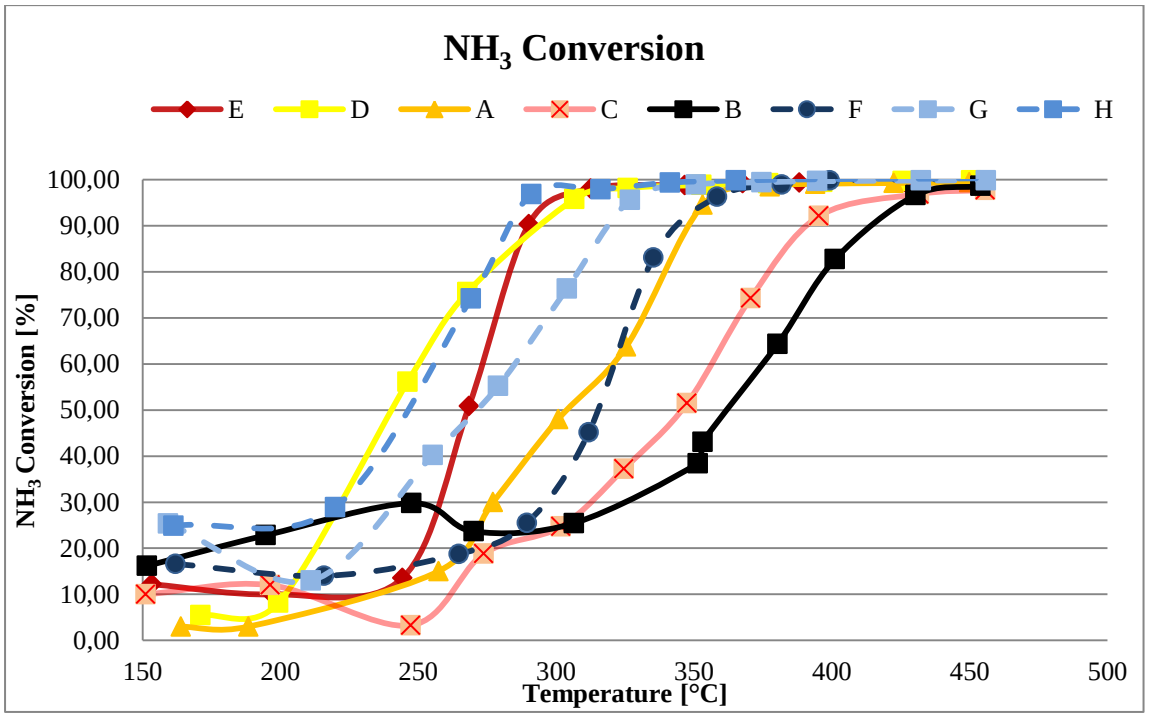

Fig. 4.1: Conversion of ammonia for catalysts developed.

All samples tested reached a conversion equal to 100%. The samples reached the complete conversion according to the following order of increasing temperature: H < E < D < G < A < F < C < B.

The selectivity to nitrogen was calculated to check how much ammonia oxidized was actually converted to nitrogen and how many unwanted products, such as NO_x (NO, NO_2) and N_2O, were generated.

The selectivity was evaluated as:

N_2 selectivity (%) $S = \frac{C_{N2}}{C_{N2}+C_{N2O}} \cdot 100\%$

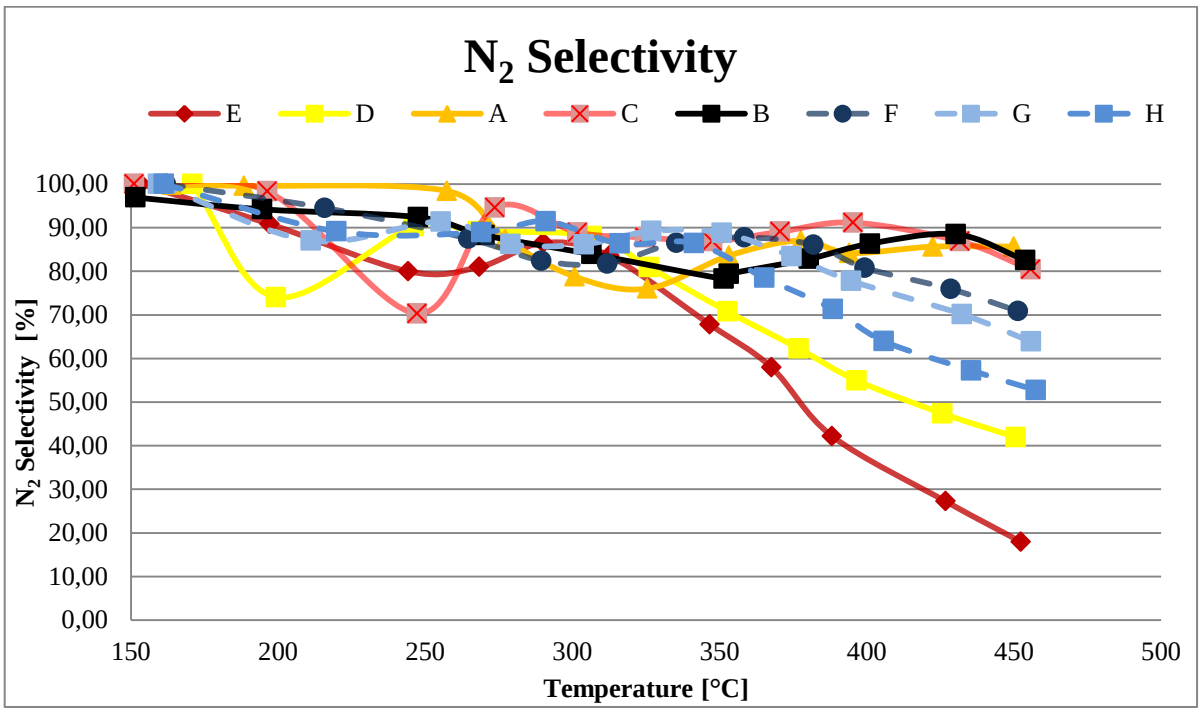

Fig. 4.2: Chart selectivity to N_2 vs temperature for the catalysts developed.

It can be noted that the samples with the blue lines (F, G and H) maintained a high selectivity by increasing the temperature, while some catalysts, such as E, showed a greater reduction.

At the temperature of 425 °C, which is a typical temperature of the outlet exhaust gases, the yield is high for the catalysts A, B and C, with values always higher than 80% as reported in Table 4.2.

Table 4.2: Values of the Yield for the best performer samples

Samples	Yield [%]
A	85
B	85,48
C	84,15

4.1.3.2 Oxidation of carbon monoxide

All the samples synthesized and characterized were tested to evaluate the conversion of carbon monoxide to carbon dioxide under the conditions described in Table 2.9.

The reaction is evaluated as follows:

$$CO + \frac{1}{2}O_2 \rightarrow CO_2$$

During the temperature ramp, under continuous flow of the mixture, all the catalysts, except A and B, following a sigmoidal trend reaching 100% of conversion of CO to CO_2.

So, for most of the catalysts tested the conversion was constant and complete in the desired range of temperatures (400-450 °C).

The catalysts reported with the blue lines also showed a higher conversion at lower temperature and constantly complete at high temperature.

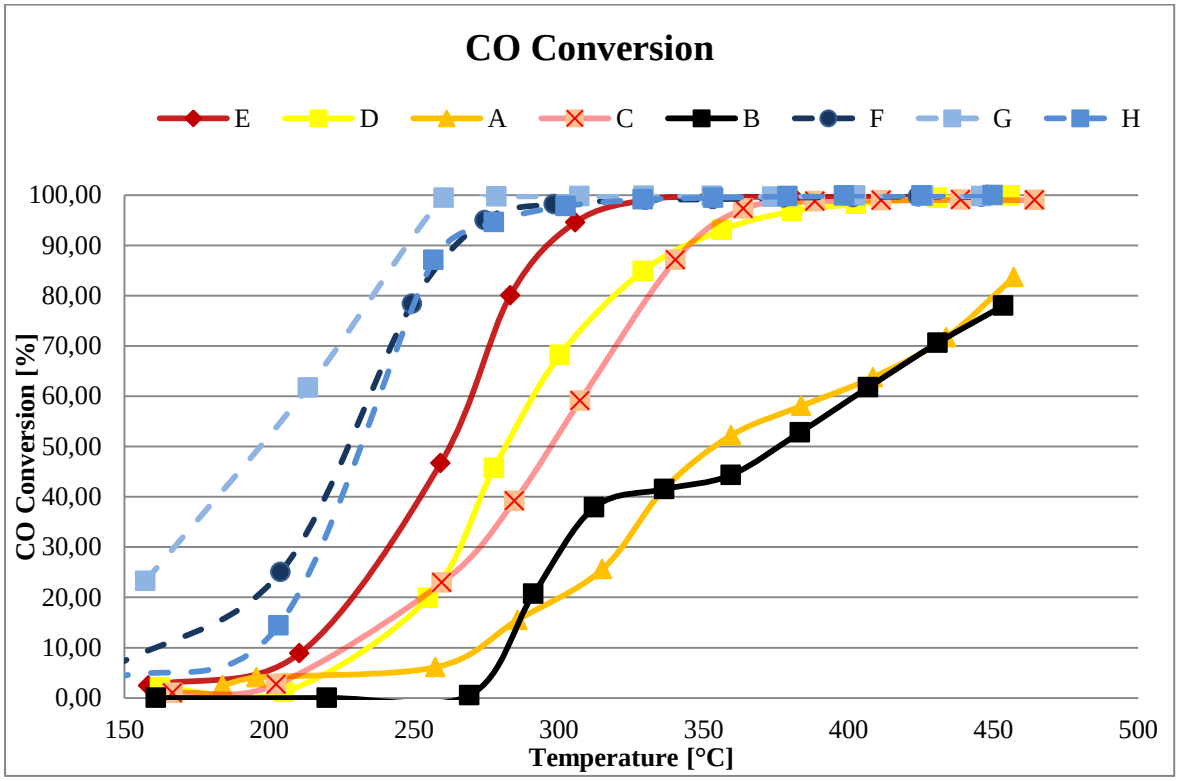

Fig. 4.3: Conversion of CO of the catalysts developed.

4.1.3.3 Oxidation of ethylene, propylene, toluene (VOC model molecules)

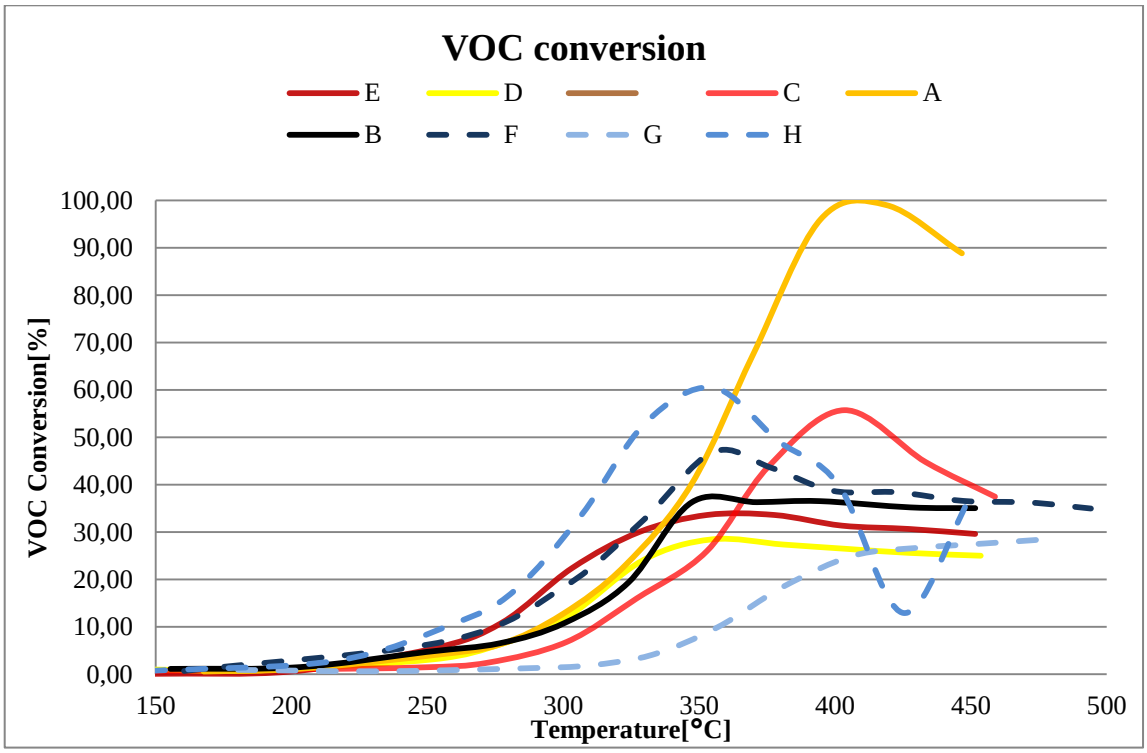

Fig. 4.4: Conversion of CO of the catalysts developed.

The mixture used for the test was made, in terms of concentration, of 1/3 of propylene, 1/3 toluene, and 1/3 of ethylene (Fig.4.4).

This complex mixture is representative of VOC that must be removed by the oxidation catalysts.

The oxidation reactions of the various components are the following compounds:

$$C_2H_4 + 3O_2 \rightarrow 2CO_2 + 2H_2O$$

$$C_7H_8 + 9O_2 \rightarrow 7CO_2 + 4H_2O$$

$$2C_3H_6 + 9O_2 \rightarrow 6CO_2 + 6H_2O$$

As a result, the conversion is so calculated as:

$$Conversion\ (\%) = \frac{F_{co2}}{\nu F_{VOCin}} x100$$

in which $F_{VOC,\ in}$ is the molar flow rate of VOC input, F_{CO2} is the molar flow at the outlet of CO_2 in stationary conditions and ν is the number of carbon atoms in the VOC (to ethylene, propylene, toluene and the mixture = 2, 3, 7 respectively, then 12 total).

As illustrated in Fig.4.4, the only sample that reached the VOC conversions higher than 90% VOC to CO_2 was sample A.

The reaction is supposed to be the following:

$$C_2H_4 + 3O_2 \rightarrow 2CO_2 + 2H_2O$$

Ethylene is the volatile organic compound in which the bonds are more difficult to break during the oxidation reaction. For this reason, the same catalysts were investigated for the oxidation of the ethylene single molecule.

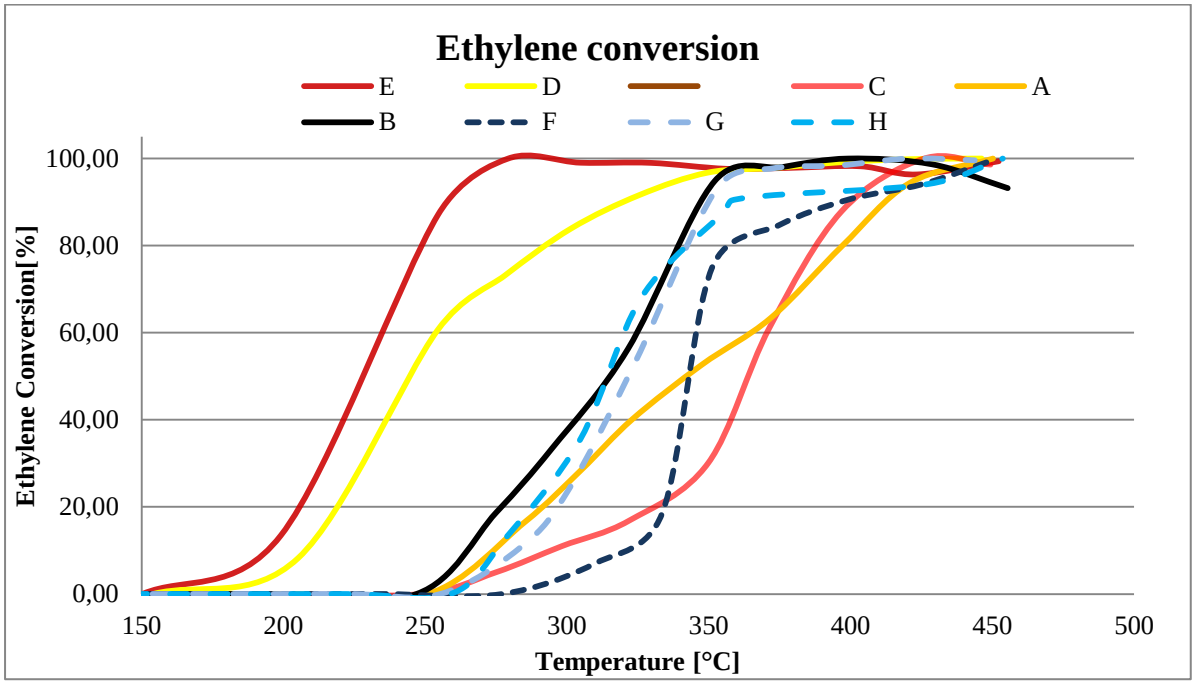

Fig. 4.5: Conversion of ethylene of the catalysts developed.

As illustrated in Fig. 4.5, all the samples reach the total conversion to CO_2. The catalysts that reached the 100% conversion at a lower temperature are E and D.

4.1.3.4 Oxidation of the complete mixture of model molecules

In the following figures the catalysts have been described and considered individually in order to evaluate the effects of all the components of the mixture and the capacity and selectivity of various catalysts.

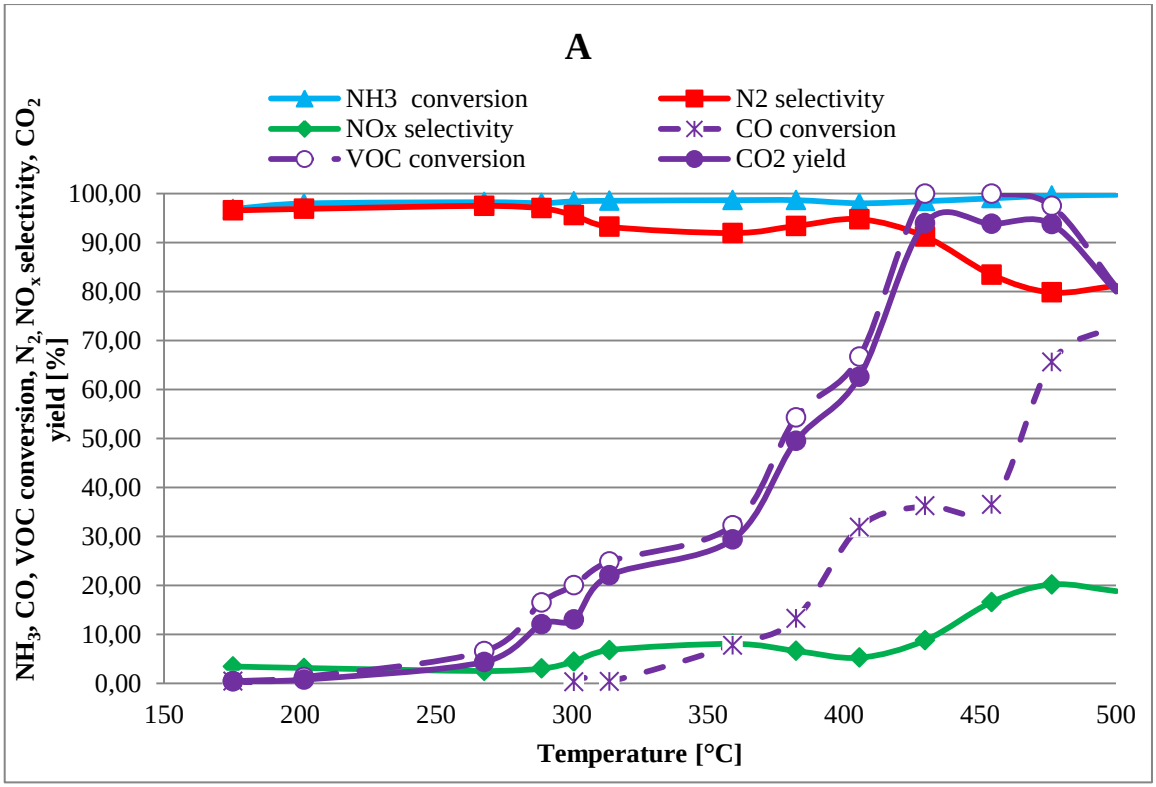

Fig. 4.6: NH_3, CO, VOC conversion, N_2 and NO_x selectivity and CO_2 yield of sample A.

Fig. 4.6 shows the trend of conversion, selectivity and yield of the various gases involved for the catalyst A.

The catalyst improved the performance of both low and high temperature; in fact, the ammonia was converted almost completely at low temperature and the selectivity had a towards nitrogen which followed the same trend.

Nitrogen oxides were formed in a reduced quantity only at temperatures close to 500 °C.

Volatile organic compounds were converted completely between 400-450 °C while achieving maximum conversion of carbon monoxide at a higher temperature, but the yield carbon dioxide reached 100%.

Therefore, this catalyst allowed to selectively oxidize all the gases present in the mixture and allows discrete yields and selectivity in the temperature range of interest. [1, 4-6]

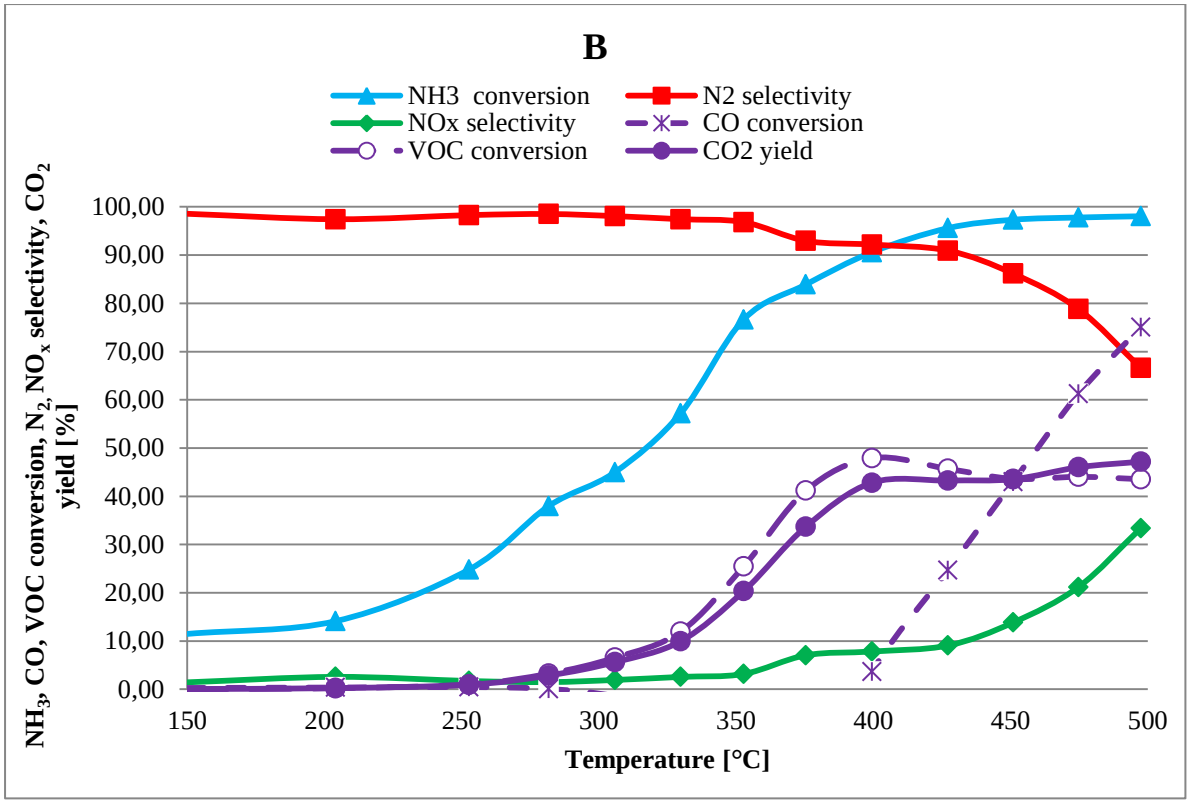

Fig. 4.7: NH_3, CO, VOC conversion, N_2 and NO_x selectivity and CO_2 yield of sample B.

As illustrated in Fig. 4.7, the sample B had a high selectivity towards nitrogen (above 80% up to 450 °C), similar to the samples A and C. Even the trend of conversion of ammonia was coincident with the latter sample, although the surface area of the sample A. The conversion of the carbon monoxide took place at high temperature while the volatile organic compounds were converted to the maximum of 30%.

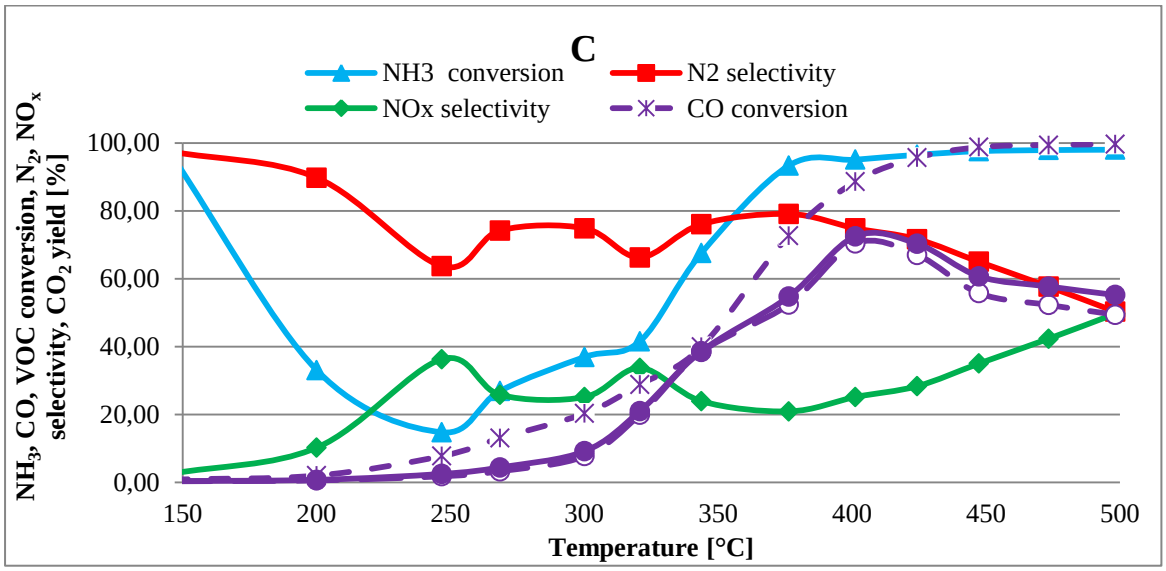

Fig. 4.8: NH_3, CO, VOC conversion, N_2 and NO_x selectivity and CO_2 yield of sample C

The sample C (Fig. 4.8) showed a total conversion of the ammonia at relatively high temperature (350 °C) with subsequent conversion of the carbon monoxide.
Even the conversion of VOC was relatively high and the resulting yield of carbon dioxide. The selectivity to nitrogen was moderate even at high temperatures.

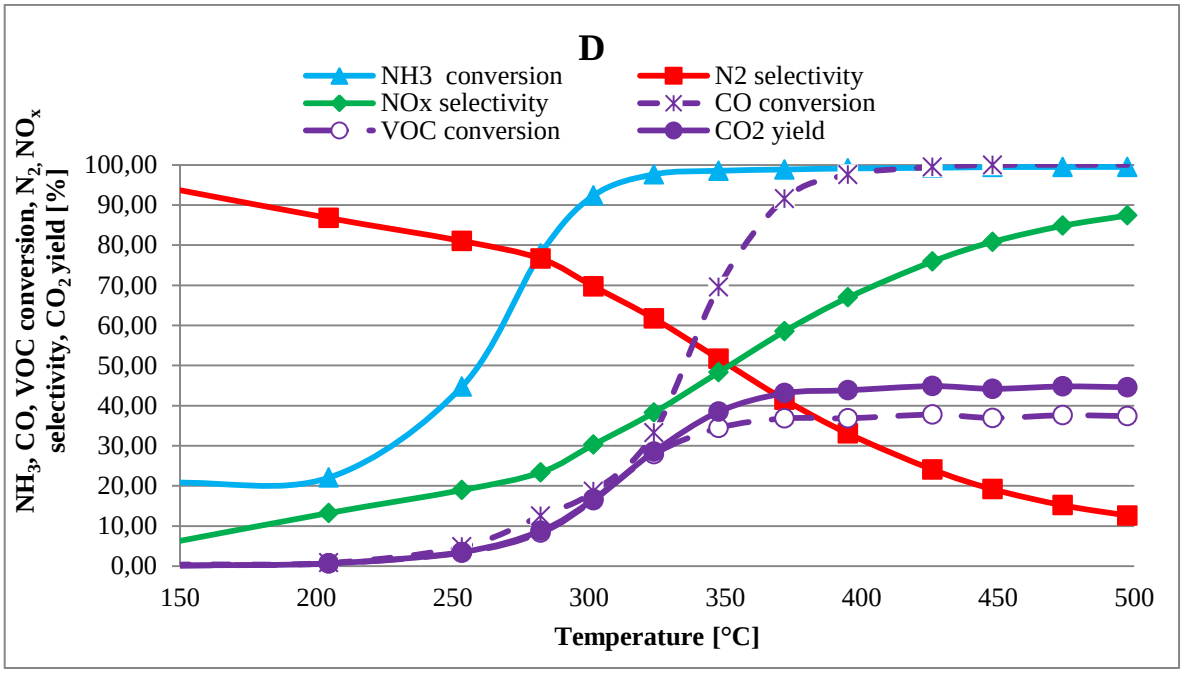

Fig. 4.9: NH_3, CO, VOC conversion, N_2 and NO_x selectivity and CO_2 yield of sample D

The graph in Fig. 4.9 highlights how ammonia reached the complete conversion at a temperature of 300 °C by employing the sample D, and also carbon monoxide was converted completely at a higher temperature of 375 °C. Volatile organic compounds reached the maximum conversion of 47% at 350 °C.
This conversion of VOC into carbon dioxide was not complete, resulting in a yield of about 38%.
The selectivity to nitrogen by reaction of selective oxidation of the ammonia decreased with increasing temperature, reaching 20% in the temperature range 400-450 °C. The cause was the unwanted formation of NO_x, mainly in the form of NO and N_2O.

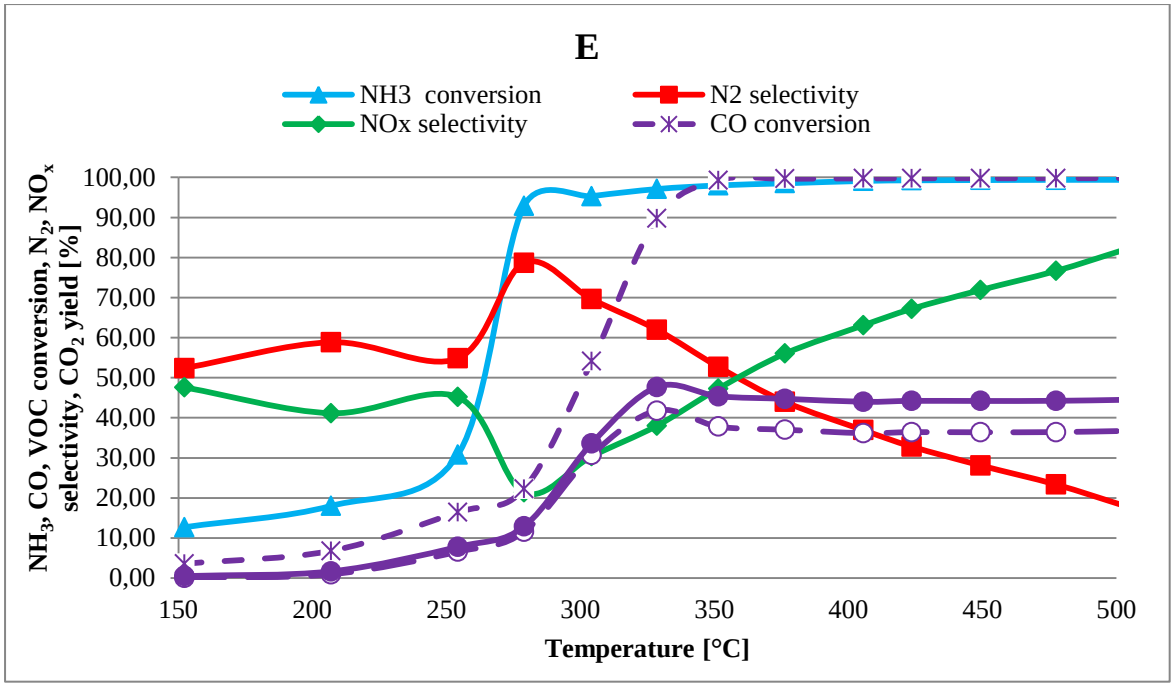

Fig. 4.10: NH_3, CO, VOC conversion, N_2 and NO_x selectivity and CO_2 yield of sample E

The catalyst with the highest percentage of non-noble metal synthesized via method IWI (sample E, see Fig. 4.10) presented the complete conversion of ammonia at a temperature lower than the catalyst D, and the selectivity to nitrogen had a decreasing trend by increasing the temperature.

The carbon monoxide reached 100% conversion at 350 °C.

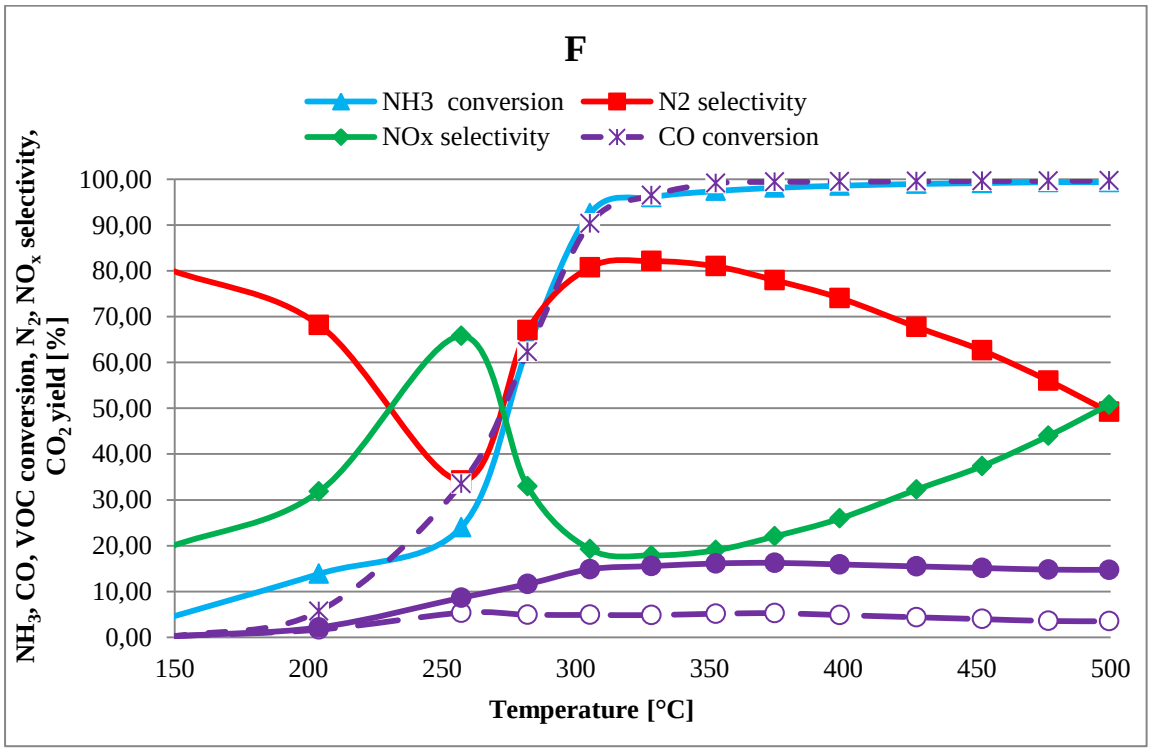

Fig. 4.11: NH_3, CO, VOC conversion, N_2 and NO_x selectivity and CO_2 yield of sample F

All samples consisting of mixed non-noble metals reached the complete conversation of NH_3 and CO at a temperature lower than the catalysts containing single non-noble metals, as evident in Fig. 4.11, 4.12 and 4.13.

The sample F reached 100% conversion of CO and NH_3 at the same temperature, while it presented a low conversion of VOC. The selectivity to nitrogen had a peak between 300 and 400 °C.

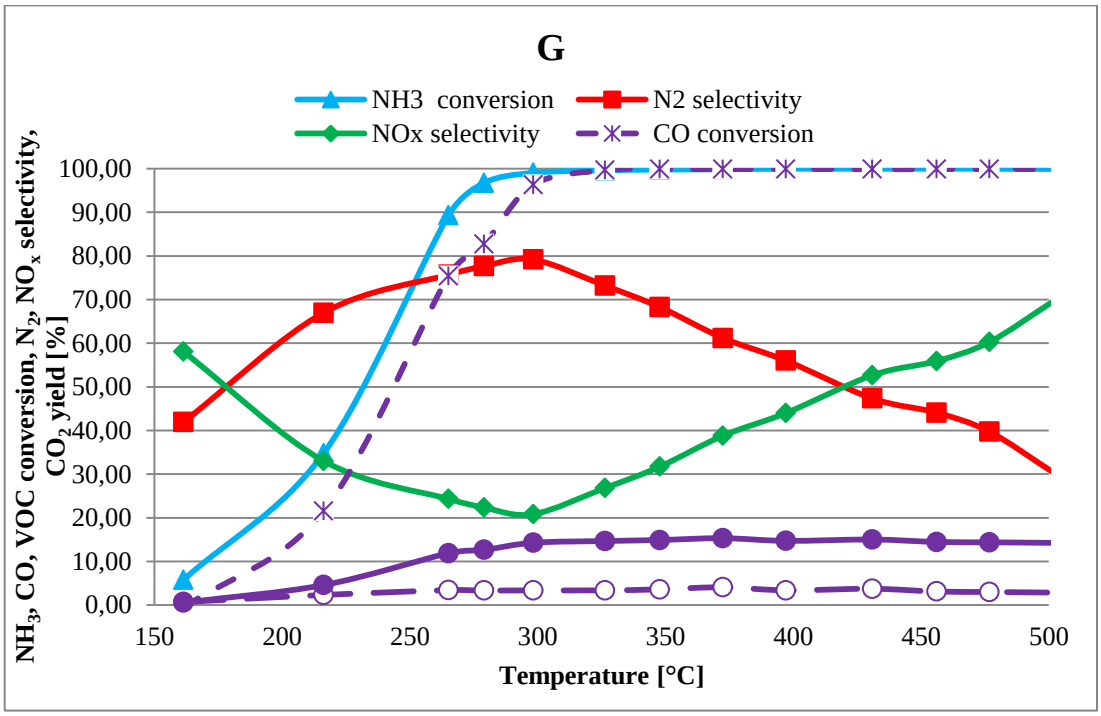

Fig. 4.12: NH_3, CO, VOC conversions, N_2 and NO_x selectivity and CO_2 yield of sample G

The catalyst G, illustrated in Fig. 4.12, had a maximum conversion of the mixture of the VOC maximum of 17%, as well as the catalysts in Figs. 4.11 and 4.13 (sample H).

The yield in CO_2 was low even if the CO conversion was total at temperatures above 300 °C.

Even the representative sigmoidal conversion of ammonia was similar to that of the sample Fig.4.13. The selectivity to nitrogen after a maximum at 300 °C decreased with increasing temperature.

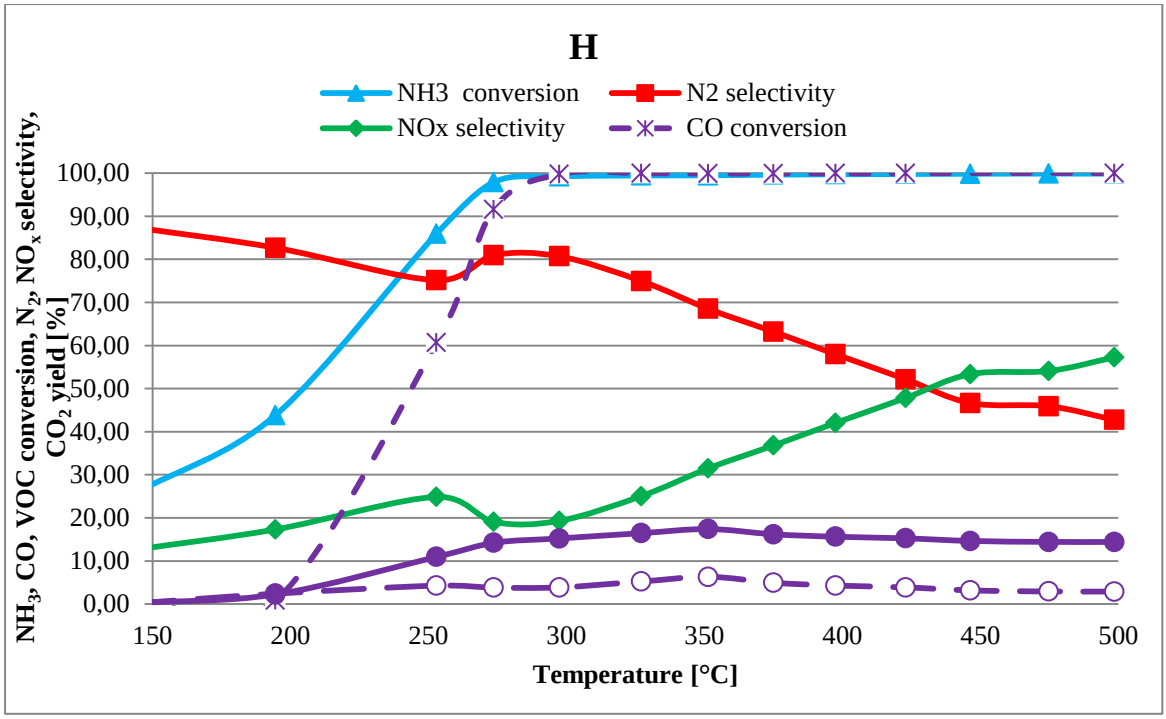

Fig. 4.13: NH_3, CO, VOC conversions, N_2 and NO_x selectivity and CO_2 yield of sample H

4.1.3.5 Oxidation of methanol (roasting probe molecule for VOC)

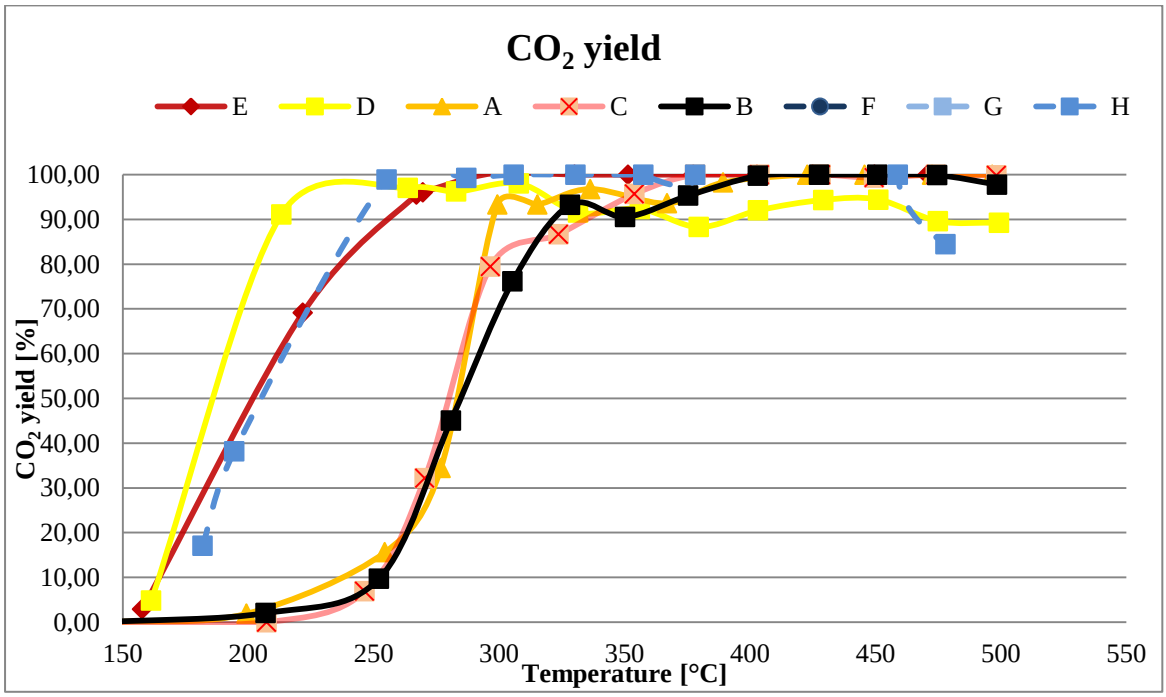

Fig. 4.14: CO_2 Yield for all the samples synthesized.

The oxidation reaction of the methanol is the following:

$$2CH_3OH + 3O_2 \rightarrow 2CO_2 + 4H_2O$$

All catalysts reached 100% conversion and this conversion was maintained by increasing temperature, except for samples D and H.

4.1.3.6 Oxidation of the pyridine (roasting probe molecule for the nitrogen in the reduced state)

The reaction considered is the following:

$$4C_5H_5N + O_2 \rightarrow 20CO_2 + 2N_2 + 10H_2O$$

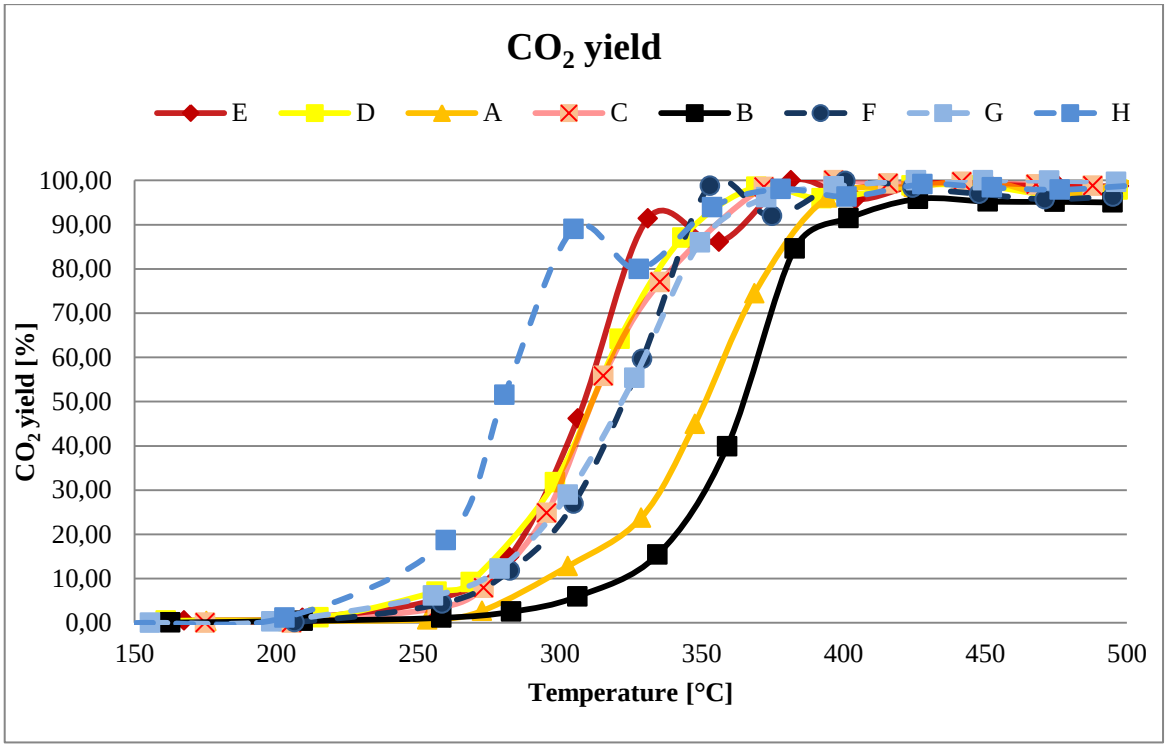

Fig. 4.15: CO_2 Yield for all the samples synthesized.

To assess the conversion of pyridine, the CO_2 yield was calculated, meaning that if the carbon present in the molecule of the pyridine was completely converted to CO_2 then the pyridine was completely converted.

For all the catalysts, as can be noticed in Fig. 4.15, a yield of carbon dioxide higher than 95% has been reached in the temperature range desired [5-7].

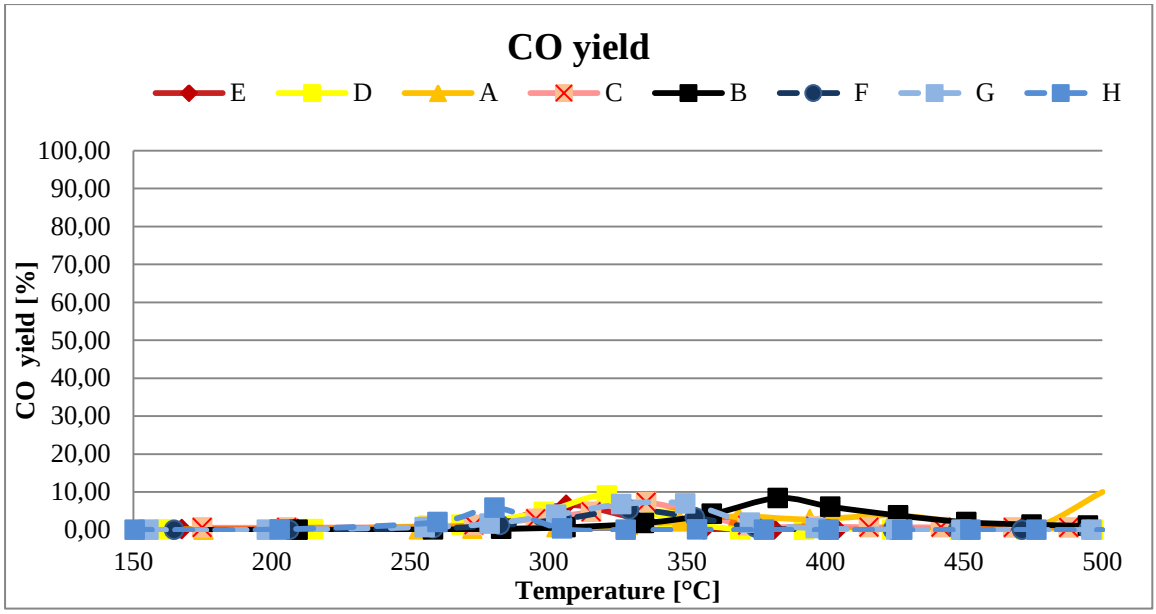

Fig. 4.16: CO yield for all the samples synthesized.

The calculation of yield was made even assuming that all the carbon is converted to CO. Given the values obtained from the tests and reported in Fig. 4.16, it become clear that the formation of CO was minimal.

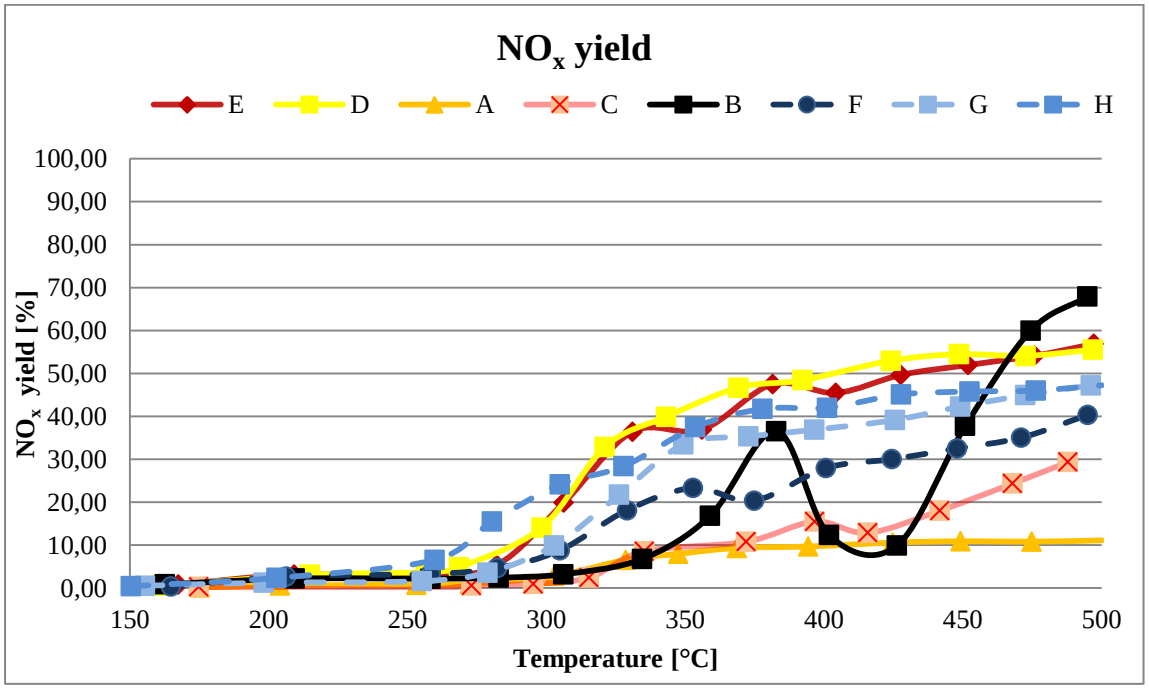

Fig. 4.17: NOx Yield for all the samples synthesized.

The yield of nitrogen oxides was analysed, and it was verified that the catalyst which produced less NO_x was sample A and it was the same that presented the best selectivity to nitrogen in the oxidation tests of the molecule sample choice for nitrogen compounds or ammonia. Samples that may be interesting in the range 400-

450 °C were also B and C. The graphs reported in Fig. 4.18 and Fig. 4.19 summarizes through histograms the results at the temperatures of 300 and 425 °C respectively. The samples that showed the best overall performance for the abatement of all the molecules testes were E and F at 300 °C and A, B and C at 425°C.

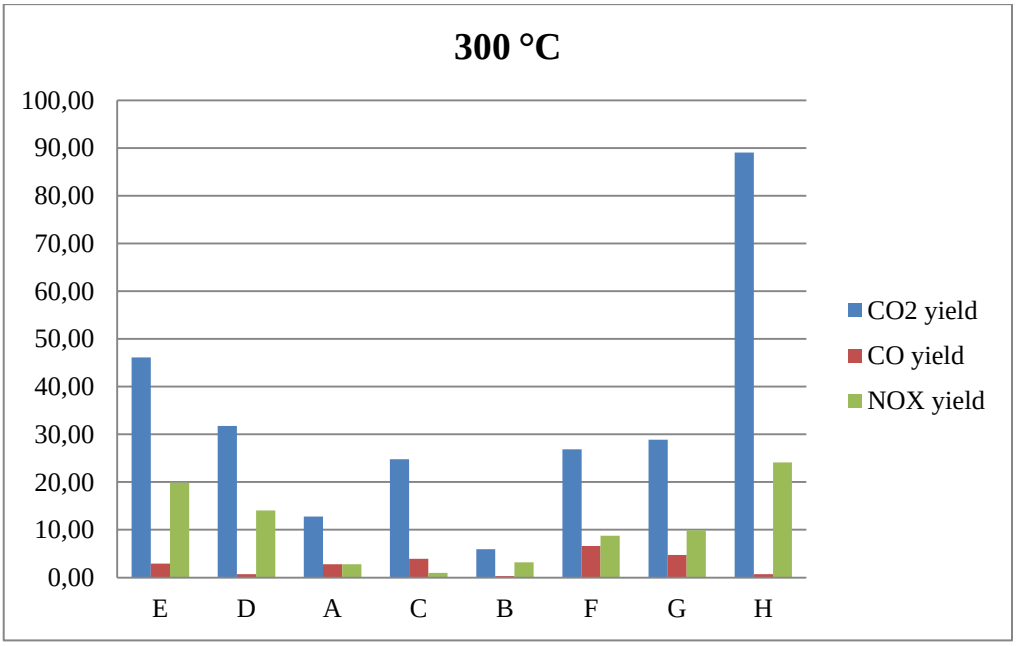

Fig. 4.18: Results at 300°C.

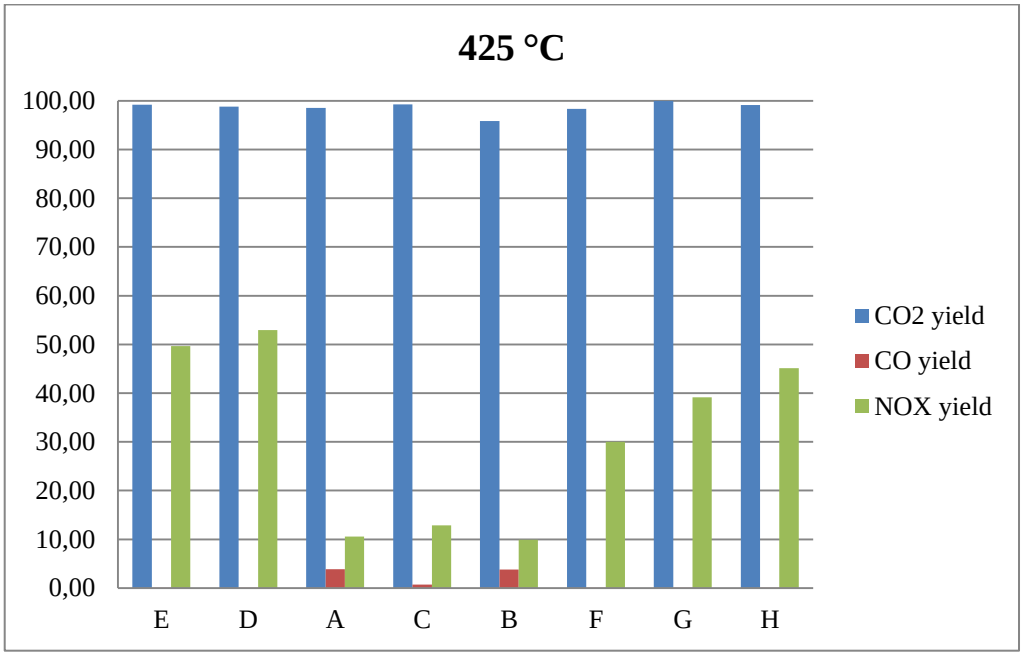

Fig. 4.19: Results at 425 °C.

4.1.3.7 Oxidation complete mixture of roasting probe molecules

In the following figures, the graphs for the comparison between A, B and C samples, that were the samples presenting the best performance, were reported. Moreover, the effect of the addition of water in the stream on the catalytic performance was evaluated. The samples were tested with the operating conditions reported in Table 2.15 with the addiction of 5% of steam water. The addition of steam has been possible through the vaporization of the water contained in a tank and vaporized due to the CEM. These tests were performed because of the presence of 12% of steam water in the real effluents. Furthermore the samples were aged at 500 °C for 72 h and 7 days in order to investigate the thermal stability of the catalysts and the possible effect on the catalytic performance.

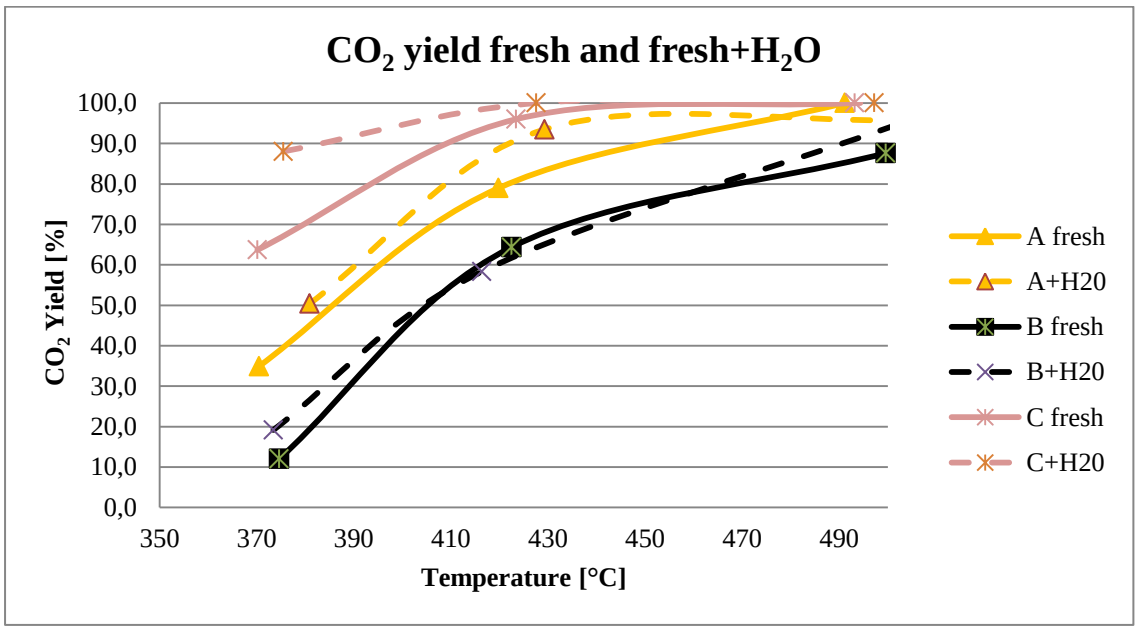

Fig. 4.20: CO_2 yield for fresh and fresh with vapour samples.

As illustrated in Fig. 4.20, all the samples incremented the CO_2 yield when 5% of water vapour was added in the flux. In addition, the NO_x yield was increased forming more undesired NO_x (see Fig. 4.21).

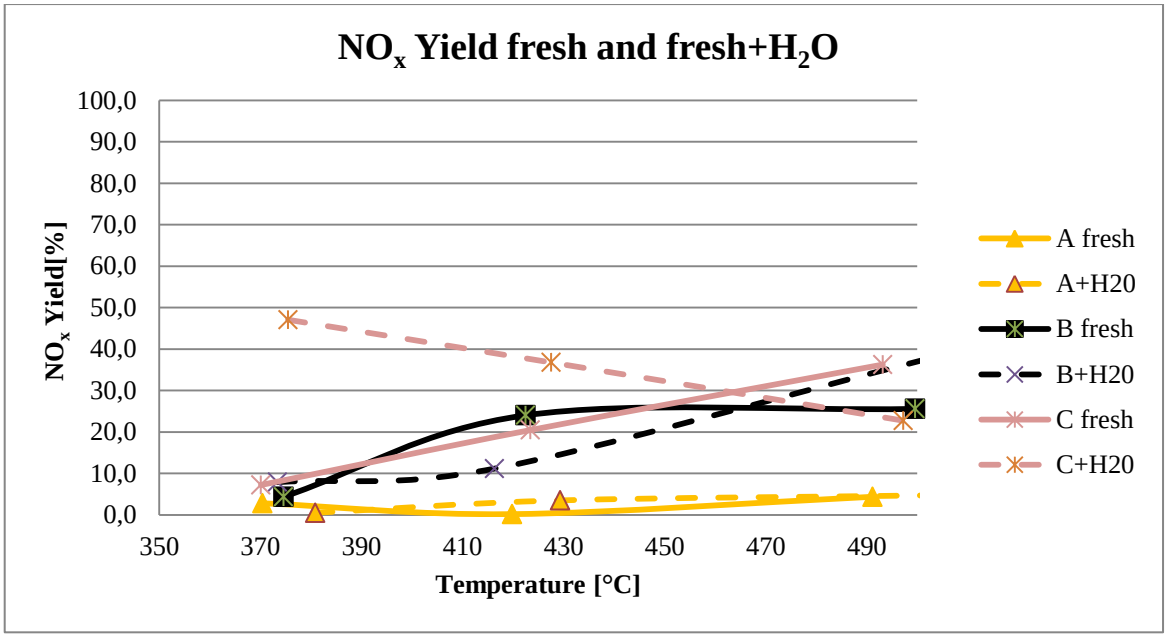

Fig. 4.21: NO_x yield for fresh and fresh with vapour samples.

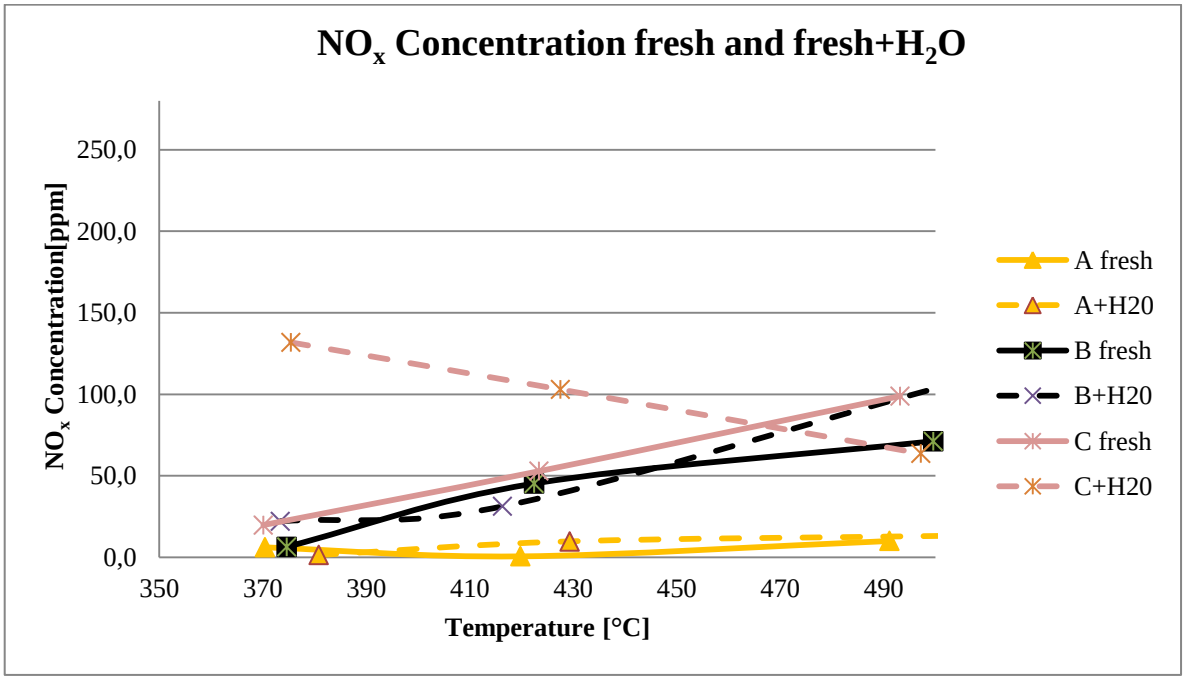

Fig. 4.22: NO_x concentrations for fresh and fresh with vapour samples.

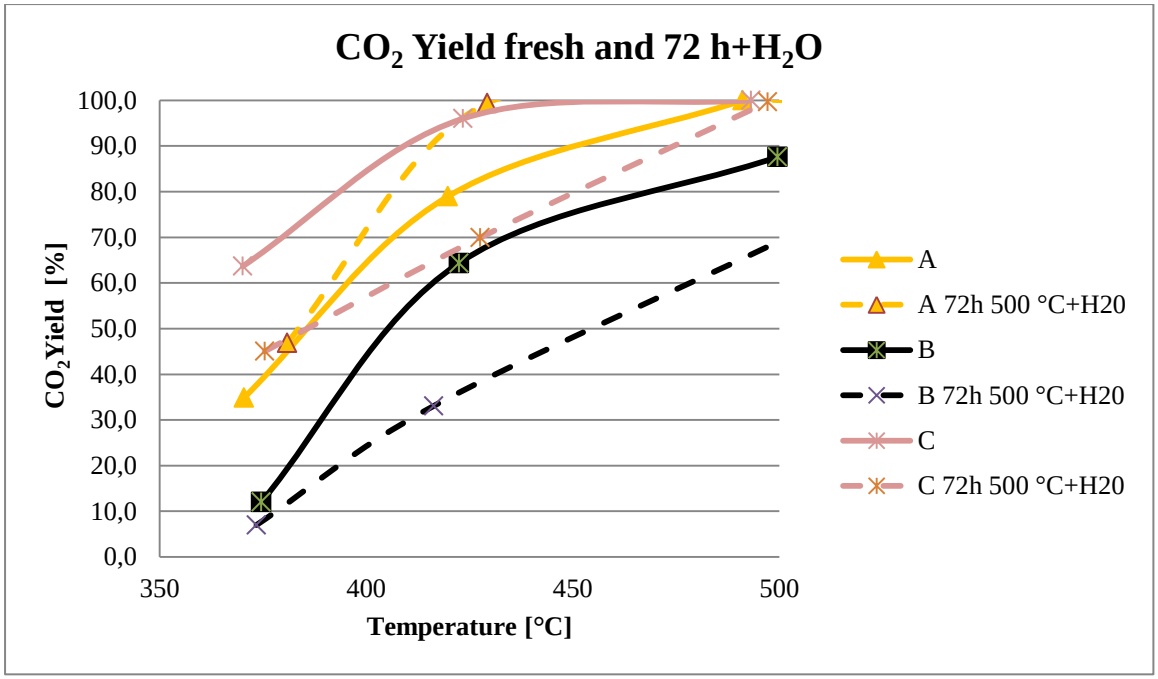

Fig. 4.23: CO_2 yield for samples for samples fresh and treated 72h with water vapour.

In Fig. 4.23, is possible to notice that for sample B and C the performance with steam water of the fresh catalyst were higher than the same samples treated for 72 h, instead the A sample had the opposite behaviour.

All the aged samples had a low NO_x yield due to the very low NO_x formation (see Fig. 4.24). The lower concentration of NO_x on the aged catalyst could be due to the stability on the catalyst surface of the nitrates species formed after NO + O_2 co-adsorption. They are highly resistant to water but easily interact with VOC compounds.

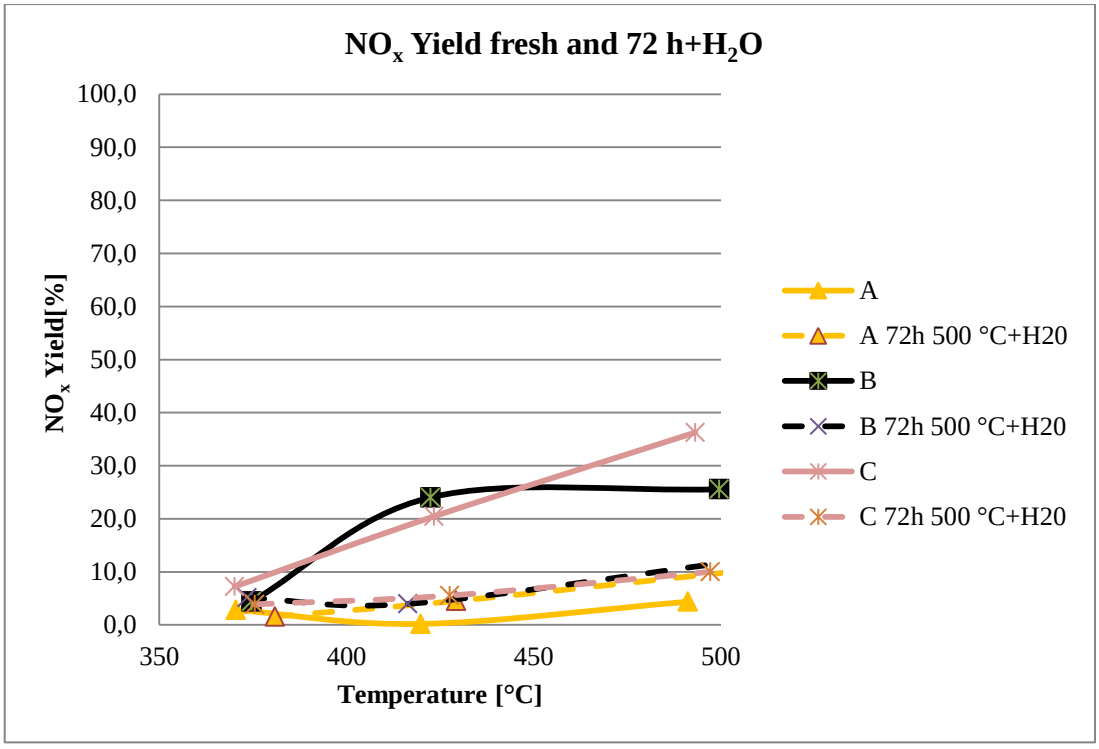

Fig. 4.24: NO_x yield for samples for samples fresh and treated 72h with water vapour.

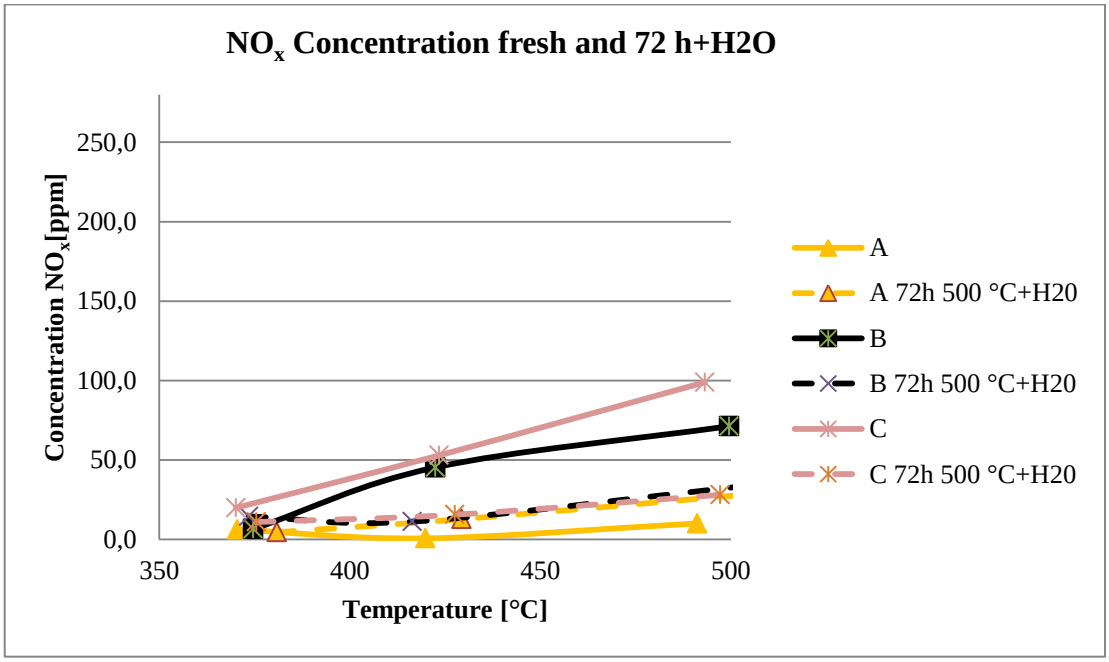

Fig. 4.25: NO_x concentrations for samples for samples fresh and treated 72h with water vapour.

The Figs. 4.26, 4.27 and 4.28 showed respectively the CO_2 yield, NO_x yield and NO_x concentration for the A, B and C samples, fresh and aged for 7 days, from the tests with the probe mixture and water vapour.

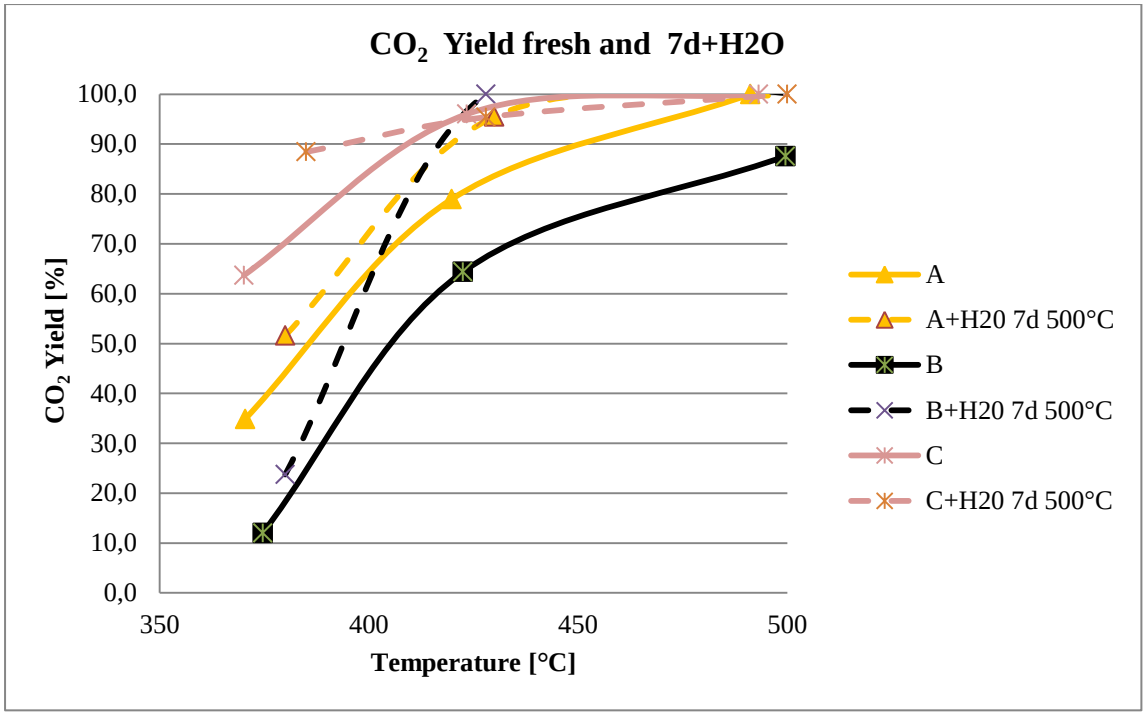

Fig. 4.26: CO_2 yield for samples for samples fresh and treated 72d with water vapour.

The samples A and B presented a higher CO_2 yield, so the conversion of the molecules was almost complete starting from 430 °C. The sample C maintained almost the same trend in the case of fresh or treated samples. All samples produced, after thermal treatment, more NO_x, as reported by a higher NO_x yield in Figs. 4.27 and 4.28.

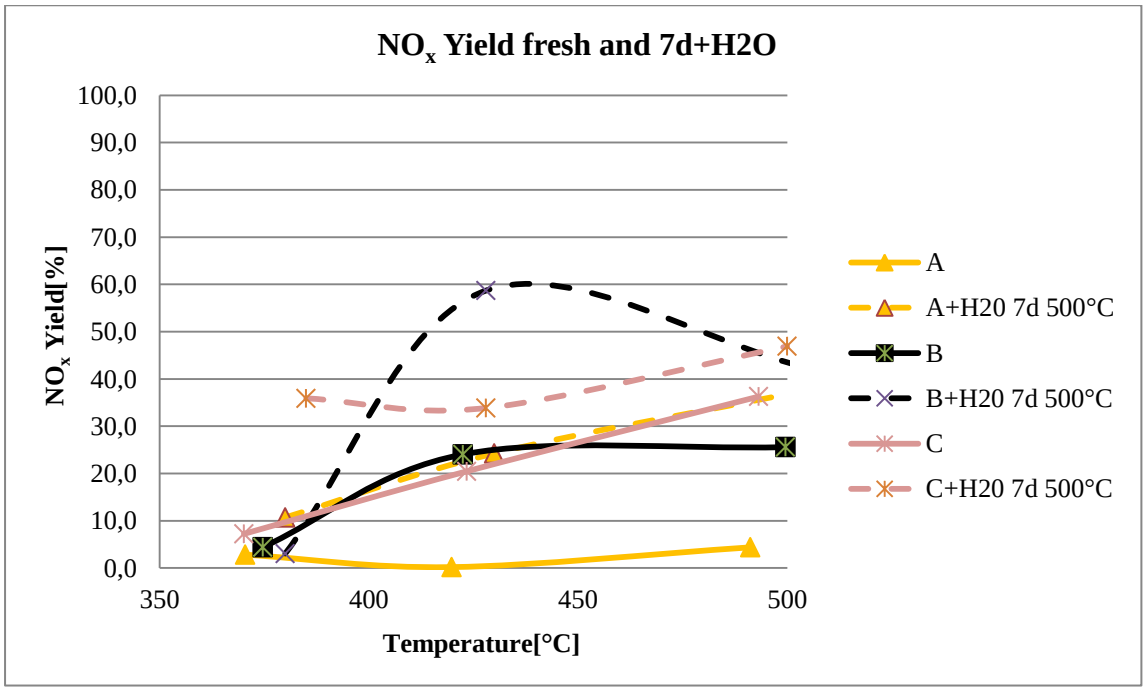

Fig. 4.27: NO_x yield for samples for samples fresh and treated 72d with water vapour.

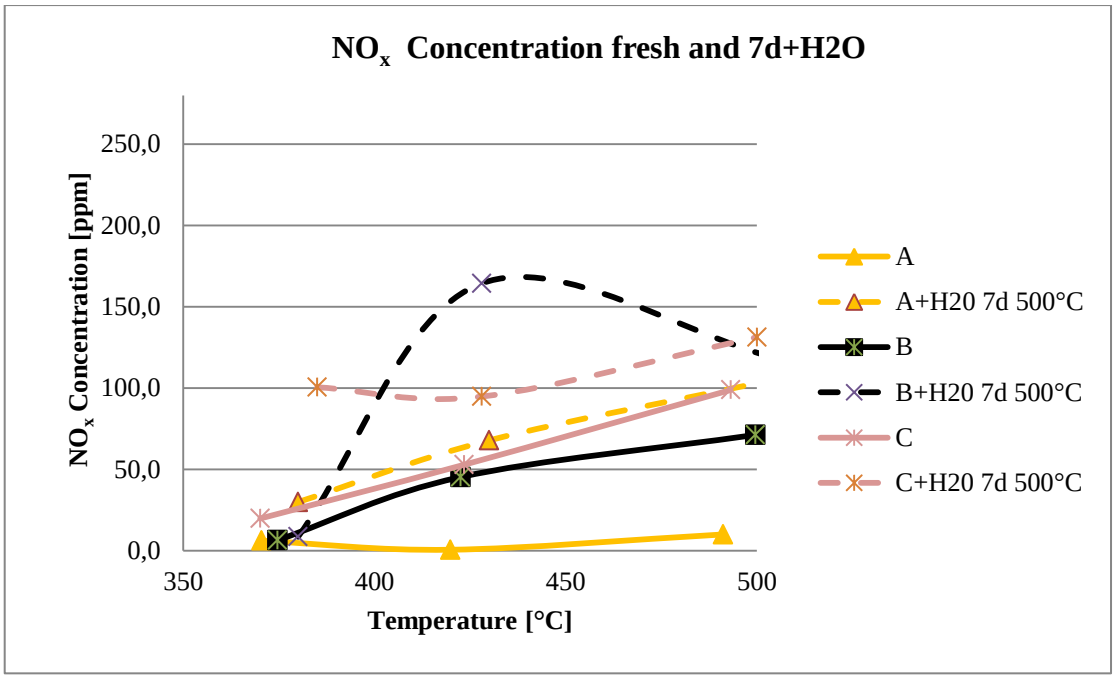

Fig. 4.28: NO_x concentrations for samples for samples fresh and treated 72d with water vapour.

4.1.4 Catalytic activity measurement on structured catalysts developed

In heterogeneous catalysis with gaseous molecules, catalysts are structured on monoliths since by this way a suitable surface for keeping in contact the gas with the active elements is provided.

So selected monoliths were impregnated with the powder of the catalyst A and C developed.

Only catalyst A and C were chosen due to the higher performance observed in the test above.

The Figs. 4.29-4.32 report the results obtained with the samples A and C deposited on a small monolith with dimensions: 0, 6x0, 6x1, 1, 6 cm.

The total flow was equal to the tests on powders, since ensuring the same GHSV, and the working conditions were the ones reported in Table 2.15 with the addiction of 5% of steam water.

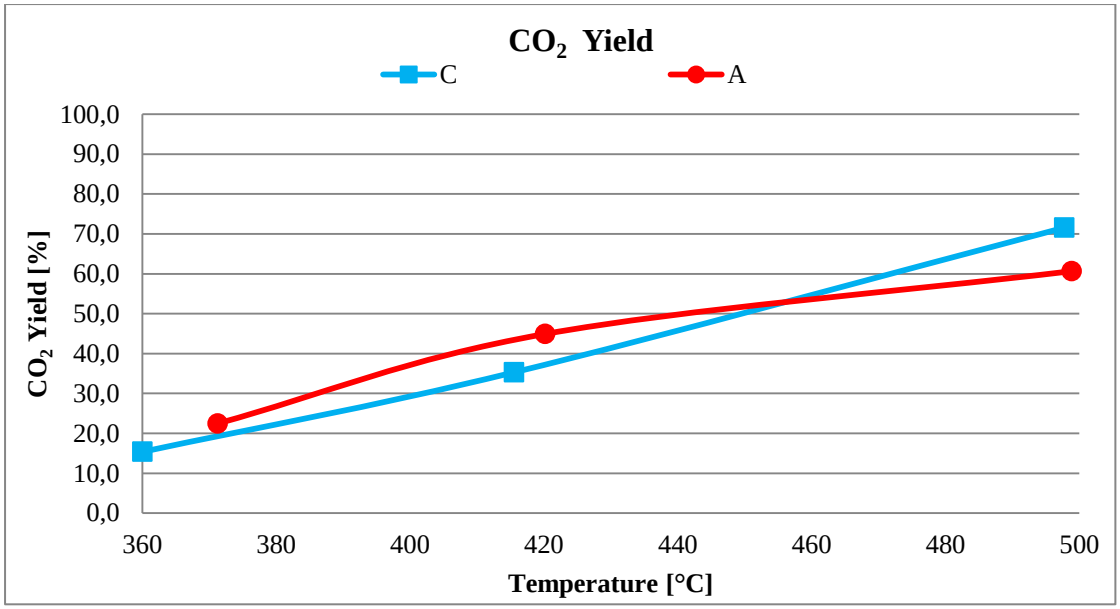

Fig. 4.29: CO_2 yield for samples A and C.

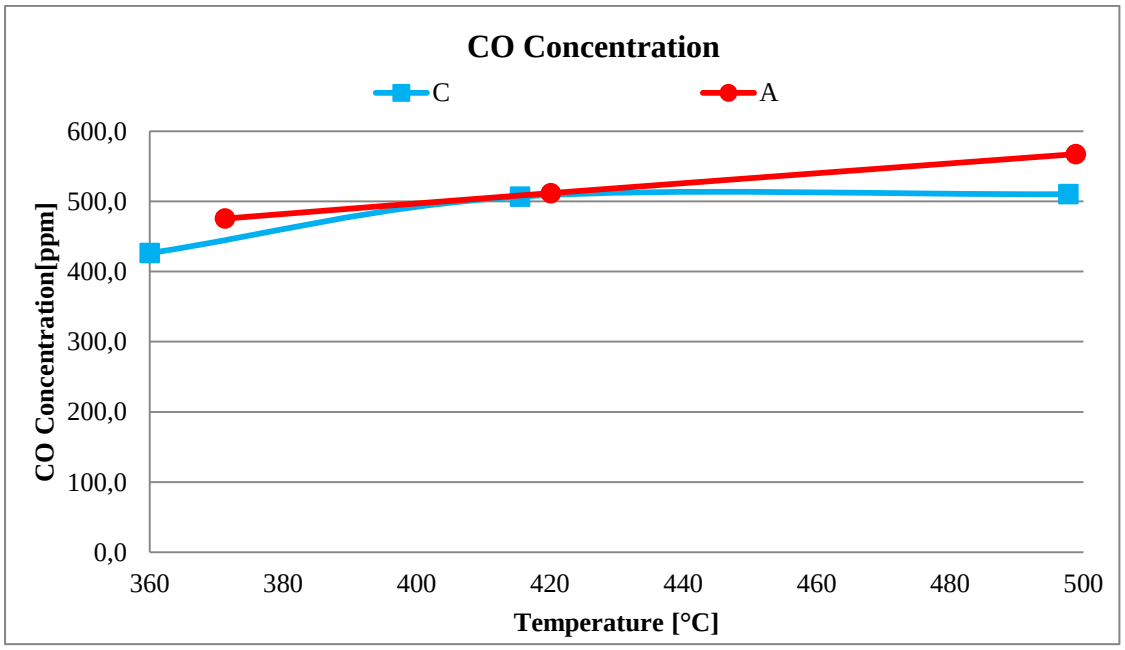

Fig. 4.30: CO concentration for samples A and C.

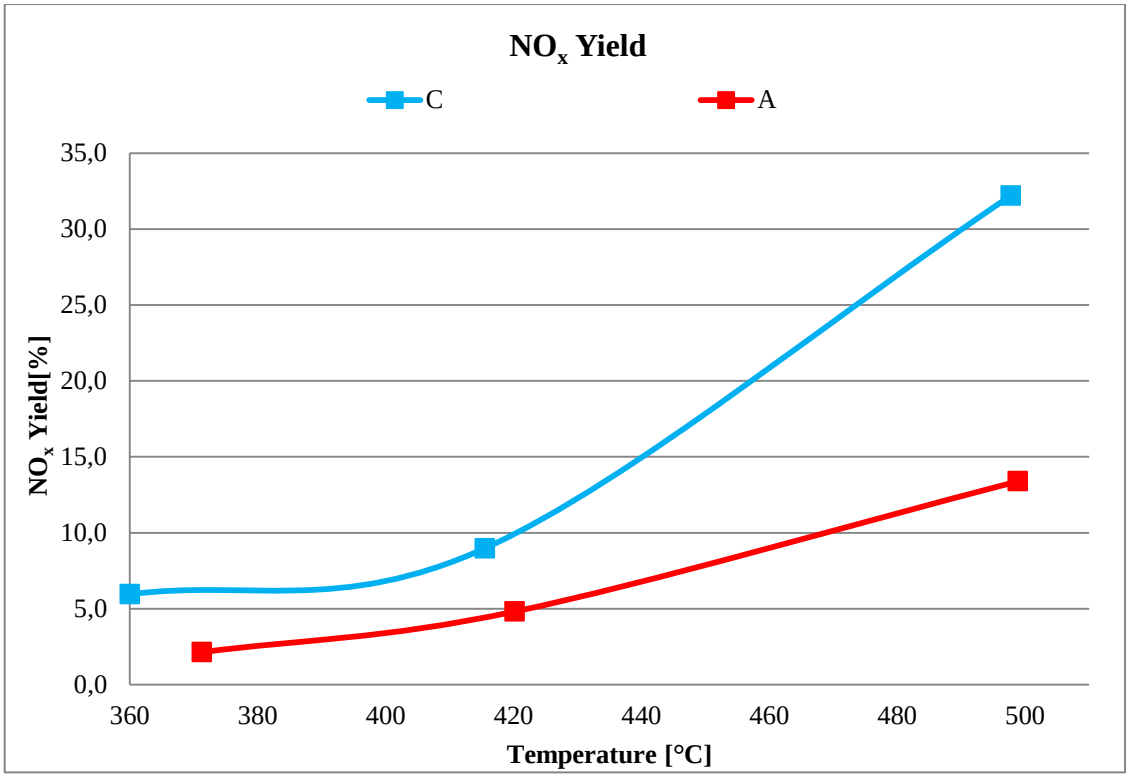

Fig. 4.31: NO_x yield for samples A and C.

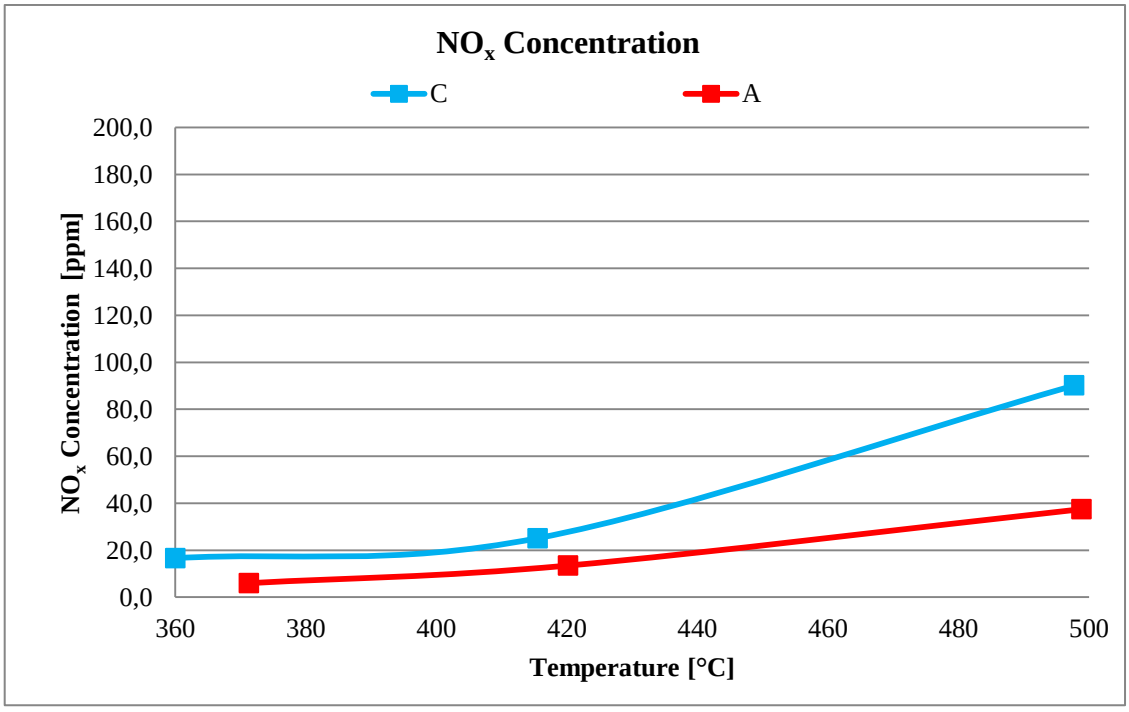

Fig. 4.32: NO_x concentration for samples A and C.

Samples A and C had almost the same trend for CO_2 yield and CO concentration but sample C showed higher NO_x yield and concentration.

So the tests development focused the attention only on the A sample. In Figs. 4.33, 4.34 and 4.35 the concentrations of CO_2, CO and NO_x at different space velocities

(50000 and 10000 h^{-1}) and different working time (durability test for 24 h at 10000 h^{-1}, performed in 3 steps of 8 hours each step) are reported.

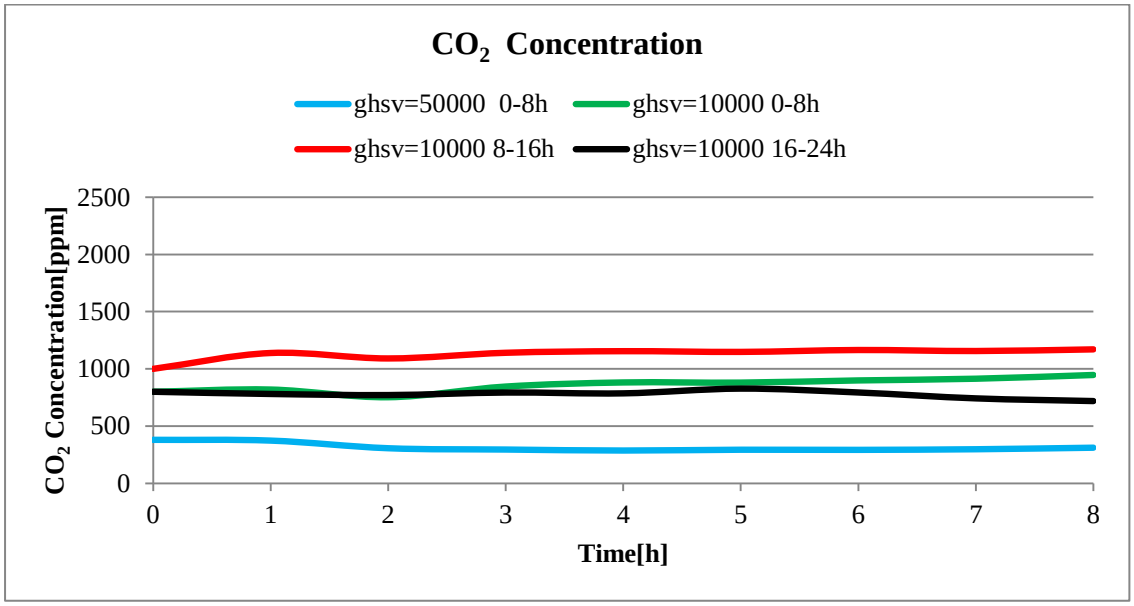

Fig. 4.33: CO_2 concentration for samples A at different GHSV.

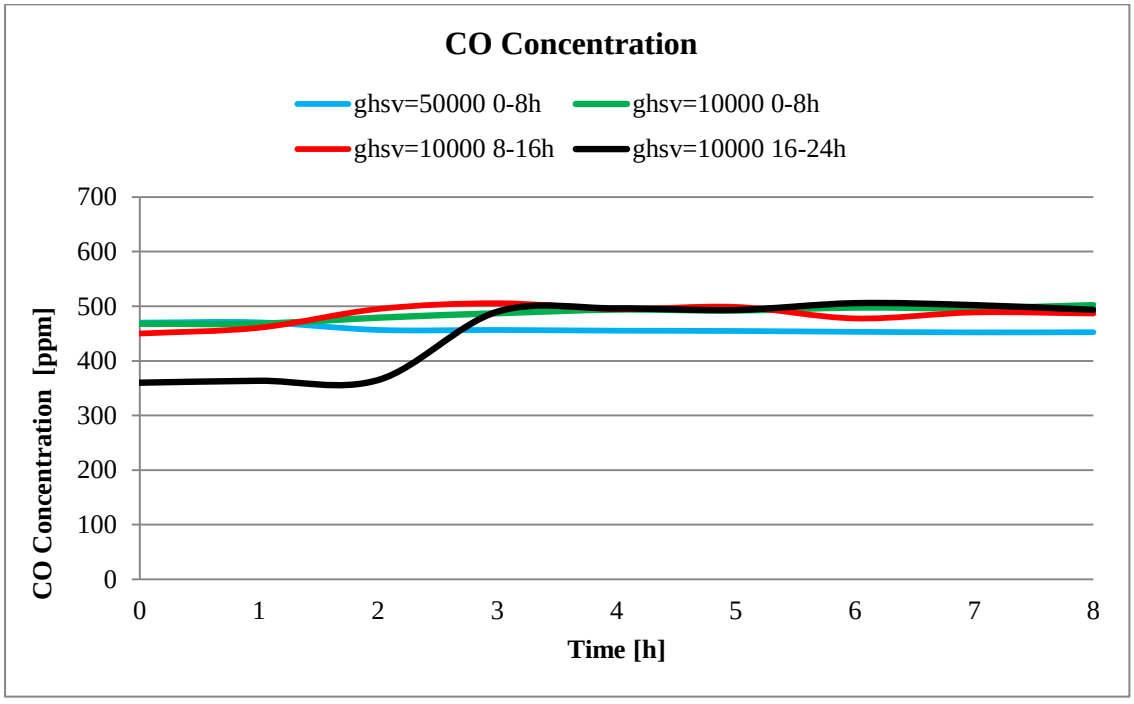

Fig. 4.34: CO concentration for samples A at different GHSV.

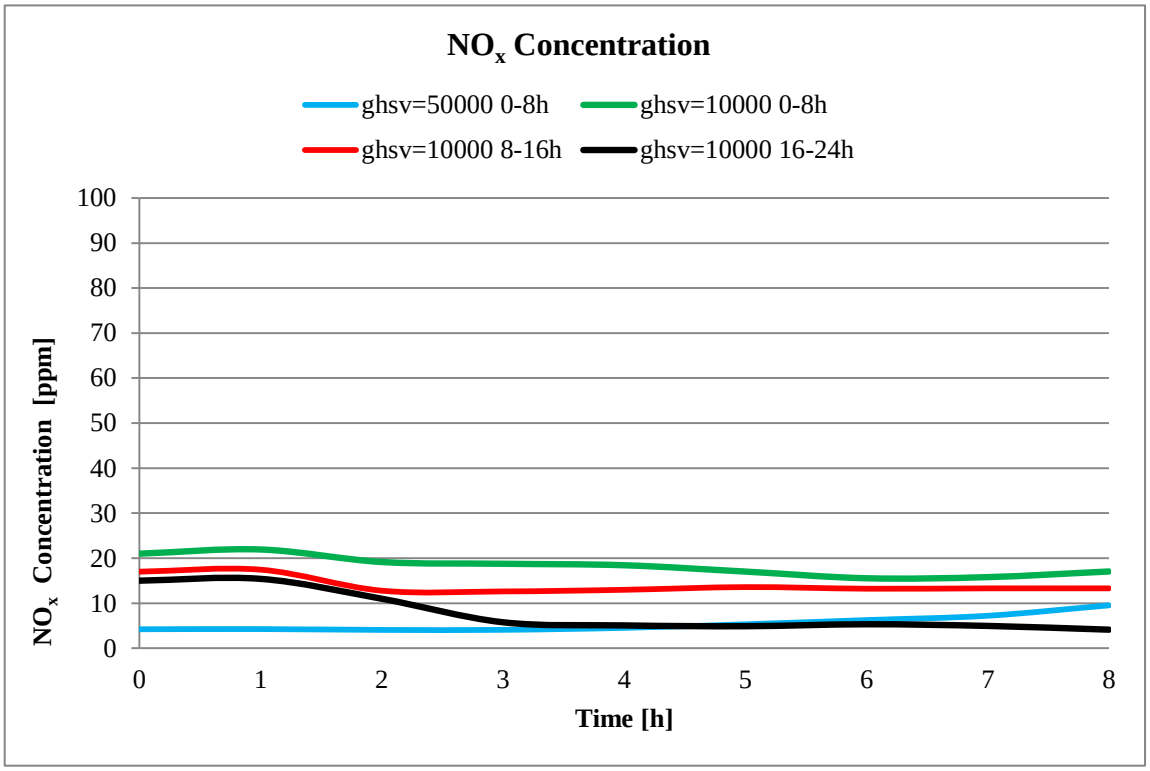

Fig. 4.35: NO_x concentration for samples A at different GHSV.

With a GHSV equal to 50000 h^{-1} lower CO_2, CO and NO_x concentrations were obtained and with GHSV equal to 10000 h^{-1} the different compounds concentrations did not follow the same trend: CO_2 and NO_x concentration for the first two steps (0-8 h and 8-16 h) had the opposite behaviour.

The CO_2 concentration did not reach the value of 2100 ppm (complete oxidation of the molecules of the mixture) due to the partial oxidation to CO.

4.1.5 Catalytic activity measurement on structured catalysts developed

The last test was performed on a lab-scale monolith maintaining the same W/F of the powder, with a diameter of 3,3 cm and height of 2,5 cm and 300 cpsi.

The GHSV used was equal to 5000 h^{-1} with a total flux of 1050 ml/min.

The tests were performed maintaining the temperature of 400 °C for 4 h.

The durability tests are necessary to understand the deactivation of the catalyst.

In this test was evident as the complete oxidation of all the molecules involved occurred and a maximum of NO_x formation equal to 15 ppm was reached (see Figs. 4.36, 4.37).

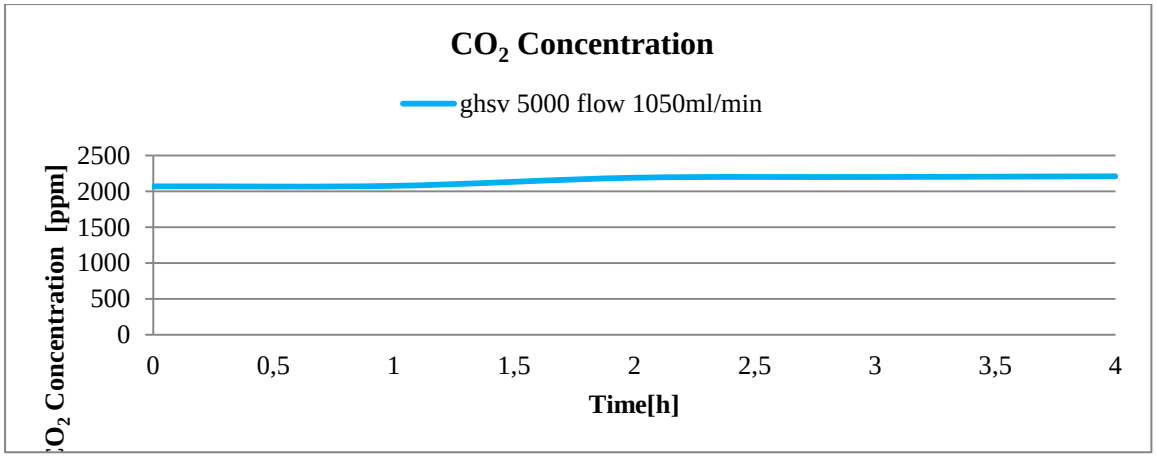

Fig. 4.36: CO_2 concentration for samples A under a total flow of 1050 ml/min and GHSV= 5000 h^{-1}.

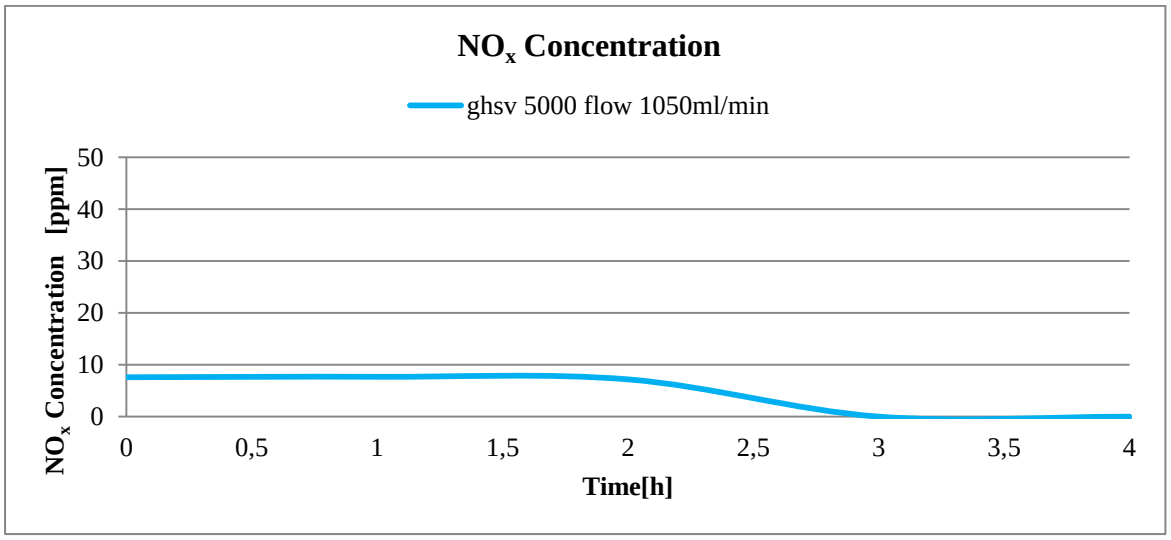

Fig. 4.37: NO_x concentration for samples A under a total flow of 1050 ml/min and GHSV= 5000 h^{-1}.

4.2 BIBLIOGRAPHY

[1] J. Zhou, Q.-H. Xia, S.-C. Shen, S. Kawi, and K. Hidajat, *"Catalytic oxidation of pyridine on the supported copper catalysts in the presence of excess oxygen",* Journal of Catalysis 225 (2004) 128–137

[2] A. Sultana , M. Sasaki, K. Suzuki, H. Hamada, *"Tuning the NO_x conversion of Cu-Fe/ZSM-5 catalyst in NH_3-SCR",* Catalysis Communications 41 (2013) 21–25

[3] R. A. Buffo, and C. Cardelli-Freire "Coffee flavour: an overview", Flavour Fragr. J. 2004; 19: 99–104

[4] I. LOÄ Pez-Galilea, N. Fournier, C.Cid,. and E. Guichard, "Changes in Headspace Volatile Concentrations of Coffee Brews Caused by the Roasting Process and the Brewing Procedure"

[5] C. Sanz, D. Ansorena, J. Bello, and C. Cid, "Optimizing Headspace Temperature and Time Sampling for Identification of Volatile Compounds in Ground Roasted Arabica Coffee", J. Agric. Food Chem. 2001, 49, 1364-1369

[6] S. Schenker, C. Heinemann, M. Huber, R. Pompizzi, R. Perren, AND F. Escher "Impact of Roasting Conditions on the Formation of Aroma Compounds in Coffee Beans" JOURNAL OF FOOD SCIENCE—Vol. 67, Nr. 1, 2002

[7] C. Yeretzian, A. Jordan, R. Badoud, W. Lindinger " From the green bean to the cup of coffee: investigating coffee roasting by on-line monitoring of volatiles" Eur Food Res Technol (2002) 214:92–104

Chapter V: Conclusions

5.1 Catalysts for NO_x abatement

Manganese oxides prepared in different structures and morphology generally confirmed to possess very interesting properties for low-temperature SCR of nitrogen oxides.

The presence of Mn_3O_4 in the catalyst seemed to be the key factor to get the active and, most of all, selective sample.

The crystallinity degree also played a relevant and obvious role, because too crystalline catalysts with low surface area performed much worse than more amorphous sample.

From the catalytic point of view, G2N1_400 sample showed the best activity in SCR of NO_x: this behaviour was ascribed to the different composition of the surface of the sample, characterized by a higher amount of O_α and Mn^{4+} species.

The latter were able to adsorb a larger amount of ammonia both as weakly adsorbed molecules (physisorbed) and as strongly adsorbed molecules.

Anyway, in the presence of a relatively huge amount of SO_2 (100 ppm) the activity all samples was severely reduced, although a regeneration treatment of catalyst carried out for 2 h at 400 °C was able to almost completely restore the catalytic performances.

MnO_x-CeO_2 catalysts synthesized by SCS, in order to achieve different compositions and chemical–physical properties, generally confirmed to possess very interesting properties for low-temperature NH_3-SCR of nitrogen oxides.

Depending on the Mn/Ce ratio as well as on the organic fuel amount employed in there action, the samples exhibited different structures, morphologies, specific surface areas, Mn average oxidation states and superficial contents of Mn, Ce and O atoms.

All the samples showed a NO_x conversion higher than 90% in a sufficiently wide range of temperatures, even if associated to a variable behaviour in terms of selectivity towards N_2.

The catalysts with a Mn/Ce ratio equal to 1 and synthesized under below stoichiometric conditions presented higher NO_x conversion at low temperatures but lower selectivity with respect to the above-stoichiometric counterparts.

The increase of the MnO_x content allowed enlarging the operating window of temperature in the range 100–225 °C, in which the Mn9Ce1_Gly− sample showed a yield higher than 60%.

So the addition of ceria to pure MnO_x permitted to obtain higher values of NO_x conversion as well as higher N_2 yield especially at low temperatures.

In particular, the MnO_x catalyst with a small amount of CeO_2 obtained by SCS with glycine as organic fuel in below-stoichiometric conditions showed the most promising catalytic performance for the low-T ammonia-SCR of NO_x.

In this case, the presence of Mn_3O_4 coupled with a considerable reducibility, seemed to be the principal factor to get the most active and selective catalyst, in agreement with previous findings over pure MnO_x phase.

5.2 Catalysts for prevention of NO_x formation

From the catalytic activity tests carried out on a pilot plant with model and probe molecules representative of roasting, both pure and mixed, it appears that all catalysts synthesized and tested showed oxidative capacity for mixtures considered.

The tests were carried out using concentrations of the molecules of interest consistent with the data provided by a company, investigating a wide range of temperature, between 150 and 500 °C, in particular to evaluate the performance of the catalysts at low temperature.

In the mixture with template molecules we have been used the following compounds: ammonia (representative of the compounds N-nitrogen), ethylene, propylene and toluene (representative VOC), carbon monoxide and oxygen.

In the mixture with probe molecules representative of those actually present in the emitted gases from roasting, pyridine (Representative of the compounds N-nitrogen), methanol (representative of the VOC), carbon monoxide and oxygen have been used.

In all the tests, both with single compounds and with the mixtures, the catalysts that had shown greater ability of selective oxidation of nitrogen-containing molecules and volatile organic compounds were A, B and C.

These catalysts showed a negligible production of oxides of nitrogen and do not exhibit emission of carbon monoxide, allowing a complete conversion of all the molecules present in the system to CO_2 and N_2.